UNIVERSITÀ DEGLI STUDI FIRENZE

Tesi di Dottorato in Ingegneria Industriale
Scienza ed Ingegneria dei Materiali
Ciclo XXXII

Nanometric spinel ferrites: a versatile platform for biomedical and energy applications

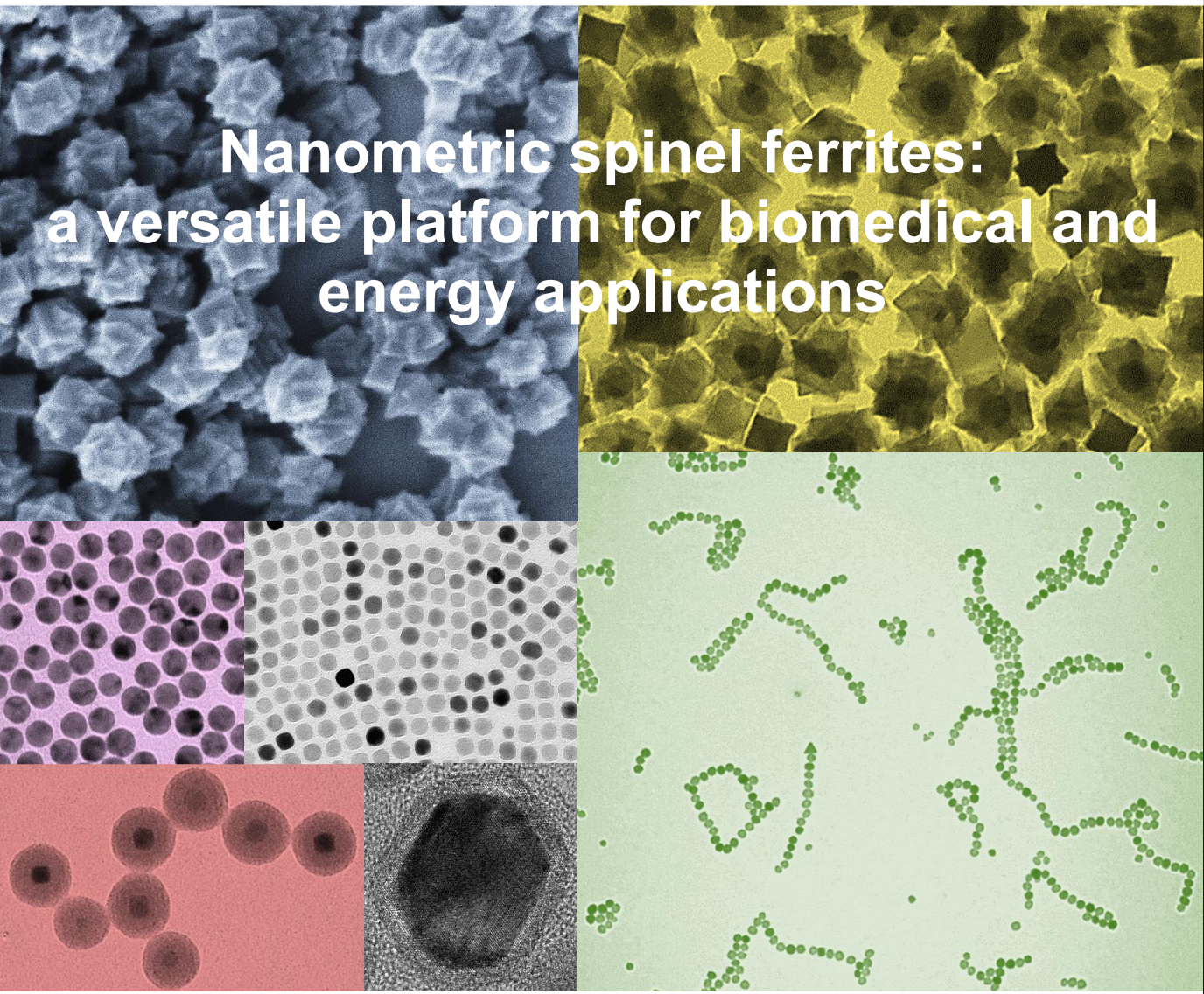

Martin Albino

2016-2019

Tutors:
Prof. A. Caneschi
Dott. C. Sangregorio

UNIVERSITÀ
DEGLI STUDI
FIRENZE

DOTTORATO DI RICERCA IN
INGEGNERIA INDUSTRIALE
(*Indirizzo in SCIENZA ED INGEGNERIA DEI MATERIALI*)

CICLO XXXII

COORDINATORE Prof. De Lucia Maurizio

Nanometric spinel ferrites: a versatile platform for biomedical and energy applications

Settore Scientifico Disciplinare ING-IND/22

Dottorando
Dott. Albino Martin

_____

Tutori
Prof. Caneschi Andrea

_____

Dott. Sangregorio Claudio

_____

Coordinatore
Prof. De Lucia Maurizio

_____

Anni 2016/2019

Table of contents

Chapter 4

Chapter 5

Chapter 6

Appendix

Chapter 1

Introduction

Nanotechnology is a branch of applied science and technology that deals with the control of matter at the nanometric scale (usually between 1 and 100 nm) in order to design and realize devices working at that scale. In the last decades, nanomaterials have been the object of intense study both in fundamental research and in technological applications. They have many applications, such as in catalysis, energy conversion, electronics, cosmetics, data storage, sensors, ferrofluids and biomedicine [1-7] and have potential to completely change the world we live in (Figure 1.1). Indeed, the reduction of materials to the nanometric scale causes significant changes in the physical and chemical properties of the bulk material that can be attractive and unexpected. There are two main factors at the basis of the unique properties of nanomaterials: the increase in surface area and finite-size effects. As the material size reduces respect to the characteristic length scale of the material (e.g., electron mean free path, domain wall width, superconducting coherence length, diffusion length, etc.), confinement effects occur modifying the related physical or chemical properties and determining the emergence of completely new optical, magnetic and electronic properties [8]. On the other hand, the reduction of the material to the nanometric scale implies a dramatic increase in the fraction of atoms located at the surface, whose behaviour is strongly affected by alterations in coordination number, symmetry of the local environment and matrix interaction [8, 9]. Moreover, the very high

surface/volume ratio is crucial in many applications such as catalysis, cosmetics, sensors, biomedicine, etc..

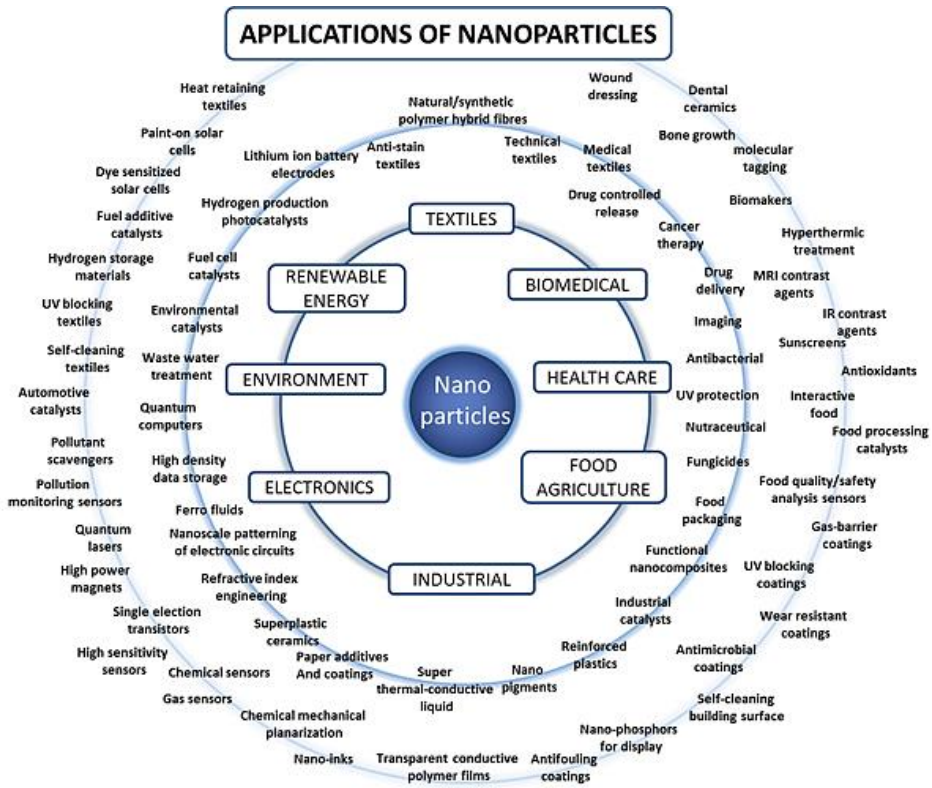

Fig 1.1. Research areas and applications in which nanomaterials have potential to completely change the world we live in. Image taken from Ref. [10].

Among the many nanomaterials investigated to date, ferro- and ferrimagnets are one of the most intriguing. Magnetic nanoparticles (MNPs) are, indeed, a class of nanomaterials that can be manipulated using an external magnetic field. MNPs usually include transition metals (iron, cobalt, zinc, manganese and nickel) and/or rare-earth elements (samarium,

dysprosium, lanthanum, niobium, etc.) to give rise to several kinds of compounds that can be classified as metals, alloys, oxides, ceramic or organometallic compounds [11]. Beside their size, the importance of MNPs relies on their specific properties, the most significant one arising from superparamagnetism [12].To minimize its magnetostatic energy a ferro- or ferrimagnetic massive material assumes a multi-domain structure in which the individual Weiss magnetic domains, where all the spins are aligned, are separated by the Bloch walls, where the spins gradually rotate to connect the orientations of contiguous domains. When the particle size becomes comparable or less than the thickness of a Bloch wall (critical dimension, d_c) [13], the formation of the multi-domain structure is no longer energetically favoured and each MNPs will therefore assume a single magnetic domain spin configuration and its magnetic behaviour will be described by a single magnetic moment given by the sum of all the atomic spins of the nanoparticle [14]. The value of d_c depends on the material properties and some examples are reported in Table 1.1.

Magnetic material	d_c (nm)
Co	70
Fe	14
Ni	55
Fe_3O_4	128
$CoFe_2O_4$	128
$MnFe_2O_4$	50
γ-Fe_2O_3	166
NdFeB	100

Tab. 1.1. Critical dimension of some magnetic materials. Modified from Ref. [15].

The behaviour of single-domain MNPs is described by the Stoner-Wohlfarth model [14], which assumes the MNPs are all single domain, do not interact with each other and have uniaxial anisotropy. Each MNPs can therefore be assigned a magnetic moment $\mu=M_S V$, where M_S is the saturation magnetization and V the volume. Moreover, in the case of uniaxial anisotropy, the anisotropy energy E_m is described by the equation:

$$E_m = KV \operatorname{sen}^2 \theta \tag{1.1}$$

where K is the anisotropy constant, and θ is the angle between the magnetic moment and the anisotropy axis. This equation shows that there are two energy minima corresponding to $\theta = 0$ and $\theta = \pi$, separated by an energy barrier, $\Delta E_b=KV$, i.e. the magnetic moment will be preferably aligned along an axis that takes the name of easy axis of magnetization (Figure 1.2).

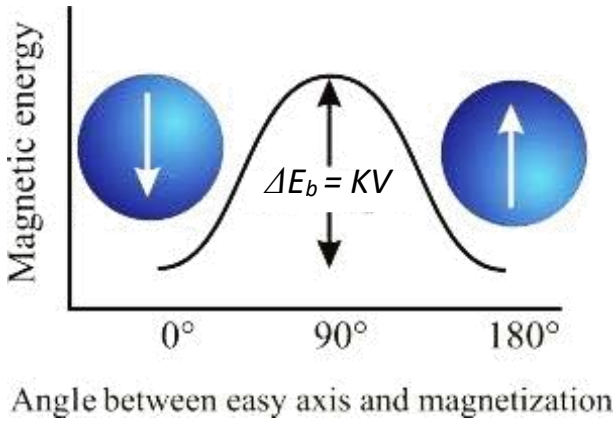

Fig. 1.2. Energy of a single domain MNPs with uniaxial anisotropy as a function of the angle between the magnetization vector and the easy axis of the magnetization.

When the thermal energy is much lower than the barrier energy ($K_BT<<\Delta E_b$), the magnetization of the MNPs will be blocked at the two energy minima. By increasing the temperature, the magnetization will be free to oscillate around the easy axis of magnetization and when $K_BT\geq\Delta E_b$, can pass from one minimum to the other. Under these conditions the system behaves macroscopically as a paramagnet, but since the magnetic moment of the MNPs is given by the sum of ca.10^2-10^4 atomic spins, its value is much higher. For this reason, this behavior is called superparamagnetism and the temperature at which the MNPs reaches the superparamagnetic regime is known as blocking temperature, T_B. At temperatures below T_B the free movement of the magnetic moments is blocked (ferromagnetic-like behaviour), while above T_B the magnetic moment will freely fluctuate like in a paramagnet (superparamagnetism).

The magnetic properties of MNPs are thus determined by many factors, such as chemical composition, crystalline structure, particle size, shape and morphology. In principle, by changing one or more of these parameters, it is possible to control, to a certain extent, the magnetic, catalytic, electric and optical properties of the material for the production of nanodevices in different research areas. Therefore, during the last decade the range of application of MNPs has remarkably increased thanks to the combination of the size-dependent properties with the possibility of tuning them through the control of synthetic parameters.

Among the many fields where the use of magnetic nanoparticles has been proposed so far, biomedical applications are by no doubts one of the most prominent. These include marking and separation of biological materials, controlled drug release (drug delivery systems), magnetic resonance imaging (MRI) and magnetic fluid hyperthermia treatment (MFH) [16-21]. There are several reasons explaining the huge interest arisen by these

applications. First of all the nanometric size of MNPs is comparable or smaller than to those of cells (10-100 μm), viruses (20-450 nm), proteins (5-50 nm) or of a single gene (width 2 nm and length 10-100 nm), which allows MNPs can be used, when properly functionalized, to easily interact with these biological entities.Then, MNPs can be used as multifunctional units in theranostic, a new frontier of oncology in which a single nanostructured material carries out both a diagnostic and a therapeutic action. Thanks to the nanometric dimensions and the magnetic properties, such a nanosystem can be injected into the blood vessels, delivered to the target cells through an external magnetic field and here it can be used as a contrast agent (CA) for MRI and as a heat mediator in MFH. In fact, MNPs are used as CA because they reduce the transverse relaxation time, T_2, of water protons with consequent darkening of the area in which they are located; this is why they are called negative CA with respect to traditional CA, such as the paramagnetic complexes of gadolinium [22-24] which instead reduce the longitudinal relaxation time, T_1, (positive CA). Some example of clinically approved CA based on dextran coated ferrite MNPs (total average diameter between 30 and 150 nm) are: Endorem® (Guerbet), also known as Feridex, Feraheme® (AMAG Pharmaceuticals), Primovist® and Eovist® (Bayer Schering Pharma AG) [25, 26]. MNPs are also used as heat mediators in MFH; in fact, MNPs colloidal solutions can convert the energy of an alternating magnetic field, of appropriate intensity and frequency, into heat (ν of 50-500 kHz, H_0 up to 15 kAm^{-1}, maintaining the $H_0\nu$ product below the tolerance threshold of 5×10^9 $Am^{-1}s^{-1}$ to avoid deleterious physiological responses such as skeletal muscles stimulation, cardiac stimulation and arrhythmias [17]). Cancer cells are more sensitive to heat than healthy cells because tumour vessels, lacking muscular scaffold, do not allow adequate vasodilation and consequent heat

dissipation; moreover, temperatures of 42-46 ° C for at least 30 minutes stimulate the production of caspases, essential proteases to activate cell apoptosis [27]. MNPs studied as CA and heat mediators are currently iron oxides, magnetite (Fe_3O_4) and maghemite (γ-Fe_2O_3), with a spinel structure that present low toxicity, are biocompatible and biodegradable and have good magnetic properties, both in terms of magnetic moment and anisotropy [16]. For example, Dr. Andreas Jordan' group of MagForce Nanotechnologies AG, at Berlin's Charité Hospital, using the combined action of radiotherapy and MFH, reported a significant improvement in the treatment of glioblastoma multiforme and prostate cancer. To obtain this result, high doses of MNPs (12 nm iron oxide coated with aminosilane ca. 35 mg/cm^3) were implanted directly into the tumour mass [28]. However, the clinical application of MFH is still severely limited due to the low amount of heat that can be produced into the tumour mass and to the high amount of magnetic material to be introduced into the body to have the desired effects. For this reason, research focuses on other materials with improved hyperthermic properties. A possible way to realize this purpose is the doping of magnetite with other metal ions [29, 30], for improving the magnetic properties, which are strongly related to the hyperthermic and relaxometric efficiency. One of the most noticeable examples is cobalt ferrite, whose magneto-crystalline anisotropy is about twenty times higher than that of magnetite [31]. The possibility to dispose of a material with improved hyperthermic properties allows for several advantages, such as reducing NPs size and introducing in the human body a smaller quantity of exogenous material while keeping constant the hyperthermic efficiency [32]. Moreover, smaller NPs, avoiding the uptake by the immunitary system, will have a longer half time in blood vessels reaching the target tissue more efficiently [20]. However, while traditional

ferrites contain only biocompatible iron ions, in doped ferrite the presence of other metal ions could lead to the issue of toxicity [33]. Despite this aspect is not particularly limiting, given the remarkable toxicity of several radio and chemotherapeutic drugs in use for the most of cancer therapies, it is necessary to investigate alternative routes in order to reduce all side effects.

Another important field of application of MNPs is electronics, where, the huge demand of new-generation high-tech devices of the recent years is pushing researchers to find novel materials with better and finely controlled properties. In particular, the requirement of miniaturization inherent to high-tech components has led the scientific community to design and synthesize nanostructured materials. Micrometric ferrites found a large use in the production of electronic devices as inductors (electronic components that store electrical energy in the form of a magnetic field) and transformers (electronic components which transfer electrical energy between two or more circuits, through electromagnetic induction). They consist of a winding of conductive material, generally copper wire, on a core of material with high magnetic permeability (ferrites or other soft magnetic materials). These devices have the capability to convert electric energy in magnetic energy and the opposite. Therefore, their use is strongly dependent on the efficiency of the conversion process, reducing as much as possible the dissipation of energy into heat (power losses) [12, 34]. Inductors and transformers containing magnetic cores based on micrometric spinel ferrite doped with manganese and zinc are optimized for operating in the range 1-2 MHz and for higher frequency exhibits extraordinary increased power losses. On the other side, magnetic cores used for higher frequency application, in the range of GHz, such as micrometric spinel ferrite doped with nickel and zinc, also

exhibits high power losses, mostly due to lower relative permeability. Nowadays, magnetic cores for traditional electronic applications in high-frequency range (1-2 MHz) are obtained with standard methods, usually starting from micrometric ferrites, obtained by ball-milling of bulk materials, suitably sintered in the desired shapes. Even if the cost of raw materials and production processes of these materials and devices is quite cheap, the high-power losses at higher frequencies represent an important hurdle to their applicability in the near future. Indeed, an increase of the operating frequency is expected to meet the needs of the market of increasingly efficient electronic devices (faster, smaller and more powerful). Thus, the development of more effective soft magnetic materials, suitable to produce electronic devices in high-frequency range is still an open challenge. Also in this context, material nanostructuration could provide a solution to significantly decrease power losses [35], as it may allow a decrease in coercive field and remanence while maintaining the saturation magnetization unaltered with respect to the corresponding bulk materials.

Among technological applications, MNPs have shown remarkably promising properties which can be exploited also in the permanent magnet research area. A magnet can be considered as an energy-storage device which provides a magnetic field in a particular volume of space. Magnetic materials can be divided into two classes: hard and soft. Hard magnetic materials show high saturation magnetization (M_S), high remanence (M_R) and high coercivity (H_C) while soft magnetic material display high M_S, low M_R and low H_C. Hard magnetic materials are usually called permanent magnets, because, once magnetically saturated, they are hardly demagnetized without applying a large magnetic field, while soft magnetic materials, being easily demagnetized, exhibit relevant magnetic properties

(large magnetization) only when a magnetic field is applied (Figure 1.3). The applications of a permanent magnet are determined by the magnetic energy density that can be stored in the material per volume unit, which is described by the maximum energy product, $(BH)_{max}$ (Figure 1.4), where B is the magnetic induction, given by (in SI units): $B=\mu_0(H+M)$ where μ_0 is the vacuum permeability ($\mu_0 = 4\pi \cdot 10\text{-}7\ Hm^{-1}$) and M the magnetization of the material. In other words, BH is the combination of the operative flux density (the magnetic induction, in working condition) and the magneto-motive force (the resistance of the magnet to demagnetization, i.e. the coercive force).

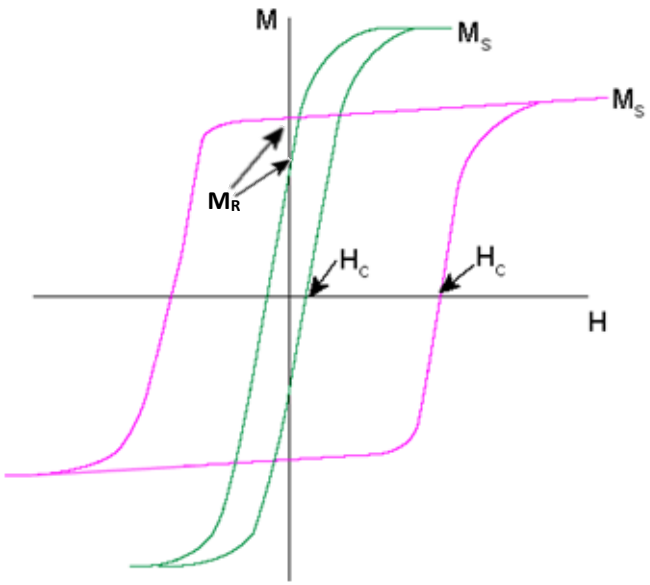

Fig. 1.3. Hysteresis loop of hard (violet line) and soft (green line) materials. Modified from Ref. [36].

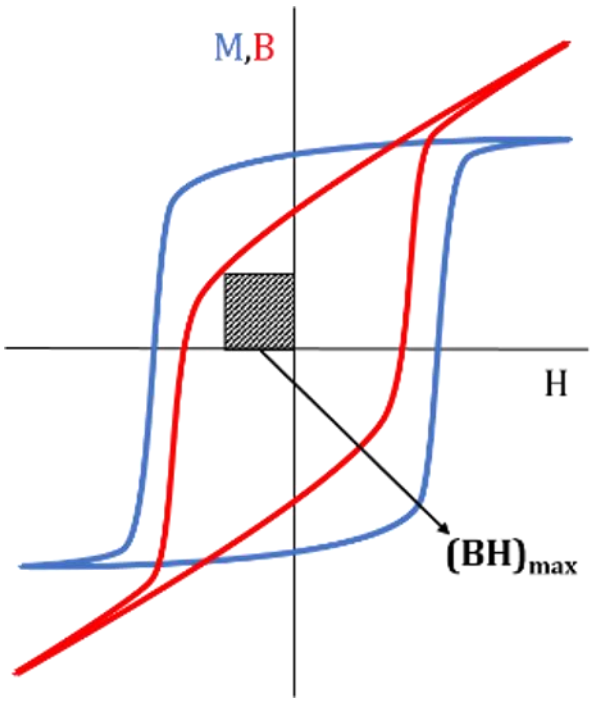

Fig. 1.4. Typical magnetization (M, blue curve) and magnetic induction (B, red curve) dependence on the applied field (H) for a permanent magnet. The maximum energy product ($(BH)_{max}$) corresponds to the area of the largest rectangle that can be inscribed under the demagnetizing branch of the B(H) curves at negative fields (the second quadrant) [37].

The worldwide market of permanent magnets moved about 9 billion dollars in 2011 and it is expected to reach 14 billion dollars in 2020. Permanent magnets are key elements of many technological devices that are used in different areas such as electronics, data storage and the automotive industry (a medium-size car contains more than 400 permanent magnets for a total weight of ca. 50 kg). Furthermore, permanent magnets are used in the construction of electric engines and generators that convert electrical energy into mechanical energy and contrary (generators used in

latest wind turbines require up to 2 tons of permanent magnets) [38-40]. In the 1980s, rare earths permanent magnets with high $(BH)_{max}$ values, ranging from 100 kJm^{-3} to over 400 kJm^{-3} for magnets based on NdFeB, were produced, with large success, in Japan and United States. These materials thanks to transition metals (high magnetic moment) and rare earths (high anisotropy) show $(BH)_{max}$ values about 5-10 times higher than the other permanent magnets (typical values for the two most common traditional materials are 35 kJm^{-3} for hard ferrites as strontium hexaferrite, $SrFe_{12}O_{19}$ and barium hexaferrite, $BaFe_{12}O_{19}$, and 45 kJm^{-3} for Alnico, an iron alloys containing mainly Al, Ni and Co (Figure 1.5).

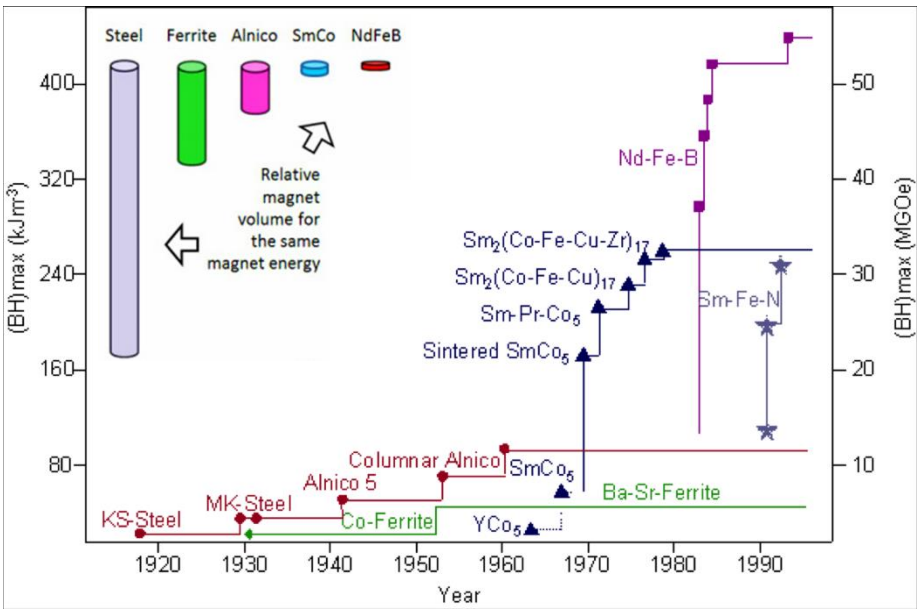

Fig. 1.5. The development of different permanent magnets in the 20th Century and relative $(BH)_{max}$ values. Modified from Ref. [39].

Rare earth elements pose important problems from a strategic and an environmental point of views with fundamental economic and social

implications at the worldwide scale. Most of the mines and reserves of rare earths are located in China and Africa, in past years underdeveloped country, and for this reason rare earths based permanent magnets have been produced with low production costs and quickly conquered most of the market. However, the situation has changed radically in recent years: the emerging countries, China in particular, started to develop their own technological devices instead of simply exporting the raw materials. Moreover, by controlling 97% of rare earth mining, China is in control of the world market. Consequently, rare earths represent the elements with the highest supply risk [41]. In addition, a serious environmental impact of rare earths mining should not be neglected due to the acidic wastewater and radioactive residues generated in the refinement process. Nevertheless, nowadays most of technological applications use rare earths-containing permanent magnets, although a relevant number of them (mainly in automotive and energy industries) requires magnets with only moderate energy product within the range of 35-100 kJm^{-3}. The increase of the energy product of standard ferrites above that threshold would thus allow the replacement of rare earth based permanent magnets in all the applications requiring low performing permanent magnets, reducing the dependence on these critical materials. Among the different approaches proposed to maximize the $(BH)_{max}$ a lot of attention has been paid towards the development of rare earth free nanostructured hybrid materials based on the coupling of a hard magnetic material with a soft magnetic one, producing a so-called exchange-spring permanent magnet (Figure 1.6) i.e. a material which takes benefits form the properties of both components. [42, 43]. In fact, the exchange interaction between the spins of the two different magnetic phases which occurs at the interface may allow a

significant enhancement of the remanence of the hard/soft hybrid nanocomposite with only a moderate decrease of the magnetic anisotropy.

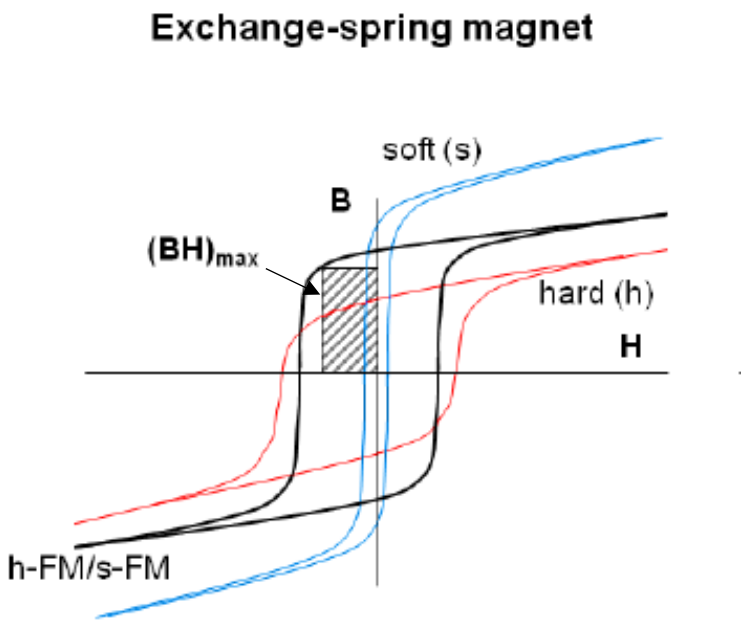

Fig. 1.6. Illustrative picture of the effect of hard-soft magnetic exchange coupling on the maximum energy product in a hard/soft hybrid nanocomposite (h-FM/s-FM). Modified from Ref. [44]

All these applications require the fine tuning and the optimization of the magnetic properties of the nanomaterial. From this point of view, spinel ferrites, which are an extremely versatile platform, represent an excellent starting material to reach these goals.

The work of this thesis moves within this context, as it addresses the investigation of the effects of different divalent metal ions (cobalt, manganese, zinc) on the magnetic properties of spinel ferrite

nanoparticles. Therefore, we aim at exploiting two complementary approaches: on one hand, we will explore the possibility of improving the magnetic properties of ferrites reducing the size of magnetic materials to the nanometric scale. On the other, we will exploit the huge versatility of ferrite and the related tunability of physical properties. In fact, their magnetic properties can be drastically modified by simply replacing, either completely or partially, metal ions or by modifying the inversion degree without affecting the crystal structure. In this framework, there is a strong interest to investigate the effect of different metal ions on the magnetic properties of ferrite nanoparticles.

Regards biological applications, the work focused on the effect of Co-Zn co-doping, which is supposed to increase both the magnetic moment and the anisotropy of magnetite nanoparticles and, consequently, also the hyperthermic and relaxometric efficiency.

Concerning high frequency electronic applications, the work addressed the development of a synthetic route, suitable for industrial scale-up, to prepare $Mn_xZn_yFe_zO_4$ (x+y+z=3) MNPs of different composition with the aim to maximize the M_S and the magnetic permeability of the final product and reduce power losses for future application in the 2-5 MHz frequency range.

Finally, with regards to the permanent magnet research area, the idea is to couple a hard magnetic material (strontium hexaferrite, $SrFe_{12}O_{19}$) to a soft magnetic material ($Mn_xZn_yFe_zO_4$) to maximize the $(BH)_{max}$ of the final product. In particular, here we focused on the synthesis of the soft component, aiming at preparing a material with a high value of M_S in order to increase the remanence of the final product (Figure 1.6). It is important to note that this work partially matches with that carried on to minimize

power losses in Mn-Zn ferrite. The improvement in the two applications require, indeed, the maximization of the magnetic permeability in one hand, and of the remanence in the other, conditions which can be both satisfied by a soft material with a high M_S value.

This thesis is structured as follows:

Chapter 2. After a brief overview on the crystalline spinel structure of ferrites and their magnetic properties, a summary of the synthetic techniques to prepare MNPs is presented. In particular, the bottom-up wet chemical approach and the synthetic parameters that control the size, size-distributions, shape and composition of the nanoparticles are discussed.

Chapter 3. Synthesis and structural, magnetic, hyperthermic and relaxometric characterization of narrowly distributed $Co_xZn_yFe_{3-(x+y)}O_4$ MNPs ($x=0.6$, $0 \leq y \leq 0.4$) for biomedical applications prepared by thermal decomposition of metal acetylacetonates in high-boiling solvents in the presence of surfactants. In particular, the effect of Zn inclusion on the magnetic properties of spinel ferrite nanoparticles is discussed in detail.

Chapter 4. Development of a synthetic route, suitable for industrial scale-up, to prepare $Mn_xZn_yFe_zO_4$ ($x+y+z=3$) MNPs with variable composition with improved magnetic properties to be used as low power loss powder to be integrated in electronic devices operating at high frequency and as building blocks to realize exchange coupled rare-earth free permanent magnet. In particular, the synthesis and structural and magnetic

characterization of the MNPs prepared by co-precipitation from aqueous solution of metal chlorides is reported. The heat treatment conditions to maximize the M_S of the final product are then discussed and finally, the industrial scale-up of the synthetic process, carried out in collaboration with the chemical company Cabro S.p.A. in Arezzo, is presented.

Chapter 5. Brief summary of the main conclusions obtained from the experimental work presented above and perspectives for the application of these materials for biomedical and technological applications, respectively.

Chapter 6. Synthetic procedures and main experimental techniques used to characterize the samples.

Appendix. List of published articles during the PhD.

References

[1] P. T. A. Santos, A. C. F. M. Costa, R. H. G. A. Kiminami, H. M. C. Andrade,H. L. Lira, L. Gama, *J. Alloys Compd.* **2009**, *483*, 399.

[2] L. Menini, M. C. Pereira, L. A. Parreira,J. D. Fabris, E. V. Gusevskaya, *J. Catal.* **2008**, *254*, 355.

[3] J. Tonga, L. Boc, Z. Li, Z. Lei, C. Xia, *J. Mol. Catal. A* **2009**, *307*, 58.

[4] B. D. Terris, T. Thomson, *J. Phys. D: Appl. Phys.* **2005**, *38*, R199.

[5] S. S. R. K. Challa, M. Faruq, *Adv. Drug. Delivery Rev.* **2011**, *63*, 789.

[6] I. C. Lekshmi, R. Buonsanti, C. Nobile, R. Rinaldi, P. D. Cozzoli, G. Maruccio, *ACS Nano* **2011**, *5*, 1731.

[7] M. Takafuji, S. Ide, H. Ihara, Z. Xu, *Chem. Mater.* **2004**, *16*, 1977.

[8] G. Cao and Y. Wang, *Nanostructures and Nanomaterials: Synthesis, Properties, and Applications* Second Ed., World Scientific Publishing Co. Pte. Ltd. **2011**.

[9] E. Roduner, *Chem. Soc. Rev.* **2006**, 35, 583.

[10] https://chandanashah.svbtle.com/few-major-applications-of-nanoparticles-in-diverse-sectors.
Image Resource: people.forestry.oregonstate.edu.

[11] A.-H. Lu, E. L. Salabas, F. Schüth, *Angew. Chem. Int. Ed.* **2007**, 46, 1222.

[12] J. M. D. Coey, *Magnetism and Magnetic Materials*, Cambridge University Press **2010**.

[13] R. H. Kodama, *J. Magn. Magn. Mat.* **1999**, 200, 359.

[14] E. C. Stoner, E. P. Wohlfarth, *Philosophical Transaction of the Royal Society A*, **1948**, *240*, 599.

[15] C. R. Vestal, *Chemistry and Biochemistry*, Georgia Institute of Technology: Atlanta, **2004**.

[16] Q. A. Pankhurst, N. K. T. Thanh, S. K. Jones, J. Dobson, *J. Phys. D: Appl. Phys.* **2009**, 42, 224001.

[17] Q. A. Pankhurst, J. Connolly, S. K. Jones, J. Dobson, *J. Phys. D: Appl. Phys.* **2003**, 36, 167.

[18] J. B. Haun, T. J. Yoon, H. Lee, R. Weissleder, *Nanomed. Nanobiotechnol.* **2010**, 2, 291.

[19] C. T. Yavuz, J. T. Mayo, W.W. Yu, A. Prakash, J. C. Falkner, S. Yean, L. Cong, H. J. Shipley, A. Kan, M. Tomson, D. Natelson, V. L. Colvin, *Science* **2006**, 314, 964.

[20] C. C. Berry, *J. Phys. D: Appl. Phys.* **2009**, 42, 22.

[21] C. C. Berry, A. S. G. Curtis, J. Phys. D: Appl. Phys. 2003, 36, 13.

[22] S. Laurent, L. Vander Elst, S. Houzé, N. Guérit, R. N. Muller, *Helv. Chim. Acta* **2000**, 83, 394.

[23] S. Laurent, D. Forge, M. Port, A. Roch, C. Robic, L. Vander Elst, R. N. Muller, *Chem. Rev.* **2008**, 108, 2064.

[24] E. Taboada, R. Solanas, E. Rodriguez, R. Weissleder, A. Roig, *Adv. Funct. Mater.* **2009**, 19, 2319.

[25] D. Pouliquen, H. Perroud, F. Calza, P. Jallet, J. J. Le Jeune, *Magn. Reson. Med.* **1992**, 24, 75.

[26] W. Reith, M. Forsting, H. Vogler, S. Heiland, K. Sartor, *Am. J. Neuroradiol.* **1995**, 16, 53.

[27] G. F. Goya, V. Grazú, M.R. Ibarra, *Curr. Nanosci.* **2008**, 4, 1.

[28] K. Maier-Hauff, F. Ulrich, D. Nestler, H. Niehoff, P. Wust, B. Thiesen, H. Orawa, V. Budach, A. Jordan, *J. Neurooncol.* **2011**, 103, 317.

[29] G. Baldi, D. Bonacchi, C. Innocenti, G. Lorenzi, C. Sangregorio, *J. Magn. Magn. Mat.* **2007**, 311, 10.

[30] G. Baldi, D. Bonacchi, M. C. Franchini, D. Gentili, G. Lorenzi, A. Ricci, C. Ravagli, *Langmuir* **2007**, 23, 4026.

[31] M. M. Schieber, *Experimental Magnetochemistry: nonmetallic magnetic materials"*, Wohlfarth E. P. Ed, North-Holland Publishing Company, **1967**.

[32] C. Ravagli, *Synthesis and characterization of nanosized magnetic materials for hypertermia applications*, Ph. D. Thesis, University of Florence, **2009**.

[33] D. G. Barceloux, *Clinical Toxicology* **1999**, 37, 201.

[34] B. D. Cullity and C. D. Graham, *Introduction to Magnetic Materials*, Second Ed. Wiley-IEEE Press, **2011**.

[35] A. Skumiel, M. Kaczmarek-Klinowska, M. Timko, M. Molcan, and M. Rajnak, *Int. J. Thermophys.* **2013**, 34, 655.

[36] https://www.quora.com/Why-soft-magnetic-material-is-used-in-transformer.

[37] E. Lottini, *PhD thesis*, **2015**.

[38] O. Gutfleisch, M. A. Willard, E. Brück, C.H. Chen, S. G. Sankar, J. P. Liu, *Adv. Mater.* **2011**, 23, 821.

[39] K. J. Strnat, *Proc. IEEE*. **1990**, 78, 923.

[40] F. Jimenez-Villacorta, L. H. Lewis, *Advanced Permanent Magnetic Materials*, in: J. M. Gonzalez Estevez, *Nanomagnetism*, One Central Press **2014**, 160–189.

[41] Critical Raw Materials, Eur. Comm., http://ec.europa.eu/growth/sectors/raw-materials/specific-interest/critical/index_en.htm, **2017**.

[42] E. F. Kneller, R. Hawig, *IEEE Trans. Magn.* **1991**, 27, 3588.

[43] E. E. Fullerton, J. S. Jiang, S. D. Bader, *J. Magn. Magn. Mater.* **1999**, 200, 392.

[44] https://www.researchgate.net/figure/Illustrative-picture-of-the-effects-o-hard-soft-magnetic-exchange-coupling-and-FM-AF_fig7_270567539.

Chapter 2

Synthesis of spinel ferrite nanoparticles

Since this thesis is focused on the synthesis of nanometric spinel ferrites, in this Chapter, after a brief overview on the crystalline spinel structure of ferrites and on their magnetic properties, a summary of the synthetic techniques to prepare MNPs is presented. Particular regard will be given to the bottom-up wet chemical approach and to the synthetic parameters that can affect size, size-distributions, shape and composition of the nanoparticles.

2.1 Spinel ferrites

As already discussed in the introduction, ferrites nanoparticles have been the object of intense study both in fundamental research and in technological applications due to their remarkable magnetic, catalytic, electric and optical properties, occurring as the particle size decreases down to the nanometric scale. Ferrites are iron oxides with the crystalline structure of the spinel ($MgAl_2O_4$). They have the general formula AB_2O_4, where A is a divalent cation (A^{2+}) and B is a trivalent cation (B^{3+}). They normally adopt a typical arrangement in which the trivalent and the divalent ions occupy, respectively, 16 out of 32 octahedral (O_h) and 8 out of 64 tetrahedral (T_d) crystallographic cavities generated by 32 oxygen ions (O^{2-}) arranged in a cubic closed packed structure. The spinel structure belongs to space group $Fd\overline{3}m$ [1]. This type of spinels are called *"normal*

spinels" (Figure 2.1) and include, for example, $MgAl_2O_4$, $FeAl_2O_4$, $CoAl_2O_4$, $NiAl_2O_4$, $MnAl_2O_4$, $ZnAl_2O_4$. For compounds that adopt the *"inverse spinel"* structure, of which the magnetite is the progenitor, the most correct formula is $B(AB)O_4$.

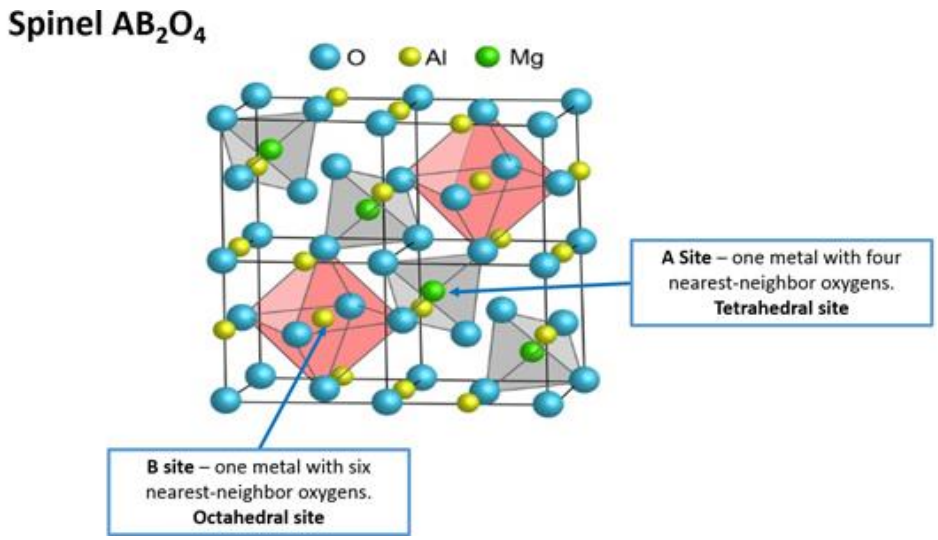

Fig. 2.1. Schematic representation of normal spinel structure AB_2O_4 [2].

Depending on the metal ion distributions, ferrites are classified as normal or inverse spinels: in the first case all the trivalent ions occupy O_h cavities while divalent ions are placed in T_d cavities; in the second one, instead, half of the trivalent ions occupies the T_d sites, while the other half and all the divalent cations occupy the O_h cavities. Finally, we talk about *"partially inverted spinel"* when both types of cations occupy T_d and O_h cavities. Thus, the general formula for spinel ferrites can be expressed as: $[A_{1-i}B_i]T_d[A_iB_{(2-i)}]O_hO_4$, where i is the inversion parameter that can vary from 0 (normal spinel) to 1 (inverse spinel).

A useful model to predict the spinel structure inversion degree is by referring to the Crystal Field Stabilization Energy (CFSE), which describes the stabilization of a given transition metal ion when it is placed in a crystal field generated by external ligands. For a given geometry, the cation will occupy the sites with the higher stabilization energy. Hence, if the trivalent ion has higher CFSE value in O_h site than the divalent cation, a normal spinel is expected. Conversely, an inverse spinel is formed when the divalent cation has higher CFSE value in O_h cavities than the trivalent one. The archetypal spinel ferrite is by no doubt magnetite (Fe_3O_4). From a crystallographic point of view, magnetite has an inverse spinel structure, $Fe^{3+}(Fe^{2+}Fe^{3+})O_4$, due to the higher *CFSE* value of Fe^{2+} in O_h sites with respect to Fe^{3+} (Figure 2.2). It has been found that most mixed ferrites, such as cobalt- and manganese ferrite, exhibit only partially inverted cation distribution [3, 4], and that at the nanoscale the inversion degree can significantly differ according to the adopted synthetic conditions [5-7]. Regarding magnetite, the chemical IUPAC name is iron (II, III) oxide and the common chemical name is ferrous-ferric oxide. It is the iron ore with the highest iron content (72.5%) which can be used industrially. It is the most magnetic of all the naturally occurring minerals on Earth [8-10]. Magnetite is the oldest known magnetic material: it was already known to the ancient Greeks and takes its name from the city of Magnesia ad Sipylum, near Sipilo Mount, where it was found in large quantities. Naturally magnetized pieces of magnetite, called lodestone, attract small pieces of iron, which is how ancient peoples first discovered the property of magnetism. It is present in small quantities in the human body, where it is located between the nose and eyes, inside the ethmoid bone. Several species of birds and other migratory animals possess deposits of biological magnetite in their ethmoid bones, which allows them to sense the

direction, polarity and magnitude of the earth's magnetic field (magnetoreception) [11]. Men possess similar deposits of magnetite, which is believed to be vestiges. Moreover, pure magnetite particles are biomineralized in magnetosomes, which are produced by several species of magnetotactic bacteria. Magnetosomes consist of long chains of oriented magnetite particle that are used by bacteria for navigation. Magnetite is an extremely versatile material, in fact, its physical, chemical and magnetic properties can be drastically modified by simply replacing, either completely or partially, metal ions or by modifying the inversion degree without affecting the crystal structure. Thus, Fe^{2+} ions can be partly or fully replaced by other divalent ions (i.e. Co, Zn, Mn, Ni) and the replacement is allowed by the flexibility of the oxygen framework, which can expand or contract to accommodate cations with different ionic radius (e.g. Mn^{2+} 0.83 Å, Fe^{2+} 0.78 Å, Co^{2+} 0.75 Å, Zn^{2+} 0.74 Å, Ni^{2+} 0.69 Å). Cation substitution is usually accompanied by changes in unit cell edge length [12]. Since the peculiar properties of ferrites are strictly related to the nature and distribution of cations between octahedral and tetrahedral sites in the spinel structure, the control of cation distribution provides a mean to tailor their properties. Therefore, there is a great interest in studying the cation distribution in ferrites, which, in turn, depends on the electronic configuration and valence of the considered ion. Some studies show that also the particle size can influence the cation distribution, especially at the nanometric scale.

From the magnetic point of view, ferrites are generally ferrimagnetic and the magnetic structure can be described considering two antiferromagnetically coupled sublattices, defined by magnetic moments of ions in T_d and O_h cavities, respectively. The ferrimagnetic properties of the ferrites are due to the non-compensated anti-parallel coupling of the

spins in the T_d and O_h sites (Figure 2.2). Ferrites nanoparticles have the same crystalline and spin structure of the bulk materials, but, as already discussed in the introduction, due to their nanometric size, magnetic behavior can be significantly different.

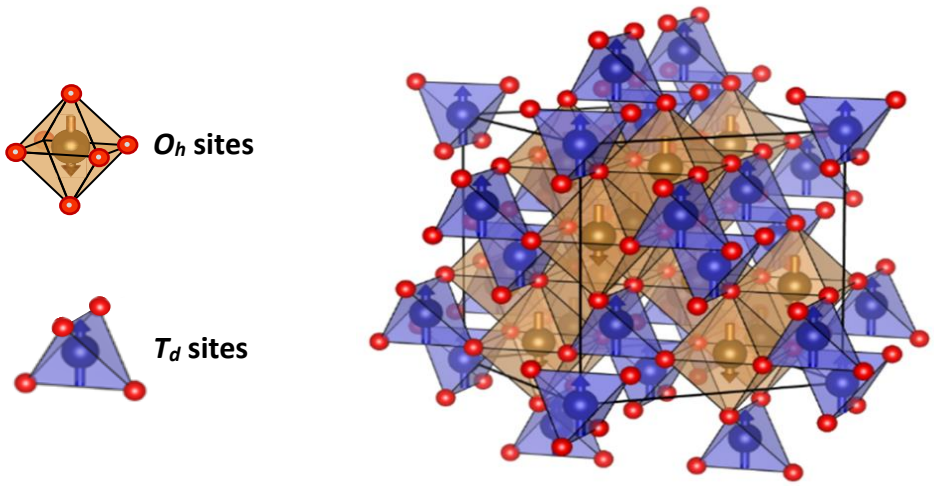

Fig. 2.2. Schematic representation of magnetic and crystalline inverse spinel structure of magnetite, Fe_3O_4. The small red spheres represent O^{2-} ions, the blue spheres with arrows represent Fe^{3+} ions and the gold spheres with arrows represent Fe^{3+} or Fe^{2+} ions. The atomic magnetic moments are described as vectors aligned along the easy axis <110>. Modified from Ref. [13].

2.2 Synthetic methods to prepare nanoparticles

MNPs are used in several research areas where different physical properties are exploited. Since these properties depend on the chemical, morphological and structural characteristics, a large variety of nanoparticles with different shape, size, composition, etc. has been developed to date. One of the fundamental aspects consists in the development of synthetic protocols able to grant for the control of dimensions, shape and chemical composition. In particular, being at intermediate size between bulk materials and molecules or structures at atomic level, nanoparticles can be obtained through two different approaches: “top-down” and “bottom-up” (Figure 2.3). In the top-down approach, nanometric particles are obtained by physical methods, by progressive reduction of the corresponding massive material. Instead, in the bottom-up approach nanostructures are built starting from small components such as atoms, molecules and clusters, used as building blocks [14–19]. At present, the top-down techniques are the most consolidated to obtain large amount of material, while the bottom-up techniques are mostly used at the laboratory scale. Top-down approach includes e.g. lithography, laser ablation, etching, mechanical milling [20]. The main advantage of most of these techniques is the possibility to yield a large amount of material. However, the nanomaterials produced in this way often have a relatively large size distribution and different shapes. Moreover, as is the case of milling, the final product may contain significant amounts of impurities deriving from the grinding medium and defects due to the milling process. Conversely, bottom-up approach usually allows to obtain a better control on chemical composition, size,

shape and size distribution of nanoparticles. Despite of this, generally only sub-gram or gram quantities can be produced.

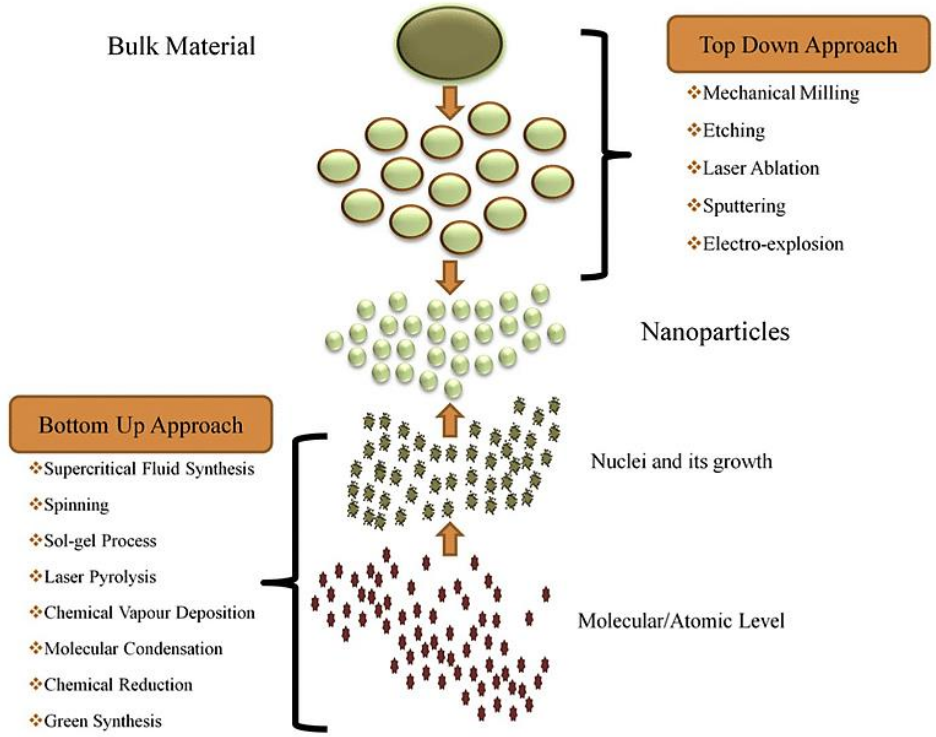

Fig. 2.3. Schematic representation of synthesis of nanomaterials via top-down and bottom-up approaches [21].

Among bottom-up synthetic techniques, colloidal chemical synthesis allows the formation of various-shaped nanoparticles and hybrid nanostructure with different properties with respect to the bulk phases. These includes e.g. co-precipitation, microemulsion, hydrothermal synthesis, polyol synthesis, thermal decomposition [22]. In the following these techniques are shortly reviewed.

Co-precipitation is a facile, cheap, eco-friendly and scalable (up to kilograms) way to synthesize MNPs starting from aqueous solutions of inorganic salts (e.g. chlorides, nitrates, sulphates) [23], by the addition of a base or a reducing agent. The reaction is carried out under inert atmosphere at room temperature or at elevate temperature (up to 100 °C) [24]. Size, shape and composition of the nanoparticles can be tuned by varying the reagents, their concentrations [25], the kind of base [26], the reaction temperature [27], the aqueous media (e.g. pH values and ionic strength) [28, 29] and the presence of surfactants. However, nanoparticles synthesized by co-precipitation are characterized by poor crystallinity and high polydispersity. Thus, usually, subsequent annealing process is necessary in order to achieve good crystallinity and, consequently, good magnetic properties.

Water-in-oil (W/O) microemulsion is based on the same principle of co-precipitation but since the reaction is carried out in a confined media, it allows a better control on size, shape and size distribution of nanoparticles. Microemulsions are isotropic, macroscopically homogeneous, and thermodynamically stable solutions containing at least three components; a polar phase (usually water), an apolar phase and a surfactant that forms an interlayer between the two phases. In O/W microemulsions the apolar nanodroplets are dispersed in a continuous water phase while in W/O microemulsions the aqueous phase is dispersed as nanodroplets, surrounded by the surfactant layer, in a continuous apolar media. These micelles can be used as nanoreactors for the synthesis of nanoparticles with low polydispersity [30-32]. The synthesis is carried out by mixing two water-in-oil microemulsions containing the proper reagents and, as the droplets collide and coalesce, the nanoparticles formation takes place [33, 34]. Size, size-distributions and shape of the nanoparticles are determined

by the micelles acting as cages and can be tuned by varying kind and surfactant concentration, water-to-surfactant or water-to-oil ratios and temperature [35]. However, the thermal stability of the microemulsions limits the use of high temperature and often affects then the crystallinity of the final product. Moreover, the yield of nanoparticles is extremely low compared to other techniques and large amounts of solvent are required to synthesize appreciable quantities of material.

Hydrothermal synthesis is a synthetic method in which an aqueous solution of inorganic salts is heated in autoclaves at high pressure increasing, hence, the mixture boiling point. During the heating process, metal hydroxides (intermediate products) evolves to metal oxide nanoparticles [36]. Hydrothermal synthesis can be carried out using other solvents (e.g., ethylene glycol, diethylene glycol) instead of water or a mixture of the two solvents (*solvothermal synthesis*) [37]. Nature and concentration of reagents, temperature and reaction time can be properly modified to tune particle size and shape [38]. Even if this technique allows improving nanoparticles crystallinity, thanks to the higher reaction temperature compared to co-precipitation or microemulsion techniques, it is characterized by slow reaction kinetics that dramatically increases the reaction time. Thus, nanoparticles synthesized by hydrothermal synthesis are often characterized by high polydispersity.

Polyol synthesis is a synthetic method that takes its name from the solvents used for the synthesis of nanoparticles, polyols (e.g. polyethylene glycol). During the heating process the metal precursors create an intermediate complex forming firstly the nuclei and, then, the final nanoparticles. Moreover, polyols act also as reducing agents as well as stabilizers to control particle growth and prevent interparticle aggregation. Size, shape and composition of the nanoparticles can be tuned by varying the reagents,

their concentration, the reaction time and temperature [39]. Thanks to the use of high boiling solvents, this synthesis allows one to obtain nanoparticles with improved crystallinity and relatively low polydispersity [40].

Thermal decomposition of organometallic precursors (metal-carbonyl, metal-acetylacetonate, metal complex with conjugate base of fatty acids, etc.) in high boiling solvents (benzyl ether, phenyl ether, 1-octadecene, etc.) in the presence of surfactants (oleic acid, oleylamine, lauric acid, 1,2-hexadecanediol, etc.) is one of the most effective recently developed synthetic methodologies that guarantees the formation of metallic and transition metal oxides nanoparticles with high control on composition, shape, size and size distribution [41, 42]. Thermal decomposition of organometallic precursors where the metal is in the zero-valent oxidation state (e.g., metal-carbonyl) initially leads to a formation of metal nanoparticles that, if followed by an oxidation step, can lead to high quality monodispersed metal oxides [43]. On the other hand, decomposition of precursors with cationic metal centres (e.g., metal-acetylacetonate) leads directly to metal oxides nanoparticles [44]. Although the role played by the different synthetic parameters on the formation of nanoparticles is still under investigation, some models reported in the literature are used to describe the growth mechanism of nanocrystals. Kwon and Hyeon [45], starting from the well-known model proposed by La Mer [46] to describe the growth of monodisperse particles, have recently developed a kinetic model for the thermal decomposition process. In this model three different phases are identified:

I. The thermal decomposition of the precursor, *P*, (e.g. metal acetates, metal acetylacetonates, metal carbonyls) generates reactive species that

form complexes with the surfactant molecules. These complexes are called monomers, *M*:

$$\text{Phase I, } P \rightarrow M$$

II. The second phase consists in the nucleation process, in this step crystals, *C*, are formed starting from the monomers:

$$\text{Phase II, } xM \rightarrow C_x$$

where C_x indicates a crystalline nanoparticle of *x* monomers. In this step the number of nuclei generated per unit of time follows an Arrhenius law.

III. In the third phase, the crystalline nanoparticles can either grow thanks to the addition of other monomers, or dissolve, depending on the supersaturation conditions and on the particle size:

$$\text{Phase III, } C_x + yM \leftrightarrow C_{(x+y)}$$

Regarding this last phase, Talapin et al. [47] have developed a kinetic equation describing the growth rate of nanocrystals. This equation has also been adopted by Kwon and Hyeon [45] to simulate the kinetics of the whole process and to accurately reproduce the experimental results (Figure 2.4).

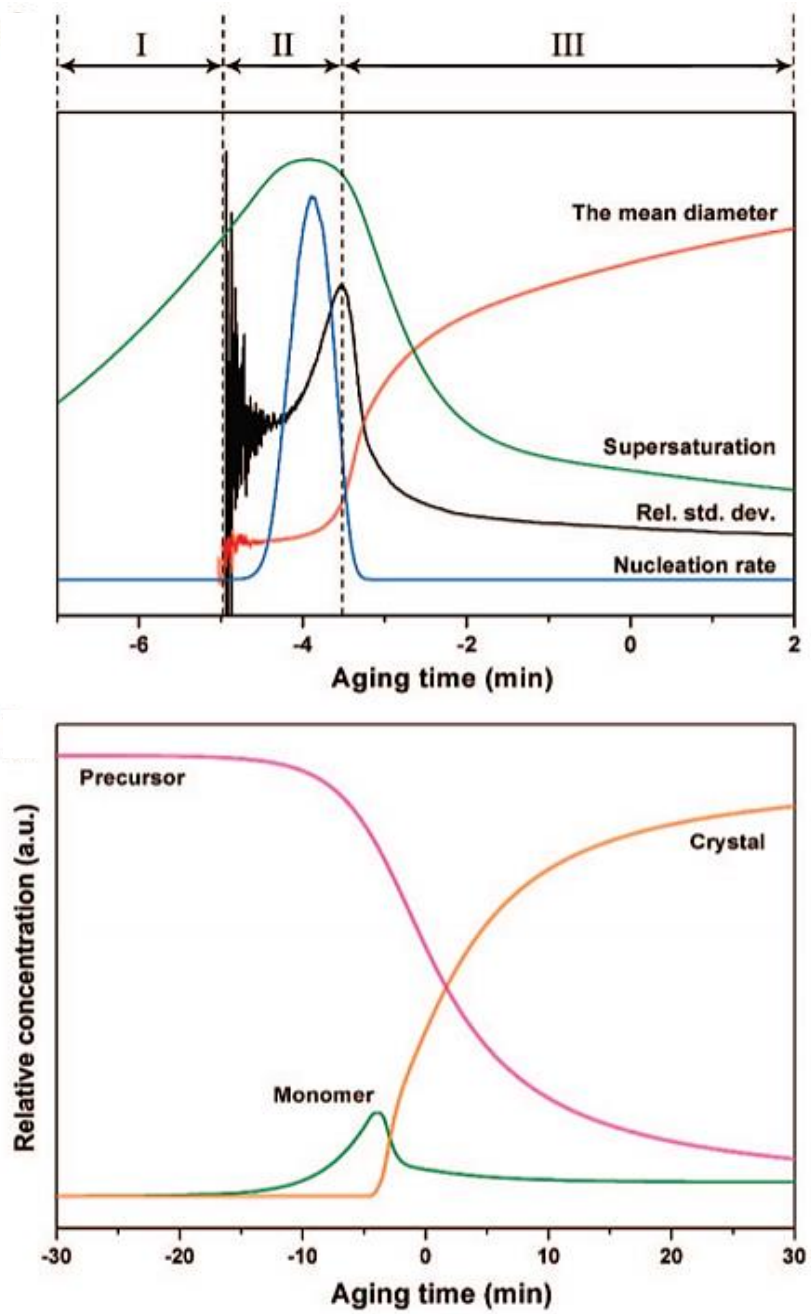

Fig. 2.4. Temporal changes of various parameters (monomers, precursors and nanoparticles concentration) involved in the thermal decomposition process obtained according to the simulation of Kwon and Hyeon [45].

According to this model, the nucleation process starts when the monomer concentration exceeds the saturation value (supersaturation). This causes a drastic reduction of the monomer concentration with consequent dissolution of the smaller and unstable nuclei, while those of larger dimensions are sufficiently stable until the end of the nucleation process. At the beginning of the third phase, supersaturation level is still enough to guarantee the growth of the nanoparticles by the diffusion of the monomers through the solution. In this step larger nanoparticles grow faster than the smaller ones thus, a rapid increase in the average diameter and a narrowing of the size distribution is observed.

Analysing these models, it is easy to understand how many synthetic parameters are involved in the thermal decomposition process and which ones play a critical role to control size, size distribution, morphology and composition of the obtained nanoparticles [48]. Principally, precursor concentration, precursor/surfactant ratio, type of surfactant and solvent are the decisive parameters for controlling the size and morphology of the obtained nanoparticles. Moreover, the reaction time and temperature, the heating rate and the aging time are also critical parameters [49, 50]. Thus, the mechanism of formation of nanoparticles is composed of two main processes, nucleation and growth [51–53], and one way to synthesize monodisperse nanoparticles is to separate the two processes. “Hot-injection” and “heating-up” are two different synthetic techniques that use this approach. Hot-injection consists of injecting the precursors into a hot solution to force a burst nucleation by the high degree of supersaturation occurring after the addition of the precursors. During the nucleation process, in fact, the monomers concentration sharply decreases and, thus, nucleation rate decays [54, 55]. Instead, in the heating-up method, precursors, surfactants and solvent are vigorously mixed at room

temperature and subsequently heated up to the desired decomposition temperature at which the nucleation occurs and, at the same time, the supersaturation decreases (Figure 2.5) [56-58].

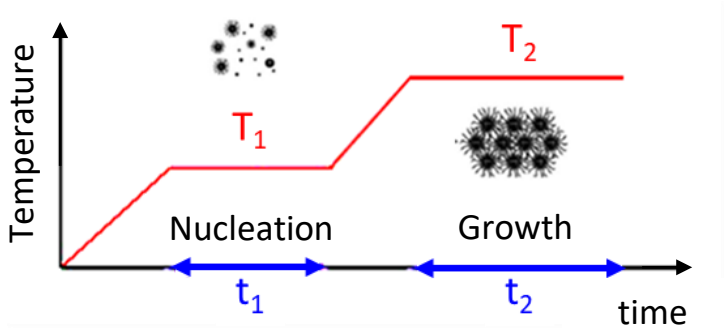

Fig. 2.5. Schematic representation of the separation of nucleation and growth steps through temperature control during the heating procedure used in the thermal decomposition synthesis.

High temperature during nucleation process (T_1) will promote the formation of a high number of nuclei, while an increase in the temperature during the growth step (T_2) results in an enhancement of dissolution of smaller nanoparticles. This means that by using high T_1 smaller particles will be obtained, while with high T_2 larger particles will be produced. Since the temperature that can be reached depends on the solvent used, its choice is an important parameter to determine the final particle size. It has been indeed, observed that by increasing the boiling point of the solvent, larger nanoparticles can be obtained [48].

Besides temperature, also the reaction time can be varied: by increasing the aging time (t_2) larger nanoparticles are obtained while the size-distribution becomes narrower. In fact, as described previously, the smaller nanoparticles dissolve and provide new monomer for further

growth of the larger. On the other hand, short nucleation time (t_1) limits heterogeneous nucleation. Thus, an optimal way to synthesize monodisperse nanoparticles is by using short t_1 and long t_2 [48].

Another important parameter is the type of surfactant used in the synthetic process. In fact the surfactant strongly affects both monomer reactivity and particle surface energy, controlling, thus, the entire crystal growth process [59, 60]. In fact, the surfactant is involved both in the nucleation process, forming an intermediate complex with the precursor, and in the growth step, where it acts as stabilizing agent preventing nanoparticles agglomeration. Therefore, as the interaction between surfactant and precursor becomes stronger, the lower will be the reactivity of the intermediate and the higher the T_1 and T_2 necessary for nucleation and growth processes to occur, and *vice versa*. Similarly, the strength of the interaction between surfactants and nanoparticles surface determines the growth rate of nanoparticles: surfactants that weakly binds the surface (e.g. trioctyl phosphinoxide (TOPO) or amines) allow a fast growth, while surfactants that strongly bind the surface (e.g. oleic acid), slow down the growth of nanoparticles [60, 61]. Moreover, exploiting the different affinity of surfactants for different crystallographic faces, it is also possible to tune nanoparticle shape, as, for example, lower affinity faces will grow faster [52]. Regarding the choice of the surfactant, it is important to mention that longer hydrocarbon chains lead to an increase in the average diameter of the nanoparticles [48]. This effect is attributed to the increased decomposition temperature of the precursor as the number of carbon atoms increases; in the limit case of a surfactant with a decomposition temperature lower than nucleation temperature, no nanoparticles will form. Finally, another important parameter to control size, size

distribution, morphology and composition of the nanoparticles is the precursor/surfactant ratio [48, 62-65].

References

[1] R. W. G. Wyckoff, *Crystal structures, vol. 3*, Interscience Publishers, a division of John Wiley & Sons, 2th edition **1982**.

[2] http://www.cdti.com/spinel/.

[3] D. Carta, M. F. Casula, A. Falqui, D. Loche, G. Mountjoy, C. Sangregorio, A. Corrias, *J. Phys. Chem. C* **2009**, 113, 8606.

[4] X. Zuo, A. Yang, S. Yoon, J. A. Christodoulides, V. G. Harris, C. Vittoria, *J. Appl. Phys.* **2005**, 97, 10G103.

[5] S. Li, L. Liu, V. T. John, C. J. O'Connor, V. G. Harris, *IEEE Trans. Magn.* **2001**, 37, 2350.

[6] Z. J. Zhang, Z. L. Wang, B. C. Chakoumakos, J. S. Yin, *J. Am. Chem. Soc.* **1998**, 120, 1800.

[7] B. Jeyadevan, K. Tohji, K. Nakatsuka, A. Narayanasamy, *J. Magn. Magn. Mater.* **2000**, 217, 99.

[8] C. S. Hurlbut, W. E. Sharp, *Dana's minerals and how to study them*, John Wiley and Sons **1998**.

[9] P. Wasilewski, K. Günther, *Geophys. Res. Lett.* **1999**, 26, 2275.

[10] R. J. Harrison, R.E. Dunin-Borkowski, A. Putnis, *PNAS* **2002**, 99, 16556.

[11] R. Wiltschko, W. Wiltschko, *Biosensors* **2014**, 4, 221.

[12] H. St. C. O. Neil, A. Navrotsky, *American Mineralogist* **1983**, 68, 181.

[13] G. Muscas, N. Yaacoub, G. Concas, F. Sayed, R. Sayed Hassan, J. M. Greneche, C. Cannas, A. Musinu, V. Foglietti, S. Casciardi, C. Sangregorio, D. Peddis, *Nanoscale* **2015**, 7, 13576.

[14] K. J. Klabunde, *Nanoscale Materials in Chemistry*, Wiley-Interscience **2001**.

[15] A. L. Rogach, D. V. Talapin, E. V. Shevchenko, A. Kornowski, M. Haase, H. Weller, *Adv. Funct. Mater.* **2002**, 12, 653.

[16] T. Hyeon, *Chem. Comm.* **2003**, 8, 927.

[17] G. Schmid, *Nanoparticles: From Theory to Application*, Wiley-VCH **2004**.

[18] J. H. Fendler, *Nanoparticles and Nanostructured Films: Preparation, Characterization, and Applications*, Wiley-VCH **1998**.

[19] P. Saravanan, R. Gopalan, V. Chandrasekaran, *Defence Science Journal* **2008**, 58, 504.

[20] C. C. Koch, *Ann. Rev. Mater. Sci.* **1989**, 19, 121.

[21] P. Khanna, A. Kaur, D. Goyal, *J. Microbiol. Methods.* **2019**, 163, 105656.

[22] M. Faraji, Y. Yamini, M. Rezaee, *J. Iran. Chem. Soc.* **2010**, 7,1.

[23] A.-H. Lu, E. L. Salabas, F. Schüth, *Angew. Chemie Int. Ed.* 2007, 46, 1222.

[24] H. Iida, K. Takayanagi, T. Nakanishi, T. Osaka, *J. Colloid Interface Sci.* **2007**, 314, 274.

[25] S. Laurent, D. Forge, M. Port, A. Roch, C. Robic, L. Vander Elst, R. N. Muller, *Chem. Rev.* **2008**, 108, 2064.

[26] C. Hu, Z. Gao, X. Yang, *Chem. Phys. Lett.* **2006**, 429, 513.

[27] R. F. Ziolo, E. P. Giannelis, B. A. Weinstein, M. P. O'Horo, B. N. Ganguly, V. Mehrotra, M. W. Russell, D. R. Huffman, *Science* **1992**, 257, 219.

[28] L. Shen, P. E. Laibinis, T. A. Hatton, *Langmuir* **1999**, 15,447.

[29] X. -P. Qiu, *Chinese J. Chem.* **2010**, 18, 834.

[30] M. A. Malik, M. Y. Wani, M. A. Hashim, *Arab. J. Chem.* **2012**, 5, 397.

[31] J. Eastoe, M. J. Hollamby, L. Hudson, *Adv. Colloid. Interf. Sci.* **2006**, 128, 5.

[32] W. Zhang, X. Qiao, J. Chen, *Chem. Phys.* **2006**, 330, 495.

[33] J. A. López Pérez, M. A. López Quintela, J. Mira, J. Rivas, S. W. Charles, *J. Phys. Chem. B.* **1997**, 101, 8045.

[34] P. A. Dresco, V. S. Zaitsev, R. J. Gambino, B. Chu, *Langmuir* **1999**, 15, 1945.

[35] S. Santra, R. Tapec, N. Theodoropoulou, J. Dobson, A. Hebard, W. Tan, *Langmuir* **2001**, 17, 2900.

[36] J. Wang, J. Sun, Q. Sun, Q. Chen, *Mater. Res. Bull.* **2003**, 38, 1113.

[37] F. Gözüak, Y. Köseoğlu, A. Baykal, H. Kavas, *J. Magn. Magn. Mater.* **2009**, 321, 2170.

[38] J. Wang, F. Ren, R. Yi, A. Yan, G. Qiu, X. Liu, *J. Alloys Compd.* **2009**, 479, 791.

[39] F. Fiévet, J. Lagier, B. Blin, B. Beaudoin, M. Figlarz, *Solid State Ionics* **1989**, 32, 198.

[40] D. Jézéquel, J. Guenot, N. Jouini, F. Fiévet, *J. Mater. Res.* **1995**, 10, 77.

[41] T. Hyeon, *Chem. Commun.* **2003**, 8, 927.

[42] J. Park, E. Lee, N. -M. Hwang, M. Kang, S. C. Kim, Y. Hwang, J. -G. Park, H. -J. Noh, J. -Y. Kim, J. -H. Park, T. Hyeon, *Angew.Chem. Int. Ed.* **2005**, 44, 2873.

[43] S. Lefebure, E. Dubois, V. Cabuil, S. Neveu, R. Massart, *J. Mater. Res.* **1998**, 13, 2975.

[44] A. -H. Lu, E. L. Salabas, F. Schüth, *Angew. Chemie Int. Ed.* **2007**, 6, 1222.

[45] S. G. Kwon, T. Hyeon, *Acc. Chem. Res.* **2008**, 41, 1696.

[46] V. K. La Mer, B. H. Dinegar, *J. Am. Chem. Soc.* **1950**, 72, 4847.

[47] D. V. Talapin, A. L. Rogach, M. Haase, H. Weller, *J. Phys. Chem. B* **2001**, 105, 12278.

[48] V. L. Calero-DdelC, A. M. Gonzalez, C. Rinaldi, *J. Manuf. Sci. Eng.* **2010**, 132, 030914.

[49] S. Basak, D. -R. Chen, P. Biswas, *Chem. Eng. Sci.* **2007**, 62, 1263.

[50] R. Massart, E. Dubois, V. Cabuil, E. Hasmonay, *J. Magn. Magn. Mater.* **1995**, 149, 1.

[51] J. Park, J. Joo, S.G. Kwon, Y. Jang, T. Hyeon, *Angew. Chem. Int. Ed.* **2007**, 46, 4630.

[52] P. D. Cozzoli, *Advanced Wet-Chemical Synthetic Approaches to Inorganic Nanostructures,* Transworld Research Network, **2008**.

[53] T. Sugimoto, *Monodispersed Particles*, First Ed., Elsevier, **2001**.

[54] V. F. Puntes, K. M. Krishnan, A. P. Alivisatos, *Science* **2001**, 291, 2115.

[55] T. Hyeon, S. S. Lee, J. Park, Y. Chung, H. Bin Na, *J. Am. Chem. Soc.* **2001**, 123, 12798.

[56] S. Sun, H. Zeng, *J. Am. Chem. Soc.* **2002**, 124, 8204.

[57] S. Sun, H. Zeng, D. B. Robinson, S. Raoux, P. M. Rice, S. X. Wang, G. Li, *J. Am. Chem. Soc.* **2004**, 126, 273.

[58] J. Park, K. An, Y. Hwang, J. -G. Park, H. -J. Noh, J. -Y. Kim, J. -H. Park, N. -M. Hwang, T. Hyeon, *Nat. Mater.* **2004**, 3, 891.

[59] M. F. Casula, Y. -W. Jun, D. J. Zaziski, E. M. Chan, A. Corrias, A. P. Alivisatos, *J. Am. Chem. Soc.* **2006**, 128, 1675.

[60] C. B. Murray, S. Sun, H. Doyle, T. Betley, *MRS Bull.* **2001**, 26, 985.

[61] A. C. S. Samia, J. A. Schlueter, J. S. Jiang, S. D. Bader, C. -J. Qin, X. -M. Lin, *Chem. Mater*. **2006**, 18, 5203.

[62] W. W. Yu, J. C. Falkner, C. T. Yavuz, V. L. Colvin, *Chem. Commun.* **2004**, 20, 2306.

[63] M. Yin, A. Willis, F. Redl, N. J. Turro, S. P. O'Brien, *J. Mater. Res.* **2004**, 19, 1208.

[64] E. Kang, J. Park, Y. Hwang, M. Kang, J. G. Park, T. Hyeon, *J. Phys. Chem. B* **2004**, 108, 13932.

[65] X. Teng, H. Yang, *J. Mater. Chem.* **2004**, 14, 774.

Chapter 3

Ferrite based MNPs for biomedical applications

As already discussed in the introduction, MNPs employed as CA and heat mediators are currently made of iron oxides with a spinel structure, magnetite (Fe_3O_4) and maghemite (γ-Fe_2O_3), that present low toxicity, are biocompatible and biodegradable and have good magnetic properties, both in terms of magnetic moment and anisotropy. However, the clinical application of MFH is still severely limited by the low amount of heat that can be produced into the tumour mass by the currently used MNPs, because the amount of magnetic material to be collected at the target tissue is very high. The hyperthermic efficiency of the materials is usually expressed in term of Specific Absorption Rate (SAR), defined as the energy converted into heat per mass unit (W/g) [1]. For Fe_3O_4 and γ-Fe_2O_3 MNPs, exposed to analternating magnetic field of appropriate intensity and frequency to maintain the $H_0\nu$ product below the tolerance threshold of 5×10^9 $Am^{-1}s^{-1}$, the SAR values range between 10 and 200 W/g and the maximum values are obtained for 15-20 nm Fe_3O_4 MNPs and 20-25 nm γ-Fe_2O_3 MNPs [2-4]. For this reason, researchers are looking for alternative materials with reduced size and improved hyperthermic properties and consequently, longer circulation time, increased probability to reach the target and reduced quantity of material introduced in the human body [5, 6]. A possible way to realize this purpose is the doping of magnetite with other divalent metal ions for improving the magnetic properties, which are strongly related to the hyperthermic and relaxometric efficiency. In fact,

according to the Rosensweig model (see § 3.3.1) [1], for a dispersion of superparamagnetic NPs exposed to an alternate magnetic field, the absorbed power depends on the anisotropy energy and the magnetic moment of the material and according to Ref. [7, 8] the nuclear transverse relaxivities r_2 depends on the square of the saturation magnetization, M_S. As already reported [9], the increase of the magnetic anisotropy, K, by the partial substitution of Fe^{2+} with Co^{2+} in iron oxide nanoparticles (NPs) of size lower than 10-12 nm leads to a significant improvement of the hyperthermic and relaxometric capability [10, 11]. This issue is relevant when the size constrain is crucial as for obtaining a long circulation time in the body or to overcome the physiological barriers [12]. As discussed above, another important magnetic parameter that can be tuned for increasing the efficiency of most applications, included hyperthermia and MRI, is the M_S. A strong enhancement of M_S has been reported after the introduction of Zn^{2+} in magnetite or cobalt ferrite [12-15] due to cation rearrangement in the spinel lattice. In bulk materials, indeed, a gradual increase of M_S is expected with the progressive introduction of diamagnetic Zn^{2+} ions. Since the latter tend to occupy tetrahedral (T_d) sites, the antiferromagnetic coupling between Fe^{3+} in T_d and octahedral (O_h) sites is partially removed and the sublattices more unbalanced. However, this mechanism holds up until the Zn^{2+} substitution reaches *ca*. half of the total number of divalent ions [16]. For higher percentage, M_S starts decreasing, due to the weakening of the magnetic exchange between T_d and O_h sites, which induces the destabilization of the ferrimagnetic order and the local canting of the spins in the O_h sites. Co-Zn ferrite NPs have been proposed as efficient hyperthermia mediators and MRI contrast agents, since the combined effect of increasing K by introducing Co^{2+} and M_S by Zn^{2+} substitution is expected to produce an enhancement of the

hyperthermic and relaxometric efficiencies of iron-oxide based materials. However, at the nanoscale, the increase of spin disorder due to the weakening of magnetic exchange coupling becomes particularly relevant and can nullify the benefit when temperatures as those related to clinical applications are considered (300-350 K). Notwithstanding this effect, surprisingly high values of M_S at room temperature (117 emu/g,) have been reported for 15 nm NPs of zinc ferrite ($Zn_yFe_{3-y}O_4$) for y=0.4, followed by a significant decrease for further Zn inclusion [12]. Zn substituted cobalt ferrite NPs ($Co_xZn_yFe_2O_4$, where x+y=1) showed a similar trend, reaching the maximum (≈ 90 emu/g) at y = 0.3 at room temperature [17]. The aim of the work here presented was a systematic investigation of the magnetic, hyperthermic and relaxometric properties of $Co_xZn_yFe_{3-(x+y)}O_4$ NPs synthesized by thermal decomposition, with very similar average size (8-9 nm) in order to shed light on the effect of the progressive Zn^{2+} substitution on cobalt ferrite properties. Contrary to most of the literature on this subject, where the total amount of Co+Zn is kept constant while varying Co- and Zn-contents simultaneously ($Co_xZn_yFe_2O_4$, with x+y=1), here the Co-content was fixed to *ca*. x=0.6, corresponding to the highest value of magnetic anisotropy for non-stoichiometric cobalt ferrite [9], and the amount of Zn was varied up to y=0.4, for which the maximum of saturation magnetization is expected in bulk material. This approach allowed us to better evaluate the peculiar role of Zn inclusion on the magnetic properties of the system, which is otherwise masked by any modification in the Co content. NPs were synthesized through thermal decomposition of metal acetylacetonates in high-boiling solvents in the presence of surfactants. As discussed in the previous Chapter, this technique allows an excellent control on the composition and mean size, which was kept constant all along the NPs series (8 nm and 9 nm). This is

a crucial issue that allows to neglect the strong dependence of the magnetic properties on the NPs volume and focusing the comparison on the variation introduced by the different composition. The synthesized series of $Co_xZn_yFe_{3-(x+y)}O_4$ NPs were characterized by low and high resolution transmission electron microscopy (TEM and HRTEM), X-ray diffraction (XRD), elemental analysis (CHN), inductively coupled plasma - atomic emission spectrometry (ICP-AES), X-ray absorption (XAS), X-ray magnetic circular dichroism (XMCD), magneto-optical spectroscopy and SQUID magnetometry. This detailed characterization allowed us to shed new light on the effect of the Zn substitution on the magnetic properties of spinel ferrite NPs. The heating and relaxometric capability of the $Co_xZn_yFe_{3-(x+y)}O_4$ NPs were then investigated and discussed on the basis of the structural and magnetic results and their potential employment in MRI and MFH applications was assessed.

3.1 Synthesis and structural characterization of $Co_xZn_yFe_{3-(x+y)}O_4$ NPs

The synthesis of the magnetite-doped NPs is described in detail in the Experimental Section. Shortly, the $Co_xZn_yFe_{3-(x+y)}O_4$ NPs and a reference sample (CoFe00) were synthesized by thermal decomposition of iron and cobalt acetylacetonates in benzyl ether in the presence of $ZnCl_2$, oleic acid and oleylamine. In the following, samples will be labeled as CoZnFeyy where yy denotes the zinc content (i.e., y = 0.13 corresponds to yy=13). The label of the 9 nm average size NPs includes the term "_9" at the end. In all samples the amount of cobalt was kept constant at ca. x=0.6, corresponding to the highest magnetic anisotropy, as observed in our

previous work [9]. Instead, the Zn amount, y, was varied in the range 0-0.4, where the maximum increase of saturation magnetization is expected [14]. The stoichiometry of the samples was controlled by adjusting the initial ratio of metal precursors in the synthesis. In order to keep the cobalt content constant (x=0.6) along the series, the ratio Co:Fe was fixed to 1:3.3 for all the samples prepared. On the other hand, the amount of Zn precursor was varied in order to obtain a series with increasing Zn-content up to y=0.40 (Table 3.1).

Sample	mmol $Co(acac)_2 \cdot 2\ H_2O$	mmol $Fe(acac)_3$	mmol $ZnCl_2$
CoFe00	0.198	0.66	0
CoZnFe05	0.198	0.66	0.088
CoZnFe13	0.198	0.66	0.132
CoZnFe27	0.198	0.66	0.558
CoZnFe40	0.198	0.66	0.873

Tab. 3.1. Initial molar amounts of metal precursors used in the synthesis.

The stoichiometry of the as obtained NPs was checked by ICP-AES (see below Table 3.3). The amount of Zn effectively introduced into the spinel lattice was observed to be systematically lower than the amount set in the synthesis. It has already been reported in the literature that, using thermal decomposition technique the stoichiometry of the final product (in terms of relative metal concentration) often does not correspond to that of the initial mixture. This is mostly due to the different kinetics of decomposition of the various metal precursors [18]. Therefore, in order to increase the effective Zn amount in the samples, an excess of Zn precursor was used. The excess was estimated by considering that a linear relationship between the final and starting Zn:Fe atomic ratio, was

experimentally observed, as shown in Figure 3.1. Moreover, in order to increase the size of the particles without affecting the composition, we found easier to replace the cobalt precursor or, alternatively, the zinc one, rather than modifying the other parameters of the synthesis.

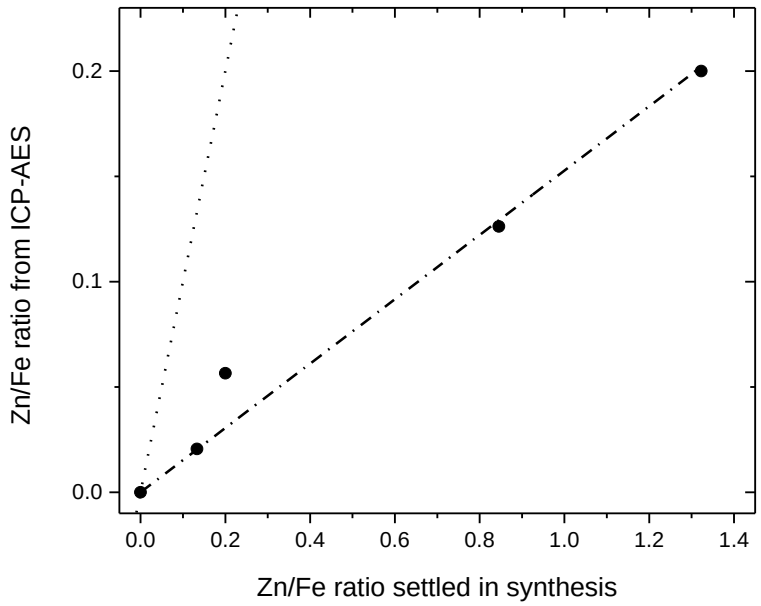

Fig. 3.1. Relationship between initial Zn:Fe ratio and that found in the final product as evaluated by ICP-AES for the 8 nm series. The dashed line represents the fit of the data with a linear relationship, while the dotted line represents the 1:1 correspondence.

The effective stoichiometry of $Co_xZn_yFe_{3-(x+y)}O_4$ NPs evaluated by elemental analysis (ICP-AES) was confirmed for same selected samples by energy dispersive spectroscopy (EDS, Table 3.2). The amount of Fe was found, within the experimental error, almost identical to that calculated using the formula 3-(x+y).

Sample	*Fe atomic %*	*Zn atomic %*	*Co atomic %*
CoZnFe13	74.6	4.5	21.0
CoZnFe27	69.2	8.4	22.4
CoZnFe40	66.3	13.3	20.4

Tab. 3.2. Estimation of the atomic percentage of Cobalt, Zinc and Iron of $Co_xZn_yFe_{(3-x-y)}O_4$ NPs obtained by the EDS analysis (the error is estimated as 1%).

The main chemical and structural parameters of the synthesized samples are summarized in Table 3.3.

Sample	d_{TEM} (nm)	d_{XRD} (nm)	a (Å)	x	y	z
CoFe00	8.5 ± 1.9	8.1(6)	8.387(1)	0.61	0	2.40
CoZnFe05	7.9 ± 2.0	8.5(5)	8.394(1)	0.52	0.05	2.42
CoZnFe13	8.0 ± 1.9	8.7(5)	8.399(1)	0.57	0.13	2.28
CoZnFe27	7.6 ± 1.7	6.7(6)	8.406(3)	0.59	0.27	2.11
CoZnFe40	8.2 ± 1.8	8.7(5)	8.419(1)	0.60	0.40	1.99

Tab. 3.3. Chemical and structural properties of $Co_xZn_yFe_{3-(x+y)}O_4$ NPs. d_{TEM}: NPs average diameter and standard deviation obtained from TEM analysis; d_{XRD}, a: crystallite mean size and lattice parameter obtained from XRD data analysis (errors on the least significant digit are reported in brackets); x, y, z: Co, Zn and Fe content obtained from ICP analysis.

TEM images are reported in Figure 3.2, together with the NPs size distributions, fitted to a log-normal function. All samples are composed of almost spherical NPs of *ca.* 8 nm diameter. Mean and standard deviation values are statistically evaluated from the size histograms.

Only the cubic ferrite phase is observed in the XRD patterns (Figure 3.3): this suggests that the introduction of Zn in the reaction pool does not induce the formation of secondary phases other than the spinel. The lattice parameter increases with Zn-content (Figure 3.4 and Table 3.3) in agreement with literature data on bulk and nanostructured mixed cobalt zinc ferrites [16, 19], confirming that the Zn^{2+} ions are effectively incorporated in the ferrite lattice. Moreover, the theoretical estimation of the variation of the lattice parameter, *a*, with the metal ion distribution among different cavities, performed following the model proposed in Ref. [20] and using the expression:

$$a = \frac{8}{9}\sqrt{3}\left[\left(r_A + \sqrt{3}r_B\right) + \left(1 + \sqrt{3}\right)R_0\right] \qquad (3.1)$$

where R_0 is the ionic radius of the O^{2-} ion while r_A and r_B are the ionic radii of the T_d e O_h sites averaged over the cation distribution, shows that a linear increase, as the one here observed, is possible only if Zn^{2+} ions replace Fe^{3+} in T_d cavities. Finally, the good agreement between the average NPs diameter obtained from TEM and the crystal grain size from XRD measurements (Table 3.3) suggests that all samples are composed by highly ordered, single crystal NPs. The high crystallinity and the cubic spinel structure of the NPs are nicely confirmed by high resolution TEM images and electron diffraction patterns of some selected samples, shown in Figure 3.5.

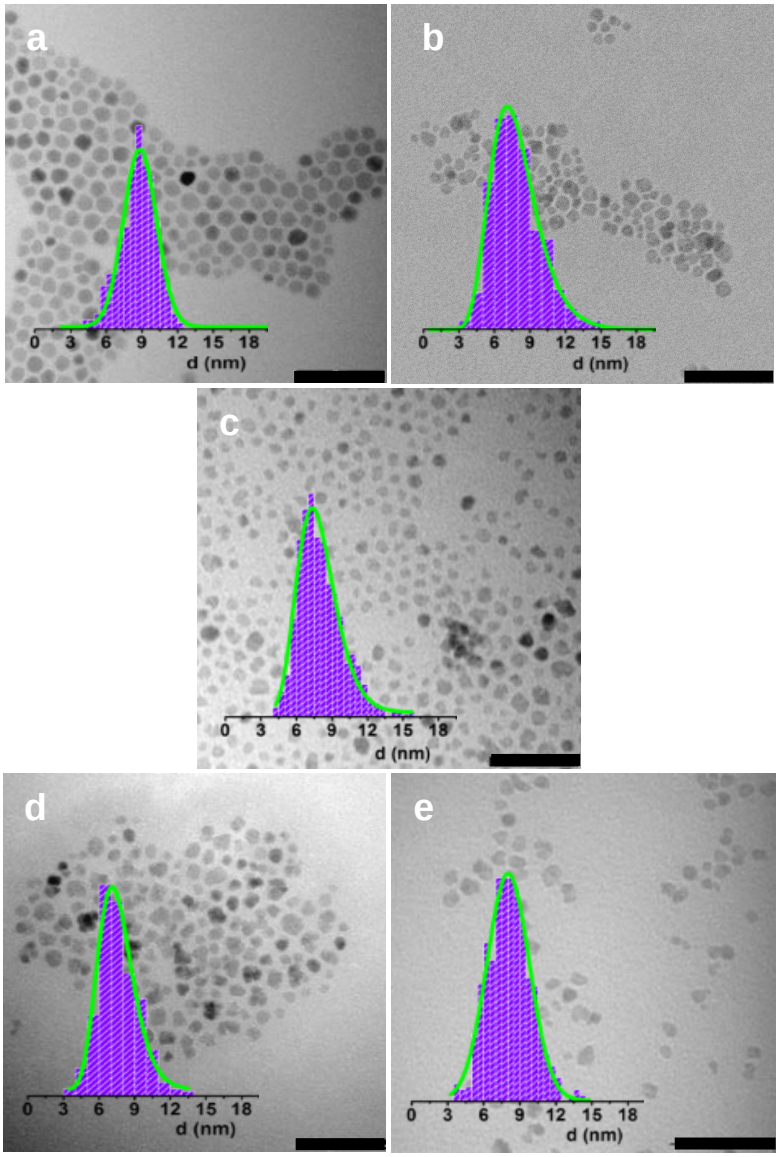

Fig. 3.2. TEM images of $Co_xZn_yFe_{3-(x+y)}O_4$ NPs: a) CoFe00 (d = 8.5 ± 1.9 nm), b) CoZnFe05 (d = 7.9 ± 2.0 nm), c) CoZnFe13 (d = 8.0 ± 1.9 nm), d) CoZnFe27 (d = 7.6 ± 1.7 nm), e) CoZnFe40 (d = 8.2 ± 1.8 nm). In the insets, the corresponding diameter distribution evaluated over 700-750 NPs is reported. The continuous line represents the best-fit curve to a lognormal distribution. The scale bar corresponds to 50 nm.

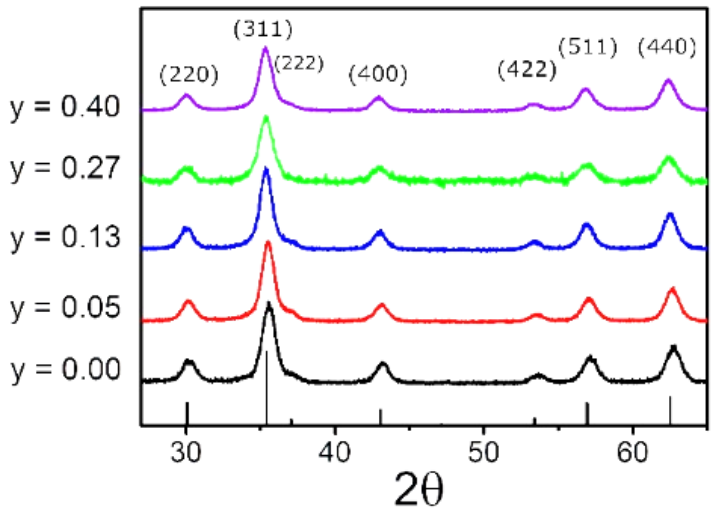

Fig. 3.3. X-ray diffraction patterns of $Co_xZn_yFe_{3-(x+y)}O_4$ NPs compared to the reference pattern of cobalt ferrite (black bars).

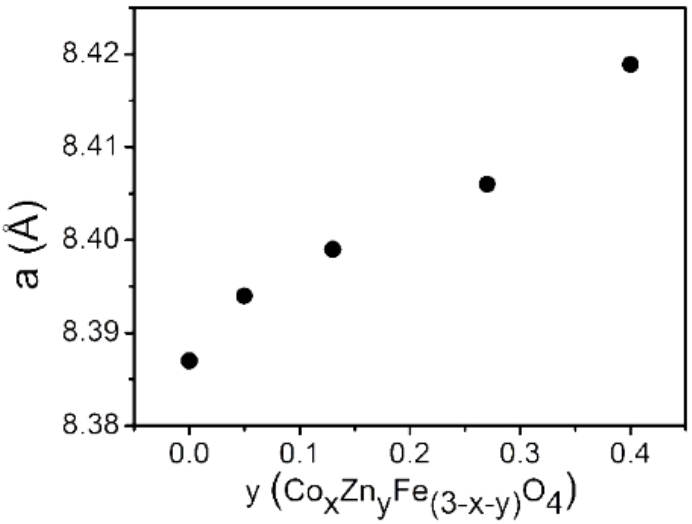

Fig. 3.4. Lattice parameter dependence on the Zn-content, y (error is within 0.003 Å).

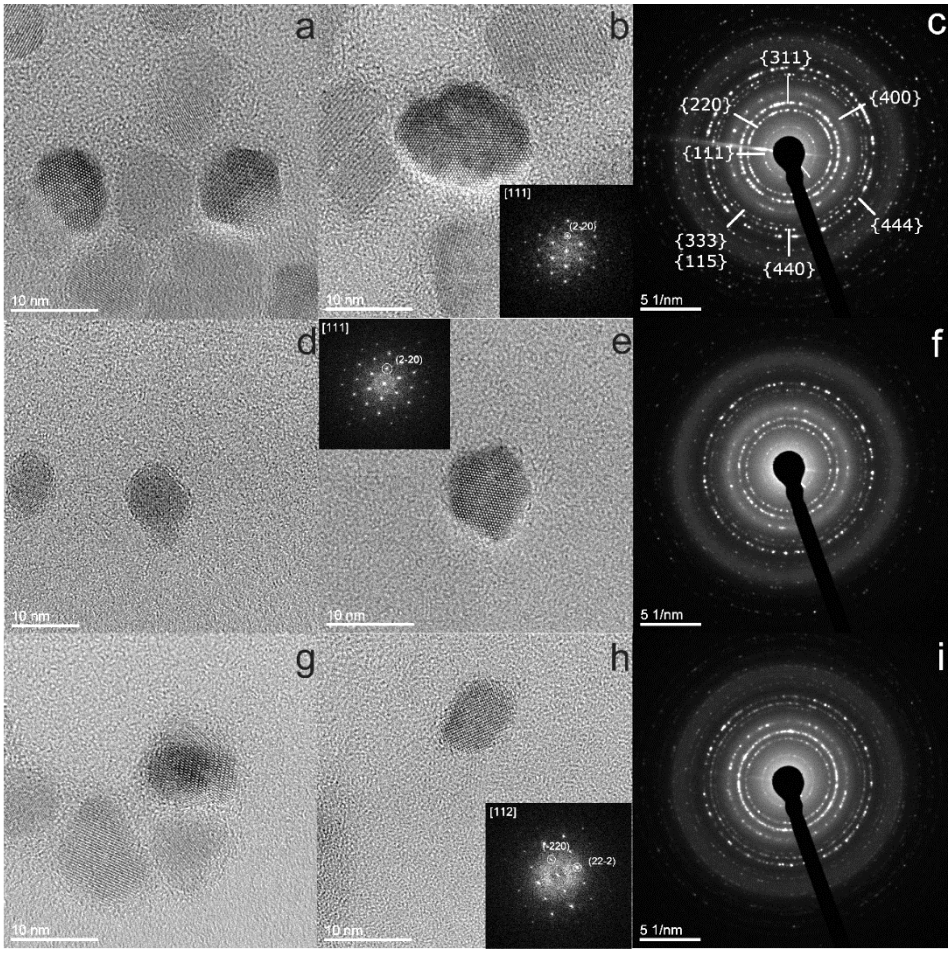

Fig. 3.5. High-resolution images (a, b, d, e, g, h) and electron diffraction (c, f, i) of samples CoZnFe13 (a, b, c), CoZnFe27 (d, e, f) and CoZnFe40 (g, h, i). In the inset of (b, e, h) the fast fourier transform (FFT) acquired on a single particle is reported.

3.2 Magnetic and magneto-optical characterization of $Co_xZn_yFe_{3-(x+y)}O_4$ NPs

To evaluate the effect of the Zn substitution on the magnetic and the magneto-optical properties of spinel ferrite NPs, SQUID magnetometry, XMCD and magneto-optical spectroscopy were performed. Magnetic measurements were carried out using two SQUID magnetometers, a Quantum Design MPMS and a Cryogenic Ltd. S600. For magnetic measurements, powder samples were hosted in a teflon tape and then pressed in a pellet to prevent preferential orientation of the nano-crystallites under the magnetic field. The magnetization values were normalized by the weight of ferrite present in the sample subtracting the surfactant percentage obtained by CHN analysis. In Figure 3.6 the field dependence of the magnetization at low temperature (5 K) is reported.

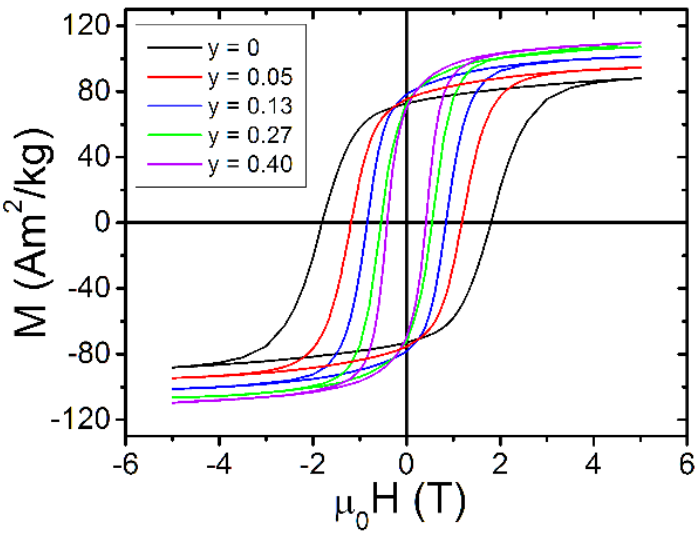

Fig. 3.6. Hysteresis loops of $Co_xZn_yFe_{3-(x+y)}O_4$ NPs measured at 5 K.

The values of coercive field, H_C, the magnetization at 5 T, M_{5T}, and the reduced remnant magnetization, $M_R=M_{0T}/M_{5T}$, are reported in Table 3.4.

Sample	μ_{tot}	T_B (K)	M_{5T} 5 K (Am^2/kg)	M_{5T} 300 K (Am^2/kg)	$\mu_0 H_C$ 5 K (T)	M_R 5 K	M_S calc. (Am^2/kg)	SAR (W/g_{Me})
CoFe00	3.39	285	88	76	1.87	0.82	81.1	17.2 ± 2.4
CoZnFe05	3.78	~350	95	81	1.18	0.79	90.4	52.6 ± 1.3
CoZnFe13	4.21	340	101	80	0.84	0.77	100.3	46.1 ± 3.7
CoZnFe27	5.03	280	107	78	0.55	0.67	119.1	25.7 ± 4.5
CoZnFe40	5.80	250	110	71	0.42	0.63	136.6	35.5 ± 0.7

Tab. 3.4. Magnetic and hyperthermic parameters of $Co_xZn_yFe_{3-(x+y)}O_4$ NPs. μ_{tot}: average magnetic moment in μ_B units per formula unit evaluated as $\mu = (4\text{-}x+6y)\mu_B$; T_B: blocking temperature (estimated errors less than 2%); M_{5T}: experimental magnetization measured at 5T; H_C: coercive field; M_R: reduced remnant magnetization; M_S calc. (calculated): theoretical value of saturation magnetization; *SAR*: Specific Absorption Rate (SAR) values per gram of metal (Co+Zn+Fe) obtained by applying an alternating magnetic field of 12 kA/m and 183 kHz. Errors on experimental measurement of M_{5T} and H_C can be estimated less than 1‰.

At low temperature, a monotonous increase of M_{5T} with the Zn-content is observed (Fig. 3.7).

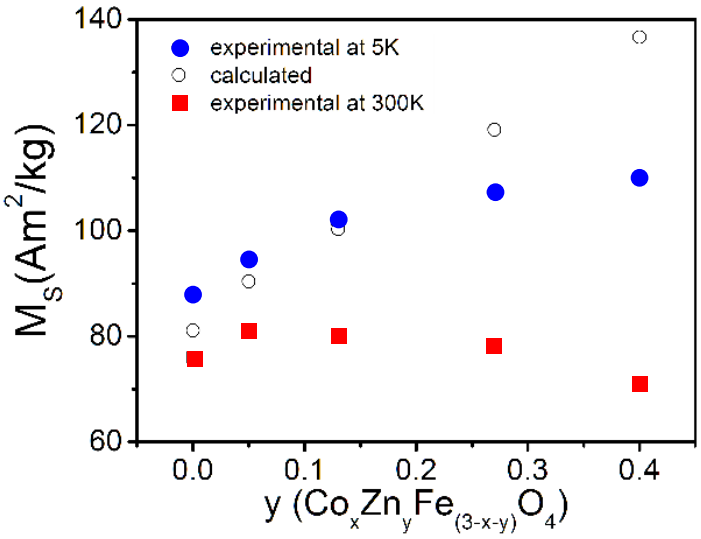

Fig. 3.7. Saturation magnetization dependence on the Zn-content, *y*: experimental (blue circles: 5 K; red squares: 300 K) and calculated (open circles). The experimental M_S was approximated to the high field (5 T) values.

This behavior can be explained by a simple model which estimates the total magnetic moment from the ion population occupying T_d and O_h sites of an inverse spinel ferrite lattice. As discussed in the previous chapter, in spinel ferrites Fe^{3+} and M^{2+} transition metal ions occupy part of the tetrahedral (T_d) and octahedral (O_h) cavities generated by the arrangement of oxygen ions in the *fcc* structure. Depending on the distribution of metal ions among the different sites, ferrites are classified as normal or inverse spinels. The iron oxide magnetite (Fe_3O_4) has the structure of inverse spinel, $B(AB)O_4$. Considering only the spin contribution, the total

magnetic moment of a single iron ion is 4 μ_B for Fe^{2+} and 5 μ_B for high spin Fe^{3+}. In spinel ferrites the total magnetic moment arises from the antiferromagnetic coupling of the two ferromagnetically ordered tetrahedral and octahedral sublattices (Figure 3.8a), and therefore in magnetite the resulting net magnetic moment per formula unit, μ, is 4 μ_B. In non-stoichiometric cobalt ferrite of formula $Co_xFe_{1-x}Fe_2O_4$, the progressive substitution of Fe^{2+} with Co^{2+} leads to a small decrease of μ depending on the degree of cobalt substitution *x*. In fact, considering a complete inverted spinel structure with all the Co^{2+} ions located in the octahedral sites and the same spin coupling scheme of magnetite (Figure 3.8b), the net magnetic moment for formula unit will be $(4-x)\mu_B$ which, for x=0.6 corresponds to $\mu = 3.4\ \mu_B$. Following the same argumentation, a further decrease of the net magnetic moment would be expected in the case of $Co_xZn_yFe_{1-(x+y)}Fe_2O_4$, due to the diamagnetic nature of the Zn^{2+} ion (μ=0). However, Zn^{2+} ions have a strong affinity for T_d sites [21] and then their introduction in the spinel lattice causes the replacement of a Fe^{3+} ions in T_d cavity, and its migration in an O_h site, as schematized in Figure 3.8c. We wish to stress that in our case this hypothesis is well confirmed by XRD and MCD data (discussed below) as well as by literature [17, 19, 22]. This migration modifies the balancing of the magnetic moments, which is now given by the relation:

$$\mu = 5\,(1+y) + 3x + 4\,(1-x-y) - 5\,(1-y) = (4-x+6y)\mu_B \qquad (3.2)$$

Thus, considering only the spin contribution, the resulting magnetic moment per formula unit is $\mu = (4 - x + 6y)\ \mu_B$, which, for a constant Co content x = 0.6 reduces to $\mu = (3.4 + 6y)\ \mu_B$.

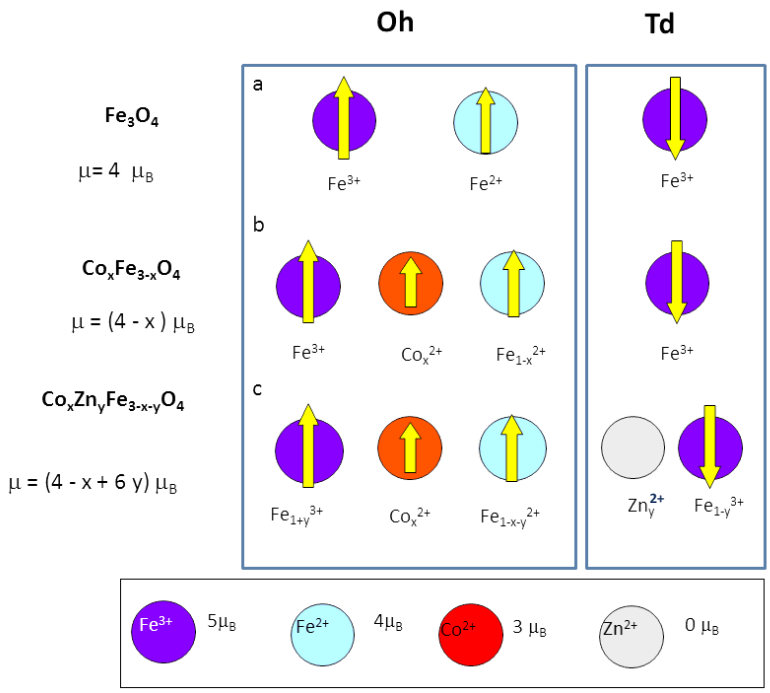

Fig. 3.8. Scheme of the ion distribution between T_d and O_h sites for: a) magnetite, b) cobalt ferrite, c) zinc doped cobalt ferrite. Colored circles denote different ions as reported in the bottom raw; the strength and direction of the ion magnetic moment is represented by the length and orientation of the superimposed arrow, respectively; μ is the net magnetic moment per formula unit and μ_B is the Bohr magneton ($9.274 \cdot 10^{-24}$ J/T).

In Figure 3.7 the experimental M_S, approximated by M_{5T}, is compared to the theoretical one, reported as $M_S = \mu_n \mu_B N_A / PM$, where μ_n is the magnetic moment of ferrite in Bohr magnetons, N_A the Avogadro number and PM the molecular weight of $Co_xZn_yFe_{1-(x+y)}Fe_2O_4$ ferrite. A good agreement is observed only for low Zn-content ($y \leq 0.13$), while, for larger y, the experimental values are considerably lower. This deviation can be ascribed to the non-collinear structure of the spins inside the spinel lattice.

Indeed, the progressive introduction of the diamagnetic Zn^{2+} in the T_d sites causes a weakening of the exchange interaction between the O_h and T_d sublattices, leading to a canting of the spins in the O_h sites with a consequent reduction of M_S [14, 23]. A similar non-collinear ordering was previously reported in $Co_{1-y}Zn_yFe_2O_4$ MNPs prepared by different experimental techniques [14, 15, 21, 23]. It can be described with the model of Yafet-Kittel [24], in which the O_h sublattice is further divided in two sub-sublattices, with magnetic moment equal in amplitude but canted in opposite directions by the same angle α_{YK}, with respect to the net magnetization at 0 K. According to this model, the spin canting can be quantified by calculating α_{YK} from the experimental moment as

$$\mu_{exp} = m_{Oh} \cos\alpha_{YK} - m_{Td} \tag{3.3}$$

where m_{Td} and m_{Oh} are the magnetic moments of the T_d and O_h sublattices, respectively. The values of α_{YK} obtained are non-zero only for CoZnFe27 (α_{YK} = 19.7°) and CoZnFe40 (α_{YK} = 29.3°), i.e., for samples with the largest Zn-content. However, it should be noted that small deviations from the assumed cation distribution may also concur to the observed behavior. Unlike the low temperature magnetization curves, the value of M_{5T} at 300 K (Table 3.4 and Figures 3.7 and 3.9) does not show such a monotonous trend along the series.

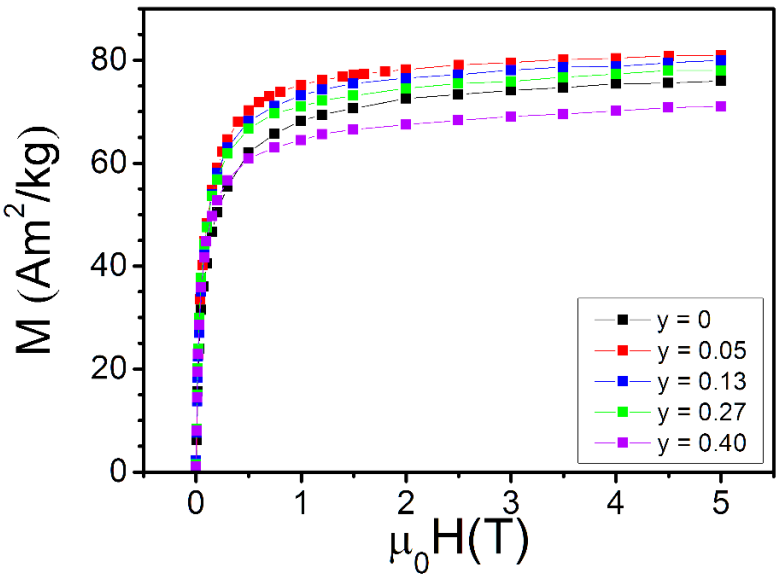

Fig. 3.9. Magnetization curves, *M*(*H*), at room temperature (300K).

The rate of magnetization decreases with temperature, expressed by the ratio R = [1 - M_{5T} (300K)/M_{5T} (5K)], shown in Figure 3.10, is found to increase almost linearly with the Zn-content. For a deeper analysis, the temperature dependences of M_{5T} (Figure 3.11) were fitted to the modified Bloch law $M(T)=M_0[1-(T/T_0)^{\beta}]$, where the scaling temperature, T_0, and the exponent β are free fitting parameters. Even though strong deviations from the Bloch exponent value (β=3/2) [25] are found especially for CoFe00, β shows a clear decreasing trend upon y (Table 3.5). Deviations from the typical Bloch exponent are commonly reported for nanosized systems [26] and are associated to cut-off of the spin wave spectra due to the reduced size of the particles, environmental conditions, like coating, interparticle interactions, or interface effects due to uncompensated layer on the particle surface.

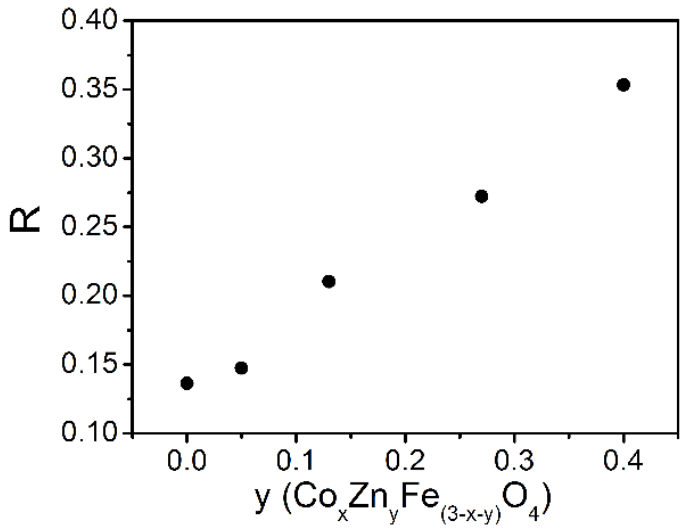

Fig. 3.10. Rate of magnetization decrease with temperature, $R = [1 - M_{5T}(300K)/M_{5T}(5K)]$, of $Co_xZn_yFe_{(3-x-y)}O_4$ NPs as a function of the Zn-content, *y*.

Sample	β	T_0
CoFe00	2.03 (0.07)	773 (23)
CoZnFe05	1.94 (0.03)	784 (13)
CoZnFe13	1.67 (0.02)	762 (7)
CoZnFe27	1.50 (0.006)	716 (3)
CoZnFe40	1.32 (0.009)	707 (6)

Tab. 3.5. Generalized Bloch law best-fit parameters, T_0, β. Fitting errors are reported in brackets.

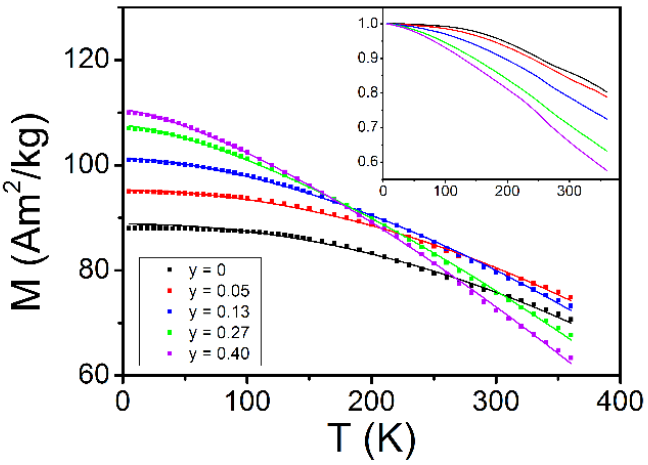

Fig. 3.11. Temperature dependence of the magnetization measured with an applied field of 5 T: continuous lines represent the best fit curves to the generalized Bloch law. In the inset, the curves are normalized to the corresponding M_{5T} measured at 5 K.

In our case, all these factors do not account for the observed trend, which can thus be attributed to the progressive weakening of the magnetic exchange coupling between ions sitting in T_d and O_h cavities, induced by the Zn introduction. Additionally, T_0, reported in Table 3.5, is related to the exchange coupling constant, J, and thus it can be considered as an estimate of the Curie temperature of the material, T_c. As expected for nanosized materials, the estimated T_c is lower than the bulk value (826 K for $Co_{0.6}Fe_{2.4}O_4$, estimated by linear interpolation of bulk cobalt ferrite and magnetite values [27]) and it decreases with Zn-content. Similar findings are reported in the literature, where T_c were directly or indirectly estimated [19]. The different temperature dependence of M_S upon Zn-content thus accounts for the observed trend of M_{5T} at room temperature reported in

Figure 3.7, but, at the same time, partially nullifies the magnetization increase through the introduction of Zn^{2+} ions in the cobalt ferrite lattice foreseen by temperature-independent models, as the one previously adopted.

The influence of the chemical composition on the magnetic anisotropy is investigated by analyzing the reduced remnant magnetization, M_R, and the coercive field, H_C, measured at low temperature (5 K). The decrease of M_R from 0.82 to 0.63 denotes how the cubic symmetry (typical value M_R = 0.83 - 0.87 [28]) of pure cobalt ferrite evolves toward uniaxial one (typical value M_R = 0.5), without reaching it completely. Dealing with MNPs of material with cubic symmetry, the evolution from a high symmetry to a lower one upon the size reduction is generally interpreted as the effect of increasing disorder of the spin alignment, particularly on the NPs surface. The lattice disorder induced by the progressive introduction of Zn^{2+} ions can be therefore the responsible for the observed trend. Assuming the reversal process occurs thorough a coherent rotation of all the spins and that interparticle interactions are weak, the effective anisotropy constant, K, is evaluated from the coercive field at 5 K, as $K = H_C \cdot M_S / f$, where the saturation magnetization is again approximated by M_{5T}(5K), and the factor f is chosen f = 0.64 considering that the anisotropy is mostly cubic and positive [29] The obtained values of K (Table 3.4 and Figure 3.12) show a marked decrease with increasing Zn concentration, particularly significant for the first substitution step for which K is reduced by 45%. Additional information can be obtained by the temperature dependence of the product $H_C \cdot M_S$, which can be associated to K only when the NPs behavior is dominated by the anisotropy energy barrier, E_a, i.e., for temperatures much lower than the blocking temperature, $T_B \propto E_a$ reported in Table 3.4.

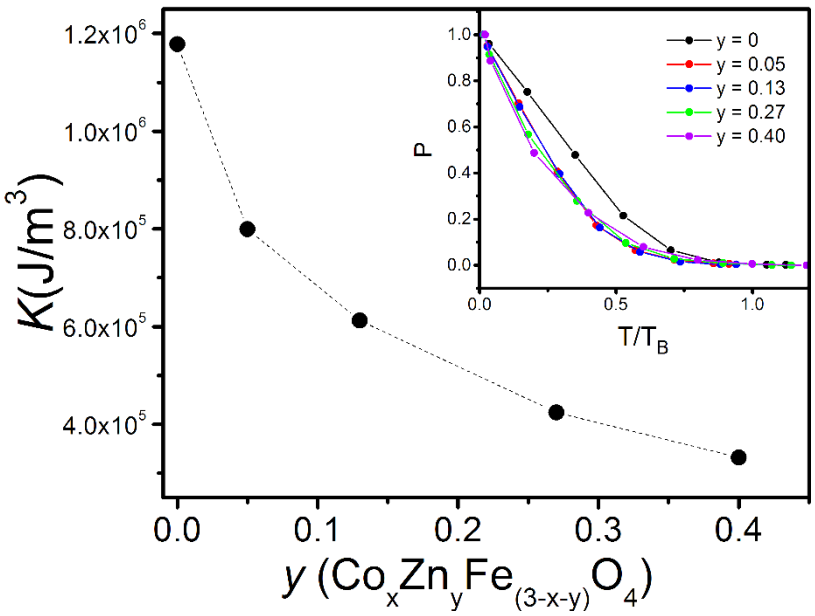

Fig. 3.12. Anisotropy constant K of $Co_xZn_yFe_{(3-x-y)}O_4$ NPs as a function of Zn-content y. In the inset, dependence of the product $P = H_c \cdot M_S$ normalized to 5 K value on the reduced temperature T/T_B. For CoZnFe05 T_B was extrapolated to 350 K from the H_C(T) curve, as $H_C(T \rightarrow T_B) \rightarrow 0$.

By definition, indeed, T_B establishes the onset of the superparamagnetic regime and it is commonly identified as the temperature at which the Zero field cooled (ZFC) curve reaches its maximum, T_{max}, (Figure 3.13) as for $T > T_{max}$, the magnetization behavior tends to follow the Curie law. Zero field cooled/ field cooled (ZFC/FC) curves were obtained by measuring the temperature dependence of the magnetization applying a probe magnetic field (5 mT) after cooling the sample in the absence (ZFC) or in the presence (FC) of the field. When the reduced variable T/T_B is used, all the $H_C \cdot M_S$ data of the doped samples collapse on the same curve, whose

decreasing rate for $T/T_B << 1$, thus relatable to the K decay, is faster than that of the undoped sample (inset of Figure 3.12). The different rescaling between undoped and doped samples suggests that the thermal activated reversal process is modified by the Zn introduction but does not depend on its amount.

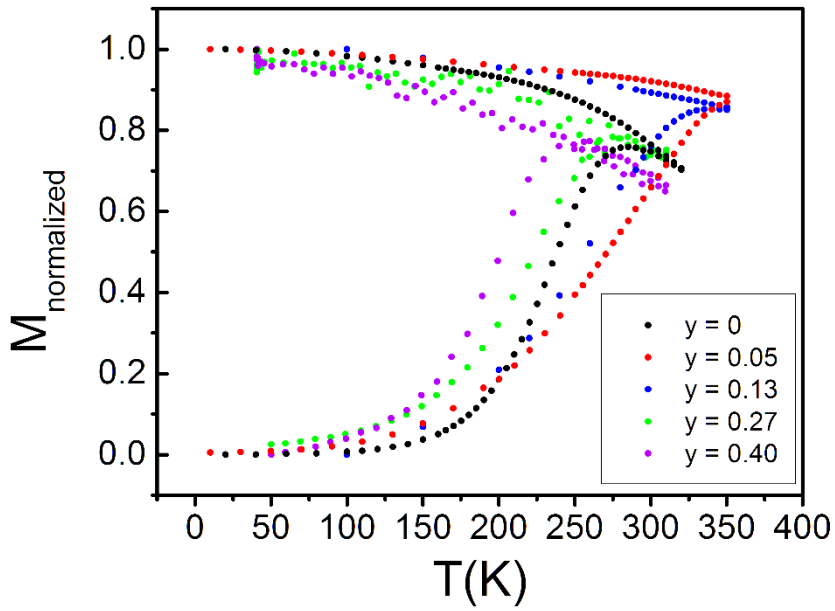

Fig. 3.13. Temperature dependence of the zero field cooled (ZFC) and field cooled (FC) magnetizations for $Co_xZn_yFe_{(3-x-y)}O_4$ NPs, normalized to the maximum of the FC curve. All curves were acquired with a 5 mT probe field.

The observed trend of K with Zn-content can be related to the structural variations induced in the ferrite lattice by the introduction of Zn^{2+} ions. One of the main contributions to the effective anisotropy is, indeed, the magneto-crystalline anisotropy, which, depending on the crystal symmetry

through the spin-orbit coupling, is influenced by local crystal lattice distortions. The introduction of Zn^{2+} in the spinel structure leads to the increase of the lattice parameter, decreasing the crystal field on Co^{2+} ions in O_h sites, thus decreasing their magneto-crystalline anisotropy. Moreover, the introduction of Zn^{2+} ions in T_d cavities causes a rearrangement of the distribution of Fe^{3+}, which eventually can involve Co^{2+} ions, too. This modification in the cation distribution can produce a large variation in the single ion magnetic anisotropy, which can be also responsible for the observed decrease of *K*.

This hypothesis is supported by XMCD experiments, performed on some selected samples, which allowed the evaluation of the orbital, μ_{orb}, and spin, μ_s, components of the mean magnetic moment per ion, μ_i (Table 3.6 and Figure 3.14).

Sample	Fe ion			Co ion		
	μ_{orb}	μ_s	μ	μ_{orb}	μ_s	μ
CoFe00	0	4.0	4.0	0.47	2.9	3.4
CoZnFe05	0	3.6	3.6	0.35	2.1	2.7
CoZnFe27	0	3.6	3.6	0.36	2.3	2.4

Tab. 3.6. Orbital, μ_{orb}, and spin, μ_s components of the mean magnetic moment, μ_i, of Fe and Co ions per formula unit, expressed in μ_B, obtained from XMCD experiment.

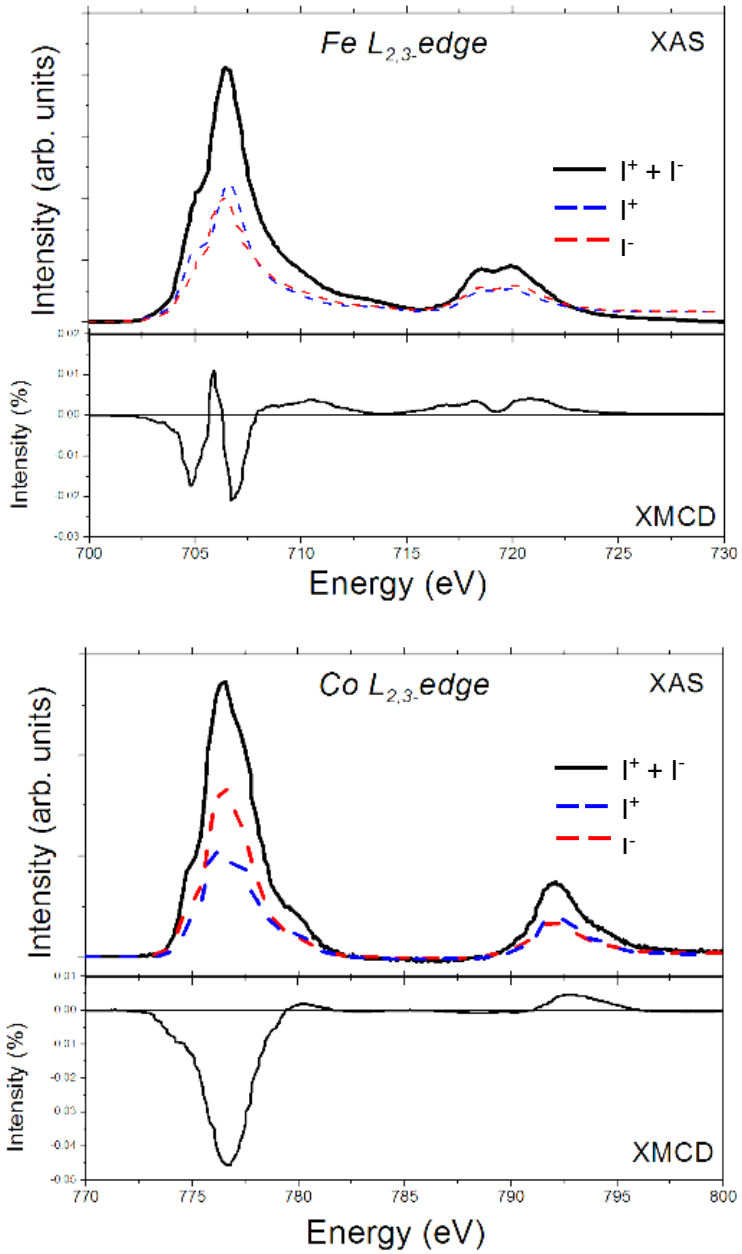

Fig. 3.14. XAS and XMCD spectra at the Fe and Co $L_{2,3}$ edges for sample CoFe00 as representative of the series. I^+ (blue dashed lines), I^- (red dashed lines) and (I^++I^-) (black lines) refers to right, left circularly polarized light and their sum, respectively.

Undoped CoFe00 particles show the expected μ values for cobalt ferrite (4.0 μ_B and 3.4 μ_B for Fe and Co ions, respectively) [30]. The incorporation of Zn^{2+} ions causes a reduction of the μ_i value at the iron edge (3.6 μ_B for y = 0.05 and 0.27) and a more marked decrease for the Co moment (2.7 μ_B for y = 0.05 and 2.4 μ_B for y = 0.27). In particular, considering the μ_{orb} and μ_s contributions separately, the inclusion of small amounts of Zn^{2+} ions cause a strong decrease of μ_{orb} of Co^{2+} ions. Since this is the main contribution to the total magneto-crystalline anisotropy of the structure, the observed reduction (*ca.* 30%), induced by the Zn substitution, can qualitatively account for the *K* trend [31]. We wish to stress here that, although some works report a decrease of *K* with the Zn-content in Co- and Zn- co-doped ferrites [19, 32], they cannot be helpfully compared to our data, since, as already mentioned, they concern materials where the content of Co and Zn is varied simultaneously (x+y=1), so that the effect of increasing Zn-content on the anisotropy is masked by the changes introduced by the amount of the highly anisotropic Co^{2+} ion.

Magneto-optical spectroscopies can give important insight on the structure and composition of spinel ferrite NPs [33, 34]. Room temperature MCD spectra were recorded in the UV-visible range for samples CoZnFe13, CoZnFe27 and CoZnFe40. The representative spectrum of CoZnFe40 is shown in Figure 3.15, along with its extinction spectrum. While the latter is mostly featureless, the MCD spectrum shows distinct peaks, owing to the additional orbital selection rule active in this type of spectroscopy [35]. Three main features dominate the spectra: a broad peak centered roughly at 3.5 eV, ascribed to intersublattice charge transfer (ISCT) transitions involving Fe ions in 2+ and 3+ oxidation states and in both O_h and T_d cavities. The second feature is a peak at 2.2 eV, ascribed to intervalence

charge transfer (IVCT) between Co^{2+} and Fe^{3+} in O_h sites. The peak at 1.7 eV is related to *d-d* transitions from Co^{2+} in T_d cavities [36].

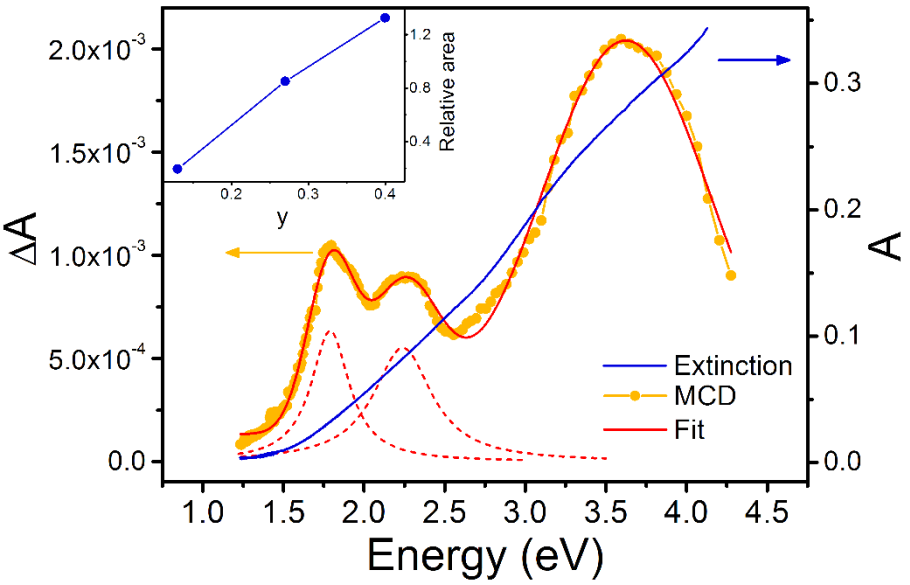

Fig. 3.15. Extinction and MCD spectra of CoZnFe40. The dashed red lines represent the deconvolution of the different transitions contributing to the total spectrum (red line). Inset: ratio between the area of the peak at 1.7 eV and at 2.2 eV for samples with increasing Zn-content.

MCD spectra give us some interesting insight on cation distribution in the series. Firstly, and contrary to common schematizations, the sharp peak at 1.7 eV indicates that at least part of the population of Co^{2+} ions are situated in T_d sites. A quantitative estimate is not straightforward, since several quantities, such as optical oscillator strength and intrinsic magneto-optical activity, are not known for the transition; however, this feature can be taken as a caveat that the base scheme to describe spinel and inverse spinel structures can be over-simplistic. Moreover, while no electronic transition

directly involving Zn^{2+} ions is found in this photon energy interval, we can indirectly follow Zn substitution through the ratio between the peak of tetrahedral Co^{2+} *d-d* transition peak at 1.7 eV and the peak at 2.2 eV related to charge transfer transitions between octahedral $Co^{2+}$and Fe^{3+} sites. According to our schematization, Zn substitution does not influence the distribution of Co^{2+} between O_h and T_d sites. Thus, the intensity of the transition at 1.7 eV involving only tetrahedral Co^{2+} is not influenced by Zn-content. On the other hand, the transition at 2.2 eV involves two types of cations: octahedral Co^{2+} ions, and octahedral Fe^{3+} species. Therefore, the occupation of O_h sites by Fe^{3+} cations increases as Zn is added in the structure, displacing tetrahedral Fe^{3+} ions. As a consequence, the intensity of the IVCT transition at 2.2 eV is expected to increase as Zn amount increases. If an absolute measure of the intensity of such features is not available, as in the present case, the intensity ratio between the transition at 2.2 eV and that at 1.7 eV is a good indicator of Zn^{2+} content in T_d sites. Following this rationale, we deconvolved the two spectral contributions in all MCD spectra and evaluated their relative areas. As expected, we found a trend of the ratio described above which follows closely the effective Zn-content found from ICP (inset of Figure 3.15). This result indicates that, independently of the validity of the initial assumption, the Zn^{2+} ions occupy T_d sites, since their position in O_h sites, replacing Fe^{3+} and Co^{2+}, should lead to a decrease of the transition at 2.2 eV with respect to 1.7 eV one.

3.3 Applications: hyperthermic and relaxometric efficiencies

As discussed previously, colloidal suspensions of MNPs can act as contrast agent for MRI and convert the energy of an alternating magnetic field, of appropriate intensity and frequency, into heat (ν of 50-500 kHz, H_0 up to 15 kAm^{-1}, maintaining the $H_0\nu$ product below the tolerance threshold of 5 x 10^9 $Am^{-1}s^{-1}$ to avoid deleterious physiological responses such as skeletal muscles stimulation, cardiac stimulation and arrhythmias [37]). To understand the heat generation mechanisms some basic principles of magnetism must be outlined.

When a material is exposed to a magnetic field H, the magnetic induction, B, of the material can be expressed as $B=\mu_0(H+M)$, where μ_0 is the vacuum permeability ($\mu_0=4\pi\cdot10^{-7}$ Hm^{-1}) and M the magnetization of the material (M=m/V, where m is the magnetic moment and V the volume of the material. Magnetic materials can be classified by susceptibility, $\chi = dM/dH$, or magnetic permeability, $\mu = dB/dH$, which describe the magnetization degree of the material in response to an applied magnetic field. In SI units, χ is adimensional because both M and H are expressed in A/m. Finally, the permeability of a material is related to the magnetic susceptibility by the relationship, $\mu = \mu_0(1 + \chi)$ and the relative permeability (μ_r) is expressed as $\mu_r = \mu/\mu_0$.

3.3.1 Physical mechanisms of the hyperthermic treatment with MNPs

To develop optimized MNPs for hyperthermic treatment, it is important to know the heat generation phenomena associated to magnetic mediators. The involved mechanism depends on the characteristics of the electromagnetic field (frequency and amplitude) as well as on the material properties and size. The capability of superparamagnetic materials to absorb energy from an external alternating magnetic field (AMF) is due to the hysteretic behaviour induced by the lag of the magnetization to follow the external field. Unlike bulk ferro/ferrimagnetic materials, for which the magnetic hysteresis depends on the instantaneous re-orientation of the magnetic domains, single domain MNPs present magnetic irreversibility only if the field variation is faster than the characteristic time of the magnetization reversal. In both cases, however, the energy stored for each field cycle can be quantified by the hysteresis area. In a very general way, thus, the heating efficiency, or SAR, *i.e.*, the energy adsorbed and converted in full into heat per unit of mass, can be defined as follows:

$$SAR = \mu_0 \nu \oint M(H) dH \tag{3.4}$$

where ν is the frequency of the AMF, that is the number of field cycle repetition in the unit of time. The evaluation of the area of the hysteresis is not an easy task, as it depends on the features of the material and can be hardly estimated *a priori*, particularly when minor loops are concerned, as in the case of MFH applications. On the other hand, the experimental measurement of this quantity, if feasible in principle for multidomain

material, becomes impossible for superparamagnetic material, where the hysteresis area extent varies with the field scan speed and thus with the acquisition time. To overcome this problem, some models, that provide values whose approximation mainly depends on the mean size of the MNPs and on the strength of the applied field, H_0, can be adopted. Among the theoretical formulations, the most popular for mono-dispersed MNPs, is the linear response theory (LRT) [1], the main assumption of which is that the magnetization varies linearly with the oscillating magnetic field as:

$$M(t) = \chi \cdot H(t) = H_0(\chi' \cos 2\pi\nu t + \chi'' \sin 2\pi\nu t) \qquad (3.5)$$

where χ' and χ'' represent the in-phase and out-of-phase components of the magnetic susceptibility, respectively, that, intrinsically, depends on the field frequency. This hypothesis is valid when the magnetic anisotropy barrier, KV, and the field oscillation amplitude are small compared to thermal energy, k_BT, *i.e.*,

$$KV/k_BT \ll 1 \qquad (3.6)$$

and

$$\mu_0 \mu H_0/k_BT \ll 1 \qquad (3.7)$$

where K is the anisotropy constant, V and μ are the mean volume and magnetic moment of the MNPs, respectively.

When these conditions are met, the dissipated power is given by the equation:

$$SAR = \frac{\pi \nu \mu_0 H_0^2}{\rho} \cdot \chi'' = \frac{\pi \nu \mu_0^2 H_0^2 M_S^2 V}{3\rho k_B T} \cdot \frac{2\pi \nu \tau_{eff}}{1 + \left(2\pi \nu \tau_{eff}\right)^2} \tag{3.8}$$

where ρ is the density of the material, and τ_{eff} is the effective relaxation time of the magnetization, which, for single domain nanoparticles dispersed in a liquid media (ferrofluid), is:

$$\frac{1}{\tau_{eff}} = \frac{1}{\tau_N} + \frac{1}{\tau_B} \tag{3.9}$$

where

$$\tau_N = \tau_0 e^{\frac{KV}{k_B T}} \tag{3.10}$$

is Néel (or "internal") relaxation time

and

$$\tau_B = \frac{3\eta V_H}{k_B T} \tag{3.11}$$

is the Brown relaxation time, where V_H is the hydrodynamic volume of NPs and η the viscosity of the ferrofluid.

If the reversal of the magnetization takes place following a physical rotation of the NPs inside the fluid, Brown's relaxation occurs. Instead, if the reversal of the magnetization is due to the coherent rotation of all the atomic spins of the NPs through the overcoming of the anisotropy energy

barrier, Néel's relaxation occurs. τ_N is the only mechanism active in samples where NPs are immobilized (e.g. agarose gel at high agarose %) while in a ferrofluid both processes must be considered.

Equation (3.8) allows one to foresee the conditions for SAR maximization, occurring when $2\pi\nu\tau_{eff} = \omega\tau_{eff} = 1$, namely when the relaxation time is equal to the characteristic time of the measurement (in this case the inverse of the applied field frequency, ν). With the aid of equation (3.8), the role of the parameters which mostly influence the heat power dissipation (saturation magnetization, magnetic anisotropy, and mean particle diameter) can be evaluated analytically, as in Figure 3.16, where the typical example of magnetite MNPs are reported. Figure 3. 16a shows that the SAR has a well pronounced, sharp maximum arising from the sum of the contribution of Néel and Brown relaxations. Evaluations of Figure 3.16b and 3.16c demonstrate how the maximum of SAR grows as the magnetization saturation increases and as the magneto-crystalline energy decreases, respectively. Thus, the LRT model provides useful indications to foresee the behaviour of a magnetic nanomaterial under the application of an AFM and thus to tune its main features to optimize the heating process.

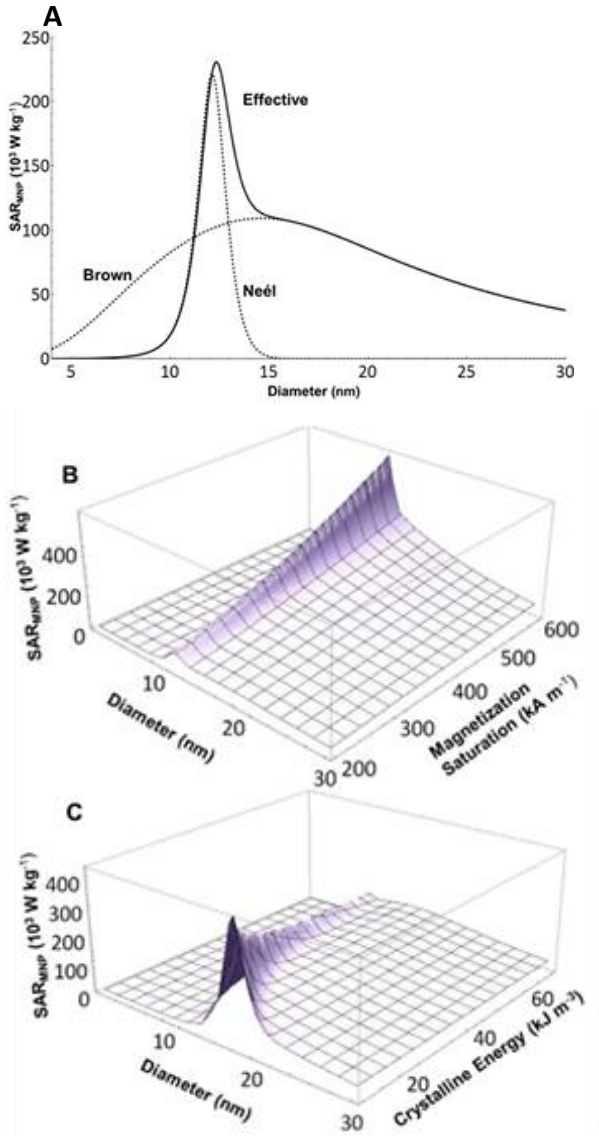

Fig. 3.16. Dependence of SAR for monodisperse magnetite MNPs evaluated from equation 3.8 on A) size ($K = 15\ kJm^{-3}$, $M_S = 450\ kAm^{-1}$), B) magnetization saturation ($K = 15\ kJm^{-3}$), and C) magnetic anisotropy energy ($M_S = 450\ KAm^{-1}$). Calculations were performed for $H_0 = 10 kAm^{-1}$ and $f = 500\ kHz$. Reprinted with permission from Ref. [38].

The hyperthermic efficiency of the materials is usually expressed in term of SAR and can be experimentally determined using a calorimetric method: ferrofluid is placed at the center of an induction coil and the temperature rise during the exposition to an alternate magnetic field is measured. SAR is then expressed as:

$$SAR = \frac{\sum_i Q_i}{m_{Me} t_{irr}} \tag{3.12}$$

where t_{irr} is the irradiation time, m_{Me} the total metal mass and $\sum_i Q_i$ represent the sum of the heat absorbed by the *i-th* specie (MNPs, solvent, surfactant, etc.) with mass m_i and specific heat c_{pi}, $Q_i = m_i c_{pi} \Delta T$. Thus, the above expression becomes:

$$SAR = \frac{\sum_i m_i c_{pi}}{m_{Me}} \frac{\Delta T}{\Delta t} \tag{3.13}$$

If calorimetric measurements are carried out in an adiabatic system, the obtained SAR values are very accurate because, in this way, all the heat generated contributes to the sample temperature increase. In these conditions the temperature rise is linear with time and SAR can be directly obtained as the slope of the T vs. t curve. However, most of the experimental set-up does not work in adiabatic conditions, leading to non-linear temperature increase. In this case, the estimation of SAR is performed considering the slope of the curve in the limit of $t \to 0$ by a linear fit.

3.3.2 Hyperthermic efficiency of $Co_xZn_yFe_{3-(x+y)}O_4$ NPs

To evaluate the hyperthermic efficiency of the synthesized samples, calorimetric measurements of specific absorption rate (SAR) were performed. The set up for the calorimetric measurements was built up at our laboratory and is based on a 6 kW power supply by Fives Celes (Figure 3.17).

Fig. 3.17. Picture of magnetic heating equipment used in this work.

Measurements were carried out by applying for 300 s an alternating magnetic field of 12 kA/m amplitude and 183 kHz frequency on a suspension in toluene (1.6 - 1.9 % w/w) in the presence of 7.5 mM of oleic acid and 7.5 mM of oleylamine. The temperature of the sample was recorded using an optical fiber temperature probe (Optocon-Fotemp). Samples were surrounded by polystyrene and hosted in an ethylene glycol

based thermostated glass dewar, in order to thermally isolate the sample from the surroundings and SAR values were evaluated using the equation (3.13). Since the measurements are carried in non-adiabatic conditions, $\Delta T/\Delta t$ values were extrapolated for t→ 0 by considering the initial slope of the temperature kinetic curves. The temperature kinetics curves of the $Co_xZn_yFe_{(3-x-y)}O_4$ series upon exposure to an alternating magnetic field are reported in Figure 3.18.

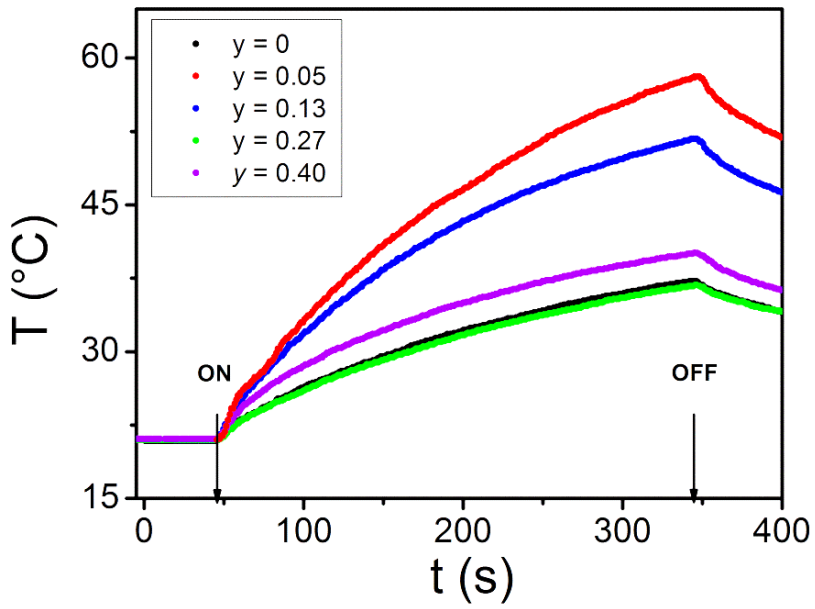

Fig. 3.18. Temperature kinetic curves of $Co_xZn_yFe_{(3-x-y)}O_4$ NPs, acquired during the exposition for 300 s to an alternate magnetic field (H = 12 kA/m, 183 kHz). Arrows denotes the switching on/off of the external alternating field.

This peculiar trend of SAR can be explained only partially considering M_S, because although the M_S dependence on Zn-content is similar, its variation is very small (Figure 3.19). On the other hand, also K alone cannot be directly related to the SAR, as it exhibits a different trend (Figure 3.12). The magnetic behavior at field amplitudes comparable with that employed in the calorimetric measurement (H = 12 kA/m) can be useful to get information on the heating process. In Figure 3.20 the minor loops measured at room temperature are shown. Notwithstanding the minor loops are measured on a much longer time scale with respect to the hyperthermic experiments, the values of the loop area multiplied by the experimental frequency (183 kHz) can be taken as a qualitative estimation of the power losses contribution (SAR_{hl}) [39].

The comparison of Figure 3.19 shows how SAR_{hl} reflects the experimental SAR trend upon Zn-content, particularly for the smallest y-value where the samples are clearly blocked (CoZnFe05 and CoZnFe13). For higher Zn substitution, the minor loop area is no more a significant indicator of the heating capability of the samples, since, coherently with the T_B findings (see Table 3.4), these samples are close to the superparamagnetic regime at room temperature. In this case, however, the heating mechanism is well described by the Rosenweig model, which is based on the linear response approximation, i.e $M \approx \chi H$ [1], and thus the magnetic susceptibility, χ, becomes the key parameter to assess the hyperthermic efficiency. The higher value of χ of CoZnFe40 justifies therefore the relative raise of its SAR compared to the other samples of the series.

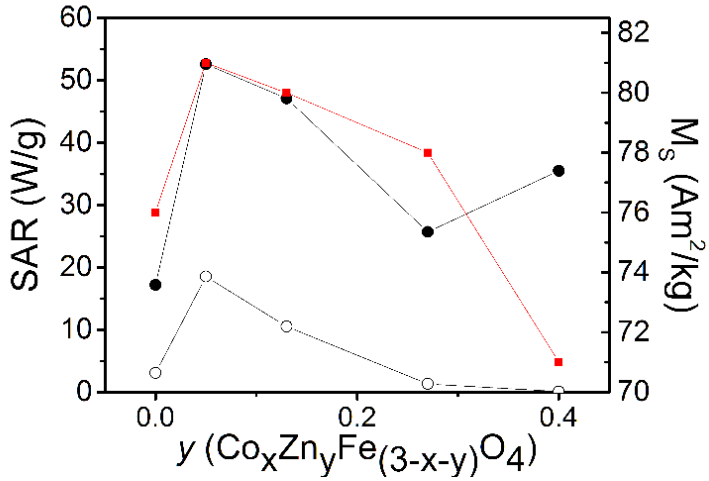

Fig. 3.19. *SAR* values of $Co_xZn_yFe_{(3-x-y)}O_4$ NPs as a function of Zn-content *y* experimentally measured (full black circles) and evaluated by the minor loop area multiplied by the operating frequency, SAR_{hl} (empty black circles); the M_S values (full red squares) are reported for comparison.

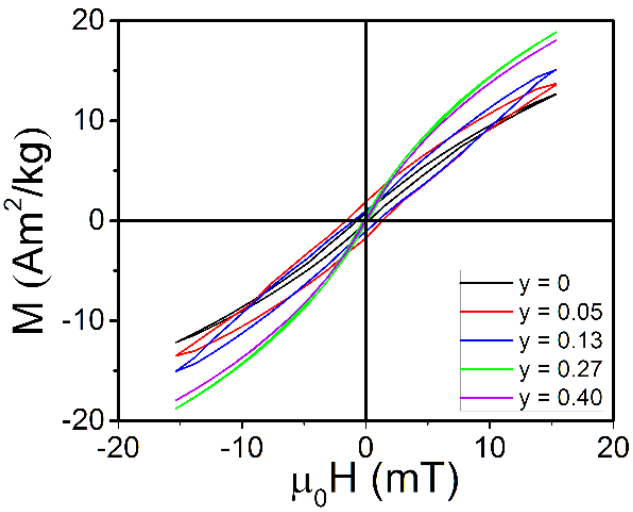

Fig. 3.20. Minor loop recorded at 300K with H_{max} = 12 kA/m ($\mu_0 H_{max}$ = 15.3 mT).

In the previous discussion, we evidenced how a small amount of Zn can improve the hyperthermia capability of cobalt ferrite NPs. However, the SAR value achieved is not very high, if compared to the literature data reported for ferrite NPs specifically synthesized for this application. Nevertheless, a further increase of SAR of Cobalt Zinc ferrite can be easily obtained by an even small increase of the mean size of the NPs. To support this claim, a series of NPs with 9 nm mean diameter containing the same amount of Zn and Co were synthesized. In particular, 3 samples were prepared with Zinc content y = 0.05, 0.11 and 0.26, respectively. The main morphological and magnetic characterization data are reported in Tables 3.7 and 3.8. TEM images are shown in Figure 3.21, together with the NPs size distributions, fitted to a log-normal function. All samples are composed of almost spherical NPs of *ca.* 9 nm diameter. Mean and standard deviation values are statistically evaluated from the size histograms. As for smaller NPs series, the lattice parameter increases with Zn-content confirming that the Zn^{2+} ions are effectively incorporated in T_d sites of the ferrite lattice. Moreover, the good agreement between the average NPs diameter obtained from TEM and the crystal grain size from XRD measurements suggests that all samples are composed by highly ordered, single crystal NPs. The analysis of the magnetic behavior (M_S, H_C, etc..) shows it resembles that of the 8 nm series. The expected increase of M_S with progressively increasing Zn substitution is preserved only at 5 K, whereas at room temperature, this effect is partially nullified by the weakening of the magnetic exchange coupling constants between T_d and O_h sites due to the increasing Zn substitution. Moreover, the spinel lattice modifications (expansion and local crystal distortion), induced by the progressive introduction of Zn^{2+} ions, are responsible of a strong decrease of the magnetic anisotropy of the material. In fact, as for 8 nm series, the

decrease of H_C from 0.98 to 0.55 and M_R from 0.78 to 0.65 (measured at 5 K) denotes how the cubic symmetry of pure cobalt ferrite evolves toward uniaxial one without reaching it completely. The SAR value for the sample with the smallest amount of zinc (y = 0.05) reaches 103 W/g. Thus, this sample, with a large heat capability, is a very promising candidate for clinical application in MFH. Furthermore, it is worth to stress that the SAR decrease upon further increase of Zn-content (y = 0.26), is confirmed for the 9 nm series (Figure 3.22).

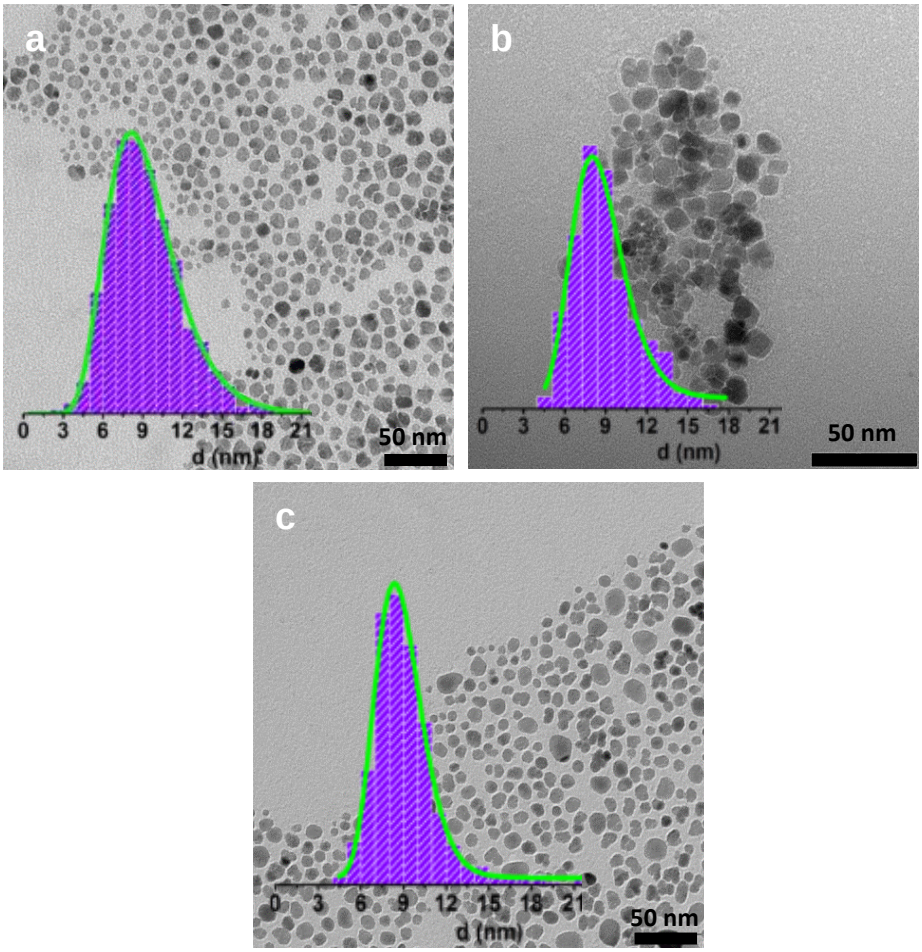

Fig. 3.21. TEM images of $Co_xZn_yFe_{(3-x-y)}O_4$ NPs of 9 nm a) CoFe05_9, b) CoZnFe11_9 and c) CoZnFe26_9. In the insets, the corresponding diameter distribution evaluated over 700-750 NPs is reported. The continuous line represents the best fit curve to a lognormal distribution.

Sample	d_{TEM} (nm)	d_{XRD} (nm)	a (Å)	x	y	z
CoZnFe05_9	9.2 ±2.7	11.0 (6)	8.404(1)	0.46	0.05	2.46
CoZnFe11_9	9.0 ± 2.3	9.6 (5)	8.415(1)	0.55	0.11	2.30
CoZnFe26_9	9.2 ±2.4	10.1 (5)	8.410(2)	0.52	0.26	2.22

Tab. 3.7. Chemical and structural properties of 9 nm $Co_xZn_yFe_{(3-x-y)}O_4$ NPs. d_{TEM}: NPs average diameter and standard deviation obtained from TEM analysis; d_{XRD}, a: crystallite mean size and lattice parameter obtained from XRD data analysis (errors on the least significant digit are reported in brackets); x, y, z: Co, Zn and Fe content obtained from ICP analysis.

Sample	μ_{tot}	T_B (K)	M_{5T} 5 K (Am^2/kg)	M_{5T} 300 K (Am^2/kg)	$\mu_0 H_C$ 5 K (T)	M_R 5 K	M_S calc. (Am^2/kg)	SAR (W/g_{Me})
CoZnFe05_9	3.84	>310	93	79	0.98	0.78	91.9	103.3 ± 1.3
CoZnFe11_9	4.11	>310	91	74	0.93	0.75	98.0	100.3 ± 1.8
CoZnFe26_9	5.04	~285	103	82	0.55	0.65	119.5	59.8 ± 2.0

Tab. 3.8. Magnetic and hyperthermic parameters of 9 nm $Co_xZn_yFe_{(3-x-y)}O_4$ NPs. μ_{tot}: average magnetic moment in μ_B units for chemical formula unit; T_B: blocking temperature; M_{5T}: experimental magnetization measured at 5T; H_C: coercive field; M_R: reduced remnant magnetization; M_S calc.: theoretical value of saturation magnetization calculated as described for 8 nm samples; SAR: SAR values per gram of metal (Co+Zn+Fe) obtained by applying an alternating magnetic field of 12 kA/m and 183 kHz.

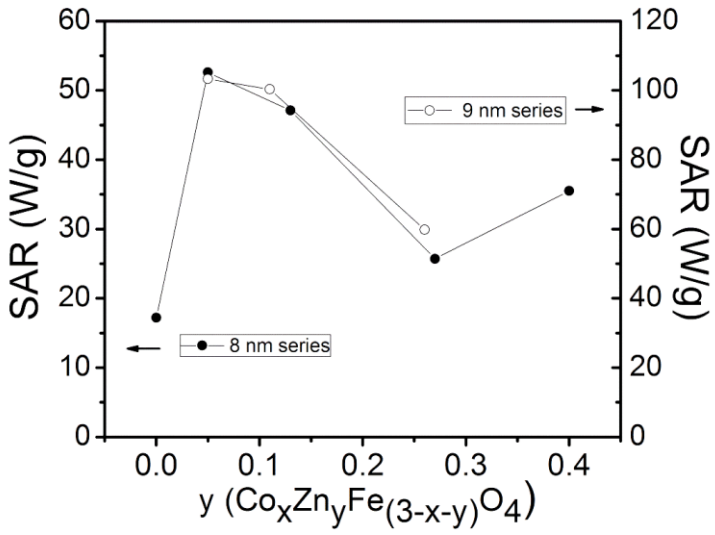

Fig. 3.22. Comparison of experimental SAR values of CoZnFeyy and CoZnFeyy_9 samples obtained at 183 kHz and 12 kA/m.

3.3.3 Relaxometric efficiency of $Co_xZn_yFe_{3-(x+y)}O_4$ NPs

In addition to the heating properties we checked the efficacy of the material to act as contrast agent for MRI. Water suspensions for relaxometric measurements were obtained by transferring NPs from organic to aqueous solution by ligand-exchange with tetrametylammonium hydroxide (see experimental section for synthetic details). The nuclear longitudinal relaxivity was evaluated as $r_1 = (1/T_{1,meas} - 1/T_{1,matrix})/C$, where $T_{1,meas}$ is the measured nuclear relaxation time, $T_{1,matrix}$ is the nuclear relaxation time of water and C is the magnetic ion concentration. The NMR-D r_1 profiles, reported in Figure 3.23, clearly display a scaling behavior as a function of the Zn-content. The evolution of the shape of the curve follows the trend of the magnetic anisotropy

previously discussed. The r_1 NMR-D profile of CoZnFe40 is characterized by a low frequency plateau, a maximum at $v \sim 1.5$ MHz, and a drop of the relaxation rate for higher frequencies. These are typical features of superparamagnetic NPs [40]. On the contrary, the r_1 curve of CoFe00 displays a plateau at low frequencies and a drop of r_1 for $v > 2$ MHz. This shape is associated to high magnetic anisotropy [41]. Furthermore, an enhancement of the r_1 values over the whole frequency range is observed when the amount of zinc increases. Using the model by Roch *et al.* [7] to fit the r_1 data, M_S values in good agreement with those obtained by D.C. susceptibility measurements are estimated and the obtained data are reported in Table 3.8.

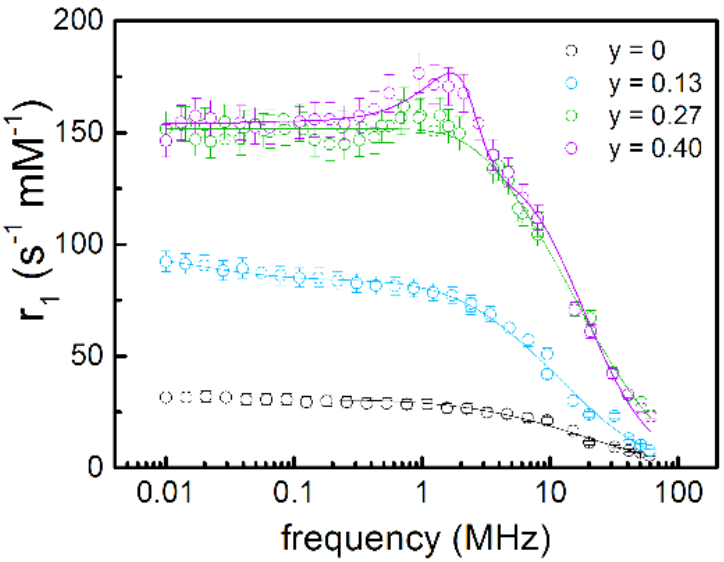

Fig. 3.23. Longitudinal relaxivity profiles and best fit curves.

Sample	τ_N(s)	r_d(nm)	M (Am^2/kg)
CoFe00	3.2 (2.4) x 10^{-7}	5.6 (0.2)	76
CoZnFe13	2.3 (0.9) x 10^{-7}	7.9 (0.3)	80
CoZnFe27	7.8 (1.1) x 10^{-8}	6.6 (0.1)	78
CoZnFe40	2.37 (1.8) x 10^{-8}	9.4 (0.3)	80

Tab. 3.8. Best fit parameters obtained by fitting the r_1 profiles with the Roch model for nuclear relaxation**.** τ_N*:* Néel relaxation time; r_d: minimum approach distance; *M*: specific magnetization.

The nuclear transverse relaxivities r_2 measured at 1.41, 0.36 and 0.17 T (60, 15.5 and 7.2 MHz for 1H, respectively) are shown as a function of the Zn-content in Figure 3.24. These measurements allowed the investigation of the contrast efficiency of the cobalt zinc ferrite NPs at the typical field used in clinical MRI scanners (e.g., 1.5 T): in particular, the higher the r_2, the higher the contrast efficiency. All the samples proved to be good contrast agents, displaying a transverse relaxivity at least comparable to the commercial superparamagnetic compounds (Endorem is here taken as reference compound). Furthermore, the r_2 value is proportional to the Zn amount, being the highest ($r_2 \sim 515$ s^{-1}mM^{-1}) for y=0.4. The influence of the single particle magnetization is crucial for the nuclear spin-spin relaxation of the superparamagnetic NPs since $r_2 \propto M^2$ [7, 8]. Thus, the r_2 increasing trend found as a function of Zn amount, whereas the M is substantially constant, suggests that some physical mechanisms behind the transverse relaxation are still unclear [42].

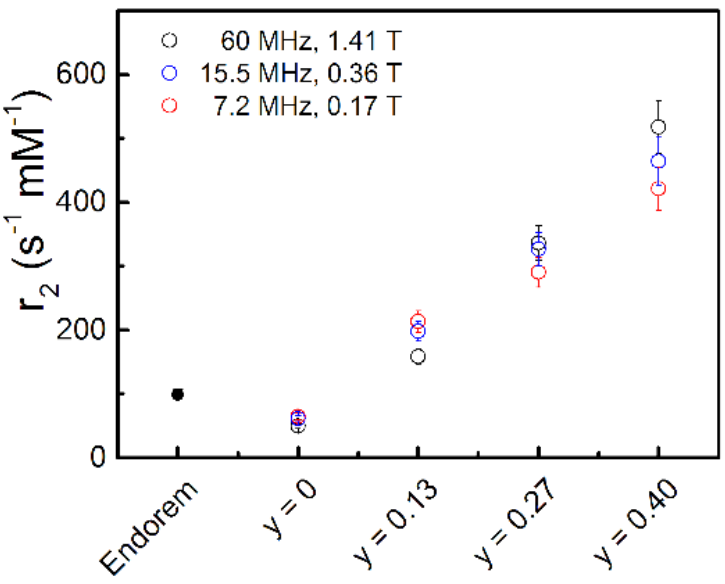

Fig. 3.24. Transverse relaxivities values measured at 7.2, 15.5 and 60 MHz and plotted as a function of the Zn amount. A former commercial compound (Endorem) is here used as reference (data acquired at 1.41 T).

3.4 Conclusions

A series of Zn-substituted cobalt ferrite NPs with comparable average diameter and variable amount of Zn^{2+} ions was synthesized by thermal decomposition and their structural and magnetic properties were deeply characterized by a wealth of techniques. Since cobalt ions have a strong impact on the magnetic properties of this material, its content was kept constant at approximately x=0.6. This strategy, which to our knowledge has not been explored so far, allowed us to elucidate the effect of Zn substitution on the physical behavior of this complex nanomaterial. The analysis of the magnetic behavior of the series demonstrated that the expected increase of magnetic moment with progressive Zn substitution, due to the unbalance between T_d and O_h spin sublattices, is preserved only at low temperature. On the contrary, on increasing temperature the thermal disorder decreases the spin alignment degree, and, at room temperature the increase of M_S is retained only for very small amounts of Zn. Moreover, this effect is further counterbalanced by the strong reduction of magnetic anisotropy produced by the insertion of Zn^{2+} ions in the spinel lattice, as indeed demonstrated by magnetic, XMCD and magneto-optical measurements. This behavior can be ascribed to the lattice expansion and local crystal distortion, as well as to the modification in cation distribution following the substitution. These results redefine the expectations relying on Zn-substitution as an effective strategy to improve the performances of cobalt ferrite NPs, particularly in view of their exploitation in biomedical applications. In fact, to assess the impact of these modifications on this landscape, we performed explorative experiments to evaluate the efficiency of the series in the two staple theranostic methodologies, i.e., magnetic fluid hyperthermia and NMR relaxivity. If on one hand the

obtained results show that increasing the Zn-content raises the capability of NPs of contrasting MR images, on the other, we found that a value of y between 0.05 and 0.15 increases the hyperthermic efficiency of cobalt ferrite NPs but that any further increase of Zn concentration leads to an opposite effect.

References

[1] R. E. Rosensweig, *J. Magn. Magn. Mater.*, **2002**, 252, 370.

[2] J.-P. Fortin, C. Wilhelm, J. Servais, C. Ménager, J.-C. Bacri, F. Gazeau, *J. Am. Chem. Soc*. **2007**, 129, 2628.

[3] L. Lartigue, C. Innocenti, T. Kalaivani, A. Awwad, Mdel. M. Sanchez Duque, Y. Guari, J. Larionova, C. Guérin, J.-L. G. Montero, V. Barragan-Montero, P. Arosio, A. Lascialfari, D. Gatteschi, C. Sangregorio *J. Am. Chem. Soc.* **2011**, 133, 10459.

[4] S. Purushotham, R. V. Ramanujan *J. Appl. Phys.* **2010**, 107, 114701.

[5] C. Ravagli, *Synthesis and characterization of nanosized magnetic materials for hypertermia applications*, Ph. D. Thesis, University of Florence, **2009**.

[6] C. C. Berry, *J. Phys. D: Appl. Phys.* **2009**, 42, 22.

[7] A. Roch, R. N. Muller, P. Gillis, *J. Chem. Phys.* **1999**, 110, 5403.

[8] Q. L. Vuong, J. -F. Berret, J. Fresnais, Y. Gossuin, O. Sandre, *Adv. Healthc. Mater.* **2012**, 1, 502.

[9] E. Fantechi, G. Campo, D, Carta, A. Corrias, C. de Julián Fernández, D. Gatteschi, C. Innocenti, F. Pineider, F. Rugi, and C. Sangregorio, *J. Phys. Chem. C*, **2012**, 116, 826.

[10] E. Fantechi, C. Innocenti, M. Albino, E. Lottini, and C. Sangregorio, *J. Magn. Magn. Mater.*, **2015**, 380, 365.

[11] A. Sathya, P. Guardia, R. Brescia, N. Silvestri, G. Pugliese, S. Nitti, L. Manna, T. Pellegrino, *Chem. Mater*. **2016**, 28, 1769.

[12] J. Jang, H. Nah, J.-H. Lee, S. H. Moon, M. G. Kim, J. Cheon, *Angew. Chem. Int. Ed. Engl.* **2009**, 48, 1234.

[13] R. A. Bohara, N. D. Thorat, A. K. Chaurasia, S. H. Pawar, *RSC Adv.* **2015**, 5, 47225.

[14] G. Petitt, D. Forester, *Phys. Rev. B* **1971**, 4, 3912.

[15] Q. Lin, J. Xu, F. Yang, J. Lin, H. Yang, Y. He, *Materials* **2018**, 11, 1799.

[16] J. Smit, H. P. J. Wijn, N. V. Philips, *Ferrites*, Gloeilampenfabrieken **1959**.

[17] V. Mameli, A. Musinu, A. Ardu, G. Ennas, D. Peddis, D. Niznansky, C. Sangregorio, C. Innocenti, N. T. K. Thanh, C. Cannas, *Nanoscale* **2016,** 8**,** 10124.

[18] A. W. Orbaek, L. Morrow, S. J. Maguire-Boyle, A. R. Barron, *J. Exp. Nanoscience* **2013**, 10, 324.

[19] S. S. Jadhav, S. E. Shirsath, S. M. Patange, K. M. Jadhav, *J. Appl. Phys.* **2010**, 108, 093920.

[20] H. S. C. O'Neill, A. Navrotsky, *Am. Mineral.* **1983**, 68, 181.

[21] J. F. Hochepied, P. Bonville, M. P. Pileni, *J. Phys. Chem. B* **2000**, 104, 905.

[22] P. Coppola, F. G. da Silva, G. Gomide, F. L. O. Paula, A. F. C. Campos, R. Perzynski, C. Kern, J. Depeyrot, R. Aquino, *J. Nanopart. Res.* **2016**, 18, 138.

[23] K. Raju, G. Venkataiah, D. H. Yoon, *Ceram. Int.* **2014**, 40, 9337.

[24] Y. Yafet, C. Kittel, *Phys. Rev.* **1952**, 87, 290.

[25] J. M. D. Coey, *Magnetism and Magnetic Materials*, Cambridge University Press **2010**.

[26] S. Cojocaru, A. Naddeo, R. Citro, *EPL* **2014**, 106, 17001.

[27] M. M. Schieber, *Iron Oxides and Their Compounds* in *Experimental Magnetochemistry*, E. P. Wohlfarth Ed **1967**, p 182.

[28] J. L. Dormann, D. Fiorani, E. Tronc, *Adv. Chem. Phys.* **1997**, XCVIII, pp. 283-494.

[29] N. A. Usov, S. E. Peschany, *J. Magn. Magn. Mater.* **1997**, 174, 247.

[30] J. F. Hochepied, P. Sainctavit, M. P. Pileni, *J. Magn. Magn. Mater.* **2001**, 231, 315.

[31] R. Skomski, A. Kashyap, A. Enders, *J. Appl. Phys.* **2011**, 109, 07E143.

[32] R. Topkaya, A. Baykal, A. Demir, *J. Nanoparticle Res.* **2012**, 15, 1359.

[33] E. Tirosh, G. Shemer, G. Markovich, *Chem. Mater.* **2006**, 18, 465.

[34] G. Campo, F. Pineider, V. Bonanni, M. Albino, A. Caneschi, C. De Julián Fernández, C. Innocenti, C. Sangregorio, *Chem. Mater.* **2015**, 27, 466.

[35] W. R. Mason, *A Practical Guide to Magnetic Circular Dichroism Spectroscopy*, Wiley-Interscience **2007**.

[36] K. J. Kim, H. S. Lee, M.H. Lee, S. H. Lee, S. H. *J. Appl. Phys.* **2002**, 91, 9974.

[37] Q. A. Pankhurst, J. Connolly, S. K. Jones, J. Dobson, *J. Phys. D: Appl. Phys.* **2003**, 36, 167.

[38] A. Cervadoro, C. Giverso, R. Pande, S. Sarangi, L. Preziosi, J. Wosik, A. Brazdeikis, P. Decuzzi, *PLoS One* **2013**, 8, e57332.

[39] G. T. Landi, *J. Magn. Magn. Mater.* **2012**, 324, 466.

[40] Y. Gossuin, P. Gillis, A. Hocq, Q. L. Vuong, A. Roch, A. *Wiley Interdiscip. Rev. Nanomed. Nanobiotechnol.* **2009**, 1, 299.

[41] T. Orlando, M. Albino, F. Orsini, C. Innocenti, M. Basini, P. Arosio, C. Sangregorio, M. Corti, A. Lascialfari, *J. Appl. Phys.* **2016**, 119, 134301.

[42] Y. Gossuin, T. Orlando, M. Basini, D. Henrard, A. Lascialfari, C. Mattea, S. Stapf, Q. L. Vuong, *Nanotechnology* **2016**, 27, 155706.

Chapter 4

Ferrite based MNPs for technological applications

This chapter will be focused on the development of a synthetic route, suitable for industrial scale-up, to prepare $Mn_xZn_yFe_zO_4$ (x+y+z=3) MNPs with variable composition and with magnetic properties optimized for application in two different fields. On one hand we tried to prepare low power loss powder to be integrated in electronic devices operating at high frequency, i.e. in the 2-5 MHz range. On the other hand, we aimed at fabricating soft building blocks to realize exchange coupled rare-earth free permanent magnet with high $(BH)_{max}$, by coupling the soft particles with a hard magnetic material ($SrFe_{12}O_{19}$).

Concerning high frequency electronic applications, the work addressed the maximization of the M_S and the magnetic permeability of the final product, while reducing power losses in the 2-5 MHz frequency range. With regards to the permanent magnet research area, the work focused on the synthesis of a soft magnetic material with a high M_S value in order to increase the remanence of the final product (Figure 1.6). As discussed more extensively in the introduction, the two objectives are partially overlapped. The improvement of the magnetic properties of the material in the two applications requires, indeed, the maximization of the magnetic permeability in one hand, and of the remanence in the other, conditions which can be both satisfied by a soft magnetic material with a high M_S value. Therefore, in the following the two approaches will be discussed in

the same Chapter.

From the perspective of the large-scale production, $Mn_xZn_yFe_zO_4$ (x+y+z=3) NPs were synthesized by co-precipitation starting from aqueous solution of manganese, zinc, iron (II) and iron (III) chlorides. This synthetic method was chosen because, even if it does not allow for obtaining MNPs with high size and shape uniformity, and crystallinity, it is facile, cheap, eco-sustainable (aqueous synthesis), it provides large quantities of materials (grams) and it is easily scalable (up to kilograms). The, the as obtained MNPs underwent a thermal annealing treatment to enhance the magnetic properties of interest.

The synthesized $Mn_xZn_yFe_zO_4$ (x+y+z=3) NPs were characterized by TEM, SEM, XRD and ICP-AES, to investigate size, morphology and size distribution, crystallographic phase and the effective stoichiometry, respectively. To evaluate the main magnetic properties (M_S, H_C and M_R), measurements were performed using a SQUID magnetometer. This detailed characterization allowed us to rationalize the effect of the Mn and Zn substitution on the magnetic properties of spinel ferrite NPs and to identify the stoichiometry and the thermal treatment conditions to maximize the M_S of the final product.

4.1 Ferrite based MNPs for electronic applications

Micrometric ferrites find a large use in the production of electric devices as inductors (electric components that store energy in a magnetic field when crossed by an electric current) and transformers (electric components which transfer electrical energy between two or more circuits, through electromagnetic induction). They consist of a conductive material, generally copper wire, wound on a core of material with high magnetic

permeability (ferrites or other soft magnetic materials). These devices have the capability to convert electric energy in magnetic energy and the opposite and are subjected to magnetization and demagnetization cycles during their use. Thus, to maximize the efficiency of the conversion process, the dissipation of the magnetic energy, quantified by the area of the hysteresis loop during each cycle, into heat should be minimum [1, 2]. Nowadays, magnetic cores for traditional electronic applications in 1-2 MHz frequency range are obtained with standard methods, usually starting from micrometric ferrites obtained by ball-milling of bulk materials and then sintered in the desired shapes. Inductors and transformers containing magnetic cores based on micrometric spinel ferrite doped with manganese and zinc are particularly suited for operating in the range 1-2 MHz, but for higher frequencies (2-5 MHz) exhibit extraordinary increased power losses. This may represent a crucial limitation in the next future as the quest for continuously increasing performances and smaller size of electronic devices is pushing towards the use of increasing frequencies (at least 4 MHz). On the other side, magnetic cores used for application in the frequency range of GHz, such as micrometric spinel ferrite doped with nickel and zinc, also exhibit high power losses in the MHz range, mostly due to their low relative permeability. In fact, magnetic cores based on Ni-Zn ferrites are characterized by a lower permeability compared to that of Mn-Zn ferrites, which remains constant for a large range of frequencies, making this material competitive only for application in the GHz range. .In this context, we focused our attention on the development of a synthetic route, suitable for industrial scale-up, to prepare Mn-Zn ferrites, with high M_S and magnetic permeability and reduced power losses for extending its application in the next future to the 2-5 MHz range. The work was carried out in collaboration with Vicor Corporation (Andover, Massachusetts,

United States), a company leader in the electronics sector, which is strongly interested on the application of this material in high frequency devices. Since I signed a *non-disclosure agreement* (*nda*) with Vicor Corporation, the results presented here have been agreed with them. The parts snipped for industrial convenience, however, do not affect the significance and presentation of the research.

4.1.1 Synthesis and structural and magnetic characterization of $Mn_xZn_yFe_zO_4$ NPs

$Mn_xZn_yFe_zO_4$ (x+y+z=3) NPs with variable composition were synthesized by co-precipitation starting from aqueous solution of manganese, zinc, iron (II) and iron (III) chlorides. The molar ratio of metal transition chlorides was quantitatively adjusted according to the final desired stoichiometry. The reactions were carried out in basic aqueous solution (NaOH) at 100 °C, under inert atmosphere (N_2) obtaining ca. 5 g of nanometric powder (see experimental section for synthetic details). The reaction consists in the precipitation of transition metal hydroxides after the addition of sodium hydroxide and the following dehydration:

$$xMn^{2+} + yZn^{2+} + zFe^{2+} + 2Fe^{3+} + nOH^- \rightarrow$$
$$xMn(OH)_2 + yZn(OH)_2 + zFe(OH)_2 + 2Fe(OH)_3 \xrightarrow{\Delta}$$
$$Mn_xZn_yFe_zFe_2(OH)_{(8-2n)}O_n \xrightarrow{\Delta} Mn_xZn_yFe_zO_4$$

The last process is driven by the increase of temperature up to 100 °C and consists in a transformation of the hydroxides first in mixed oxo-hydroxides and then in the desired cubic spinel structure. It should be

noted that precipitation of the metal hydroxides is mainly driven by the pH values of the solution. Indeed, this process occurs at different pH depending on the transition metal (Figures 4.1 - 4.4). On this basis, in order to quantitatively precipitate $Fe(OH)_3$, $Fe(OH)_2$, $Mn(OH)_2$ and $Zn(OH)_2$, it is appropriate to work with a pH value close to 8, 12, 10-12, and 9-11, respectively. Therefore, to obtain simultaneous co-precipitation of the metal hydroxides, the pH value was set in the 10-11 range. Moreover, manganese and ferrous ions have a high instability towards oxidation in water, thus, to avoid the oxidation of Mn^{2+} to Mn^{4+} and of Fe^{2+} to Fe^{3+}, which would prevent the formation of the spinel structure, the reaction was carried out under inert atmosphere (nitrogen flow) and using N_2 purged demineralized water.

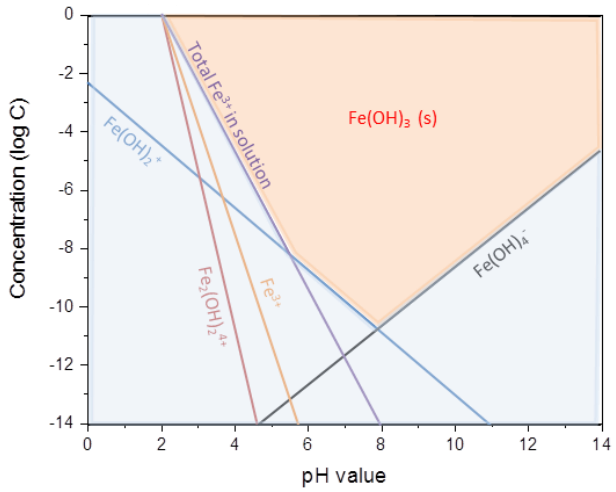

Fig. 4.1. Aqueous-solid phase equilibrium for iron (III) hydroxide complexes as a function of pH. The light red region indicates the region at which the solid exists; conversely, the light blue areas indicate the water-soluble regions.

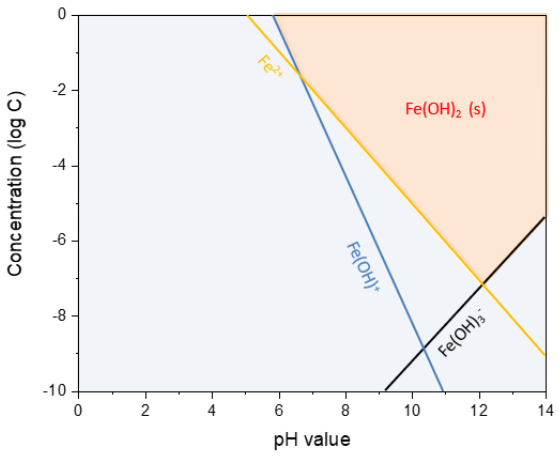

Fig. 4.2. Aqueous-solid phase equilibrium for iron (II) hydroxide complexes as a function of pH. The light red region indicates the region at which the solid exists; conversely, the light blue areas indicate the water-soluble regions.

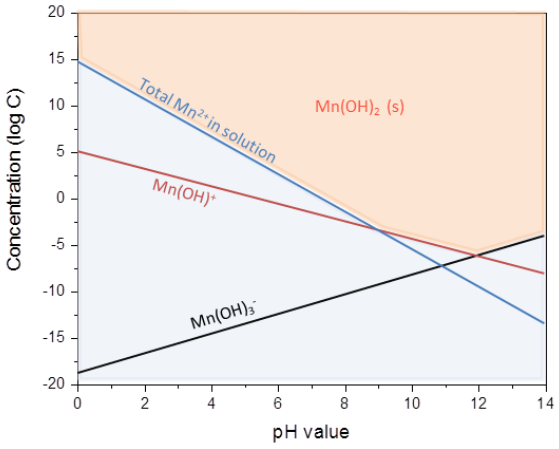

Fig. 4.3. Aqueous-solid phase equilibrium for manganese hydroxide complexes as a function of pH. The light red region indicates the region at which the solid exists; conversely, the light blue areas indicate the water-soluble regions.

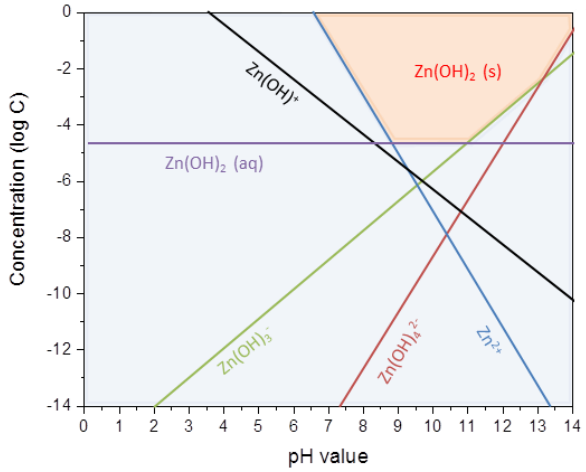

Fig. 4.4. Aqueous-solid phase equilibrium for zinc hydroxide complexes as a function of pH. The light red region indicates the region at which the solid exists; conversely, the light blue areas indicate the water- soluble regions.

As mentioned in the previous paragraphs, Mn-Zn ferrites are widely used in electronic applications in the 1-2 MHz range, due to their high M_S and magnetic permeability. In fact, as reported in Ref. [3] Mn ferrite has the highest relative initial permeability (μ_r) at room temperature (Table 4.1) among bulk ferrites. Moreover, a strong enhancement of M_S has been reported after the introduction of Zn^{2+} in magnetite or manganese ferrite [4, 5] due to cation rearrangement in the spinel lattice. As already discussed in chapter 3 for $Co_xZn_yFe_{1-(x+y)}Fe_2O_4$ NPs, indeed, a gradual increase of M_S is expected with the progressive introduction of diamagnetic Zn^{2+} ions, because, as they tend to occupy tetrahedral (T_d) sites, the antiferromagnetic coupling between Fe^{3+} in T_d and octahedral (O_h) sites is partially removed, making the sublattices more unbalanced.

Ferrites	μ_r 300K	M_S 300 K (Am^2/kg)	M_S 0 K (Am^2/kg)
$MnFe_2O_4$	260.0	80	112
$FeFe_2O_4$	100.0	92	98
$CuFe_2O_4$	45.0	25	30
$NiFe_2O_4$	25.0	50	56
$MgFe_2O_4$	12.0	27	31
$CoFe_2O_4$	1.3	80	90

Tab. 4.1. μ_r and M_S values at room temperature and M_S values at 0 K for some common ferrites. Values taken from Ref. [3, 5]. No measuring frequency was indicated in the references.

In fact, considering as a first approximation a complete inverted spinel structure with all the Mn^{2+} (5 μ_B) ions and Fe^{2+} ions (4 μ_B) located in the octahedral sites, Fe^{3+} ions split between O_h and T_d cavities and assuming all Zn^{2+} ions occupy T_d cavities, the magnetic moment at 0 K for Mn-Zn ferrites, estimated using the same model proposed in Figure 3.8, will be equal to:

$$\mu = 5\,(1+y) + 5x + 4\,(1-x-y) - 5\,(1-y) = (4+x+6y)\mu_B \qquad (4.1)$$

However, this mechanism holds up until the Zn^{2+} substitution reaches *ca*. half of the total number of divalent ions [5]. For a higher percentage, M_S starts decreasing, due to the weakening of the magnetic exchange between

T_d and O_h sites, which induces the destabilization of the ferrimagnetic order and the local canting of the spins in the O_h sites [6 - 8]. Therefore, the work was focused to investigate $Mn_xZn_yFe_zO_4$ (x+y+z=3) NPs with variable composition with $y \leq 0.5$, for exploiting the combined effect of increasing μ_r by introducing Mn^{2+} and M_S by Zn^{2+} substitution to produce a soft magnetic material with reduced power losses.

It should be noted that the previous argument is valid regardless of the fact that actually Manganese ferrite has an only partial inverted character. Bulk MnZn ferrite has indeed an inversion degree of ca. 0.7, while a survey of the literature indicates that different values characterizes nanosized manganese ferrite, from 0.58 for manganese ferrites synthesised by pulsed-laser ablation [9] to 0.58 - 0.67 for MNPs prepared by wet chemical methods [10], and 0.92 for manganese ferrite synthesised through thermal decomposition of oxalates [11].

As a first step, we focussed on sample $Mn_{0.6}Zn_{0.4}Fe_2O_4$, the structural and magnetic characterization of which are reported in the following (Figures 4.5 - 4.7). This Mn-Zn content was chosen to maximize the M_S value since, according to the literature, corresponds to the highest value [4, 5]. For $Mn_{0.6}Zn_{0.4}Fe_2O_4$, the theoretical $M_S = \mu_n \mu_B N_A/PM$, where $\mu_n = 7\ \mu_B$ is the magnetic moment in Bohr magnetons ($\mu_B = 9.274 \cdot 10^{-24}$ J/T) given by equation 4.1 for x = 0.6 and y 0.4, N_A the Avogadro number ($6.022 \cdot 10^{23}$) and PM the molecular weight of $Mn_{0.6}Zn_{0.4}Fe_2O_4$ ferrite, is 166 Am^2/kg. However, according to Ref. [5] and as already discussed for $Co_xZn_yFe_{1-(x+y)}Fe_2O_4$, this M_S value is expected only at very low temperature. In fact, on increasing temperature the thermal disorder decreases the spin alignment degree, and, at room temperature the progressive introduction of the diamagnetic Zn^{2+} in the T_d sites causes a high weakening of the exchange interaction between the O_h and T_d sublattices, leading to a

canting of the spins in the O_h sites with a consequent reduction of M_S [6, 7]. At the nanoscale, as the increase of spin disorder becomes particularly relevant, it is more difficult to make theoretical considerations so that the best composition which maximizes M_S could be different from $Mn_{0.6}Zn_{0.4}Fe_2O_4$.

The effective stoichiometry of the $Mn_{0.6}Zn_{0.4}Fe_2O_4$ powders prepared following the procedure described above was checked by elemental analysis (ICP-AES), and confirmed that the amount of Mn, Zn and Fe introduced into the spinel lattice was, within the experimental error, almost identical to that set in the synthesis (Table 4.2).

A representative TEM image of the sample is shown in Figure 4.5, together with the NPs size distributions, fitted to a log-normal function. The sample consists of monodispersed NPs of 7 ± 2 nm diameter with irregular shape.

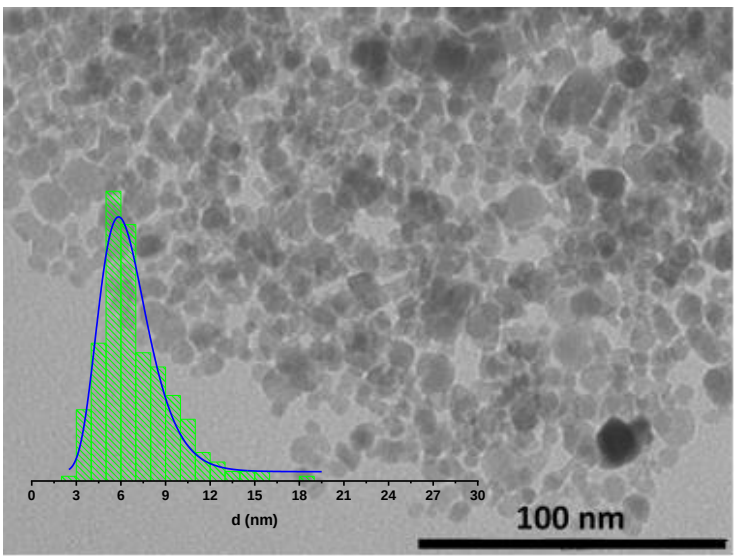

Fig. 4.5. TEM image of $Mn_{0.6}Zn_{0.4}Fe_2O_4$ together with the NPs size distribution. The continuous blue line represents the best-fit curve to a log-normal distribution.

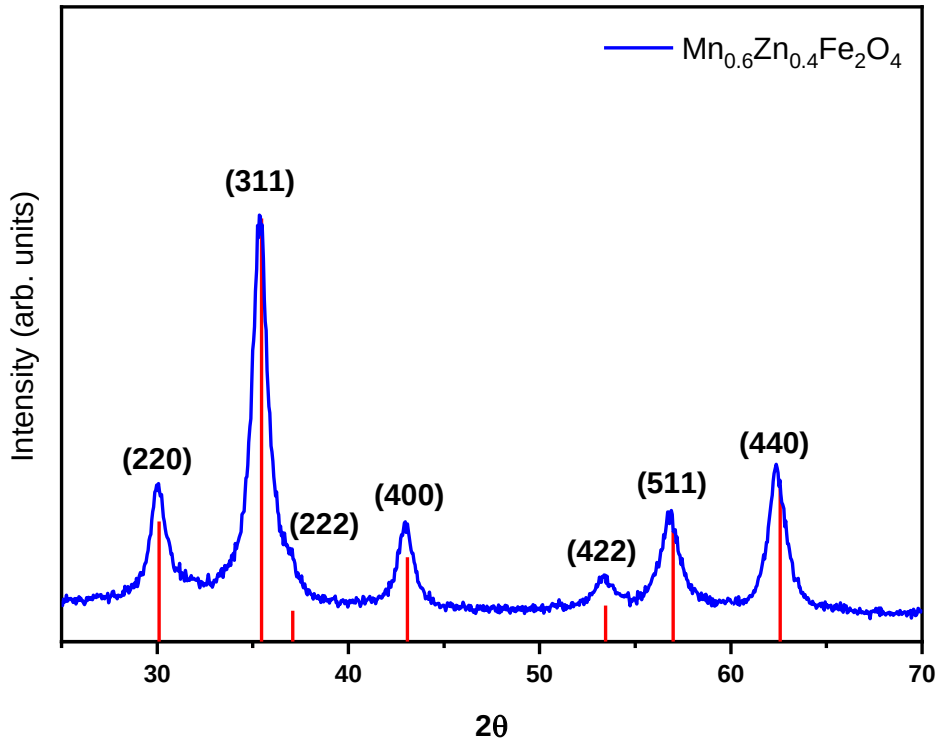

Fig. 4.6. XRD pattern of $Mn_{0.6}Zn_{0.4}Fe_2O_4$ compared to the reference pattern of magnetite (red bars; JCPDS 19-0629). The corresponding *hkl* indexes are also reported.

The field dependence of the magnetization of the $Mn_{0.6}Zn_{0.4}Fe_2O_4$ sample was investigated at room temperature (300 K) (Figure 4.7). As expected for manganese-zinc ferrites NPs of this size, within the experimental error (1-2 mT), no magnetic irreversibility was observed at this temperature. The MNPs are thus in the superparamagnetic state, a property generally required to reduce the losses associated to a hysteretic behaviour [13]. Moreover, the M_S value, approximated to the magnetization recorded at the highest experimental measuring field (5 T), was 60 Am^2/kg. This value, even if comparable with the M_S value reported in the literature for NPs of

the same composition and obtained by a similar synthetic strategy [12], is too low to use this material for the production of inductors in the 2-5 MHz frequency range.

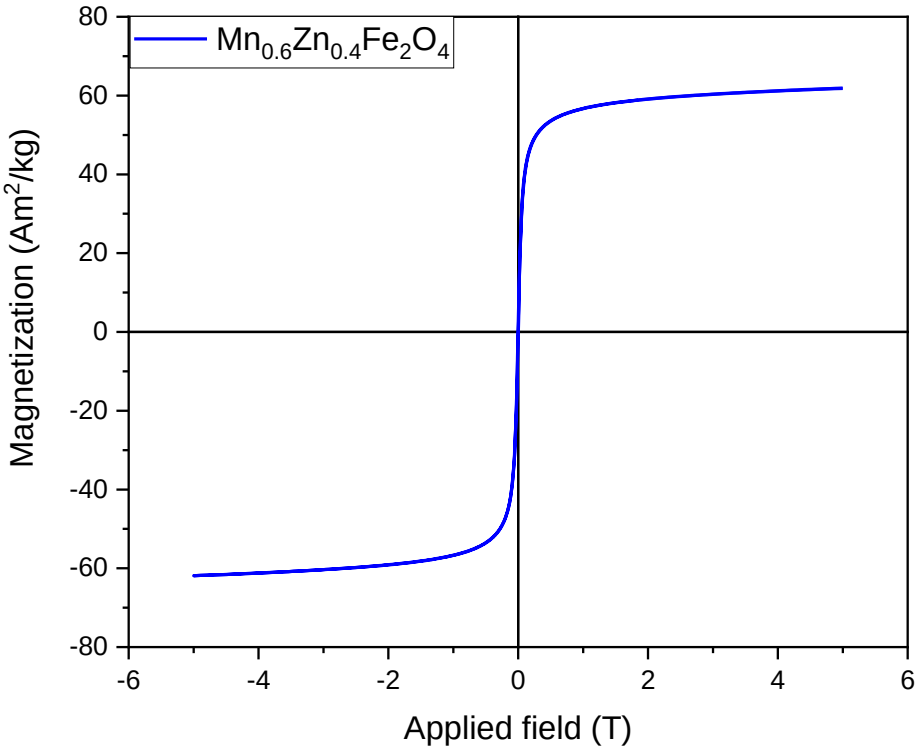

Fig. 4.7. Room temperature field dependence of the magnetization of $Mn_{0.6}Zn_{0.4}Fe_2O_4$ measured in the field range ± 5 T.

Thus, $Mn_xZn_yFe_zO_4$ (x+y+z=3) NPs of different composition were prepared using the same synthetic method used for $Mn_{0.6}Zn_{0.4}Fe_2O_4$ NPs, with the aim to experimentally investigate how the composition modifies the magnetic properties of this kind of mixed ferrite at the nanoscale in order to identify the best one for the desired application.

In particular, a series of $Mn_xZn_yFe_zO_4$ NPs with $x = 0.6$ and $0.1 \leq y \leq 0.4$

was first considered. Then, in order to better compare the effect of Mn/Zn ratio, a second series with no Fe^{2+} (x+y =1) was prepared, varying the Mn to Zn ratio from 0.7:0.3 to 0.5:0.5. Finally, a last sample of $Mn_{0.2}Zn_{0.2}Fe_{2.6}O_4$ composition was synthesized. This particular composition was selected because it corresponds to that of a sintered commercial product (ML91S) currently used at Vicor for the production of electronic devices operating in the range 1-2 MHz, and which is used as a reference to evaluate the properties of our samples.

The main chemical and structural parameters of the synthesized samples are summarized in Table 4.2.

The lattice parameter increases with the Mn-Zn-content in agreement with literature data on bulk and nanostructured mixed manganese zinc ferrites [4, 5], confirming that the Zn^{2+} ions are effectively incorporated in the ferrite lattice. Moreover, when the lattice parameter of samples with the same Mn content (x = 0.6) but different Zn content ($0.1 \leq y \leq 0.4$) is compared, a linear behavior is observed. The theoretical estimation of the variation of the lattice parameter with metal ion distribution among different cavities, performed following the model proposed in Ref. [14] and using the equation 3.1, shows that a linear increase, as the one here observed, is possible only if Zn^{2+} ions replace Fe^{3+} in *Td* cavities. It is also interesting to note that all the synthesized samples show a very similar grain size. This is an important advantage provided by the selected synthetic method, which allows for a better comparison among the samples and for the identification of the best composition at the nanosize.

Sample	d_{TEM} (nm)	d_{XRD} (nm)	a (Å)	x	y	z
$Mn_{0.6}Zn_{0.1}Fe_{2.3}O_4$	8.5 ± 1.9	9.1(6)	8.423(1)	0.63	0.11	2.26
$Mn_{0.6}Zn_{0.2}Fe_{2.2}O_4$	7.9 ± 2.0	8.5(5)	8.443(1)	0.61	0.19	2.20
$Mn_{0.6}Zn_{0.3}Fe_{2.1}O_4$	8.0 ± 1.9	8.7(5)	8.456(1)	0.62	0.33	2.05
$Mn_{0.6}Zn_{0.4}Fe_2O_4$	7.0 ± 2.0	7.6(5)	8.467(2)	0.63	0.41	1.96
$Mn_{0.5}Zn_{0.5}Fe_2O_4$	7.6 ± 2.3	7.6(5)	8.452(2)	0.49	0.52	1.99
$Mn_{0.7}Zn_{0.3}Fe_2O_4$	7.2 ± 2.5	7.3(6)	8.498(2)	0.71	0.32	1.97
$Mn_{0.2}Zn_{0.2}Fe_{2.6}O_4$	7.9 ± 2.8	8.1(6)	8.421(1)	0.22	0.21	2.57

Tab. 4.2. Chemical and structural properties of $Mn_xZn_yFe_zO_4$ NPs. d_{TEM}: NPs average diameter and standard deviation obtained from TEM analysis; d_{XRD}, a: crystallite mean size and lattice parameter obtained from XRD data analysis (errors on the least significant digit are reported in brackets); x, y, z: Mn, Zn and Fe content obtained from ICP analysis.

The field dependence of the magnetization of the $Mn_xZn_yFe_zO_4$ samples investigated at 300 K, shows that, as expected for manganese-zinc ferrites NPs of this size, all the samples are superparamagnetic at room temperature since no coercivity, nor remanence are observed ($\mu_0 H_C < 2$ mT and $M_R \sim 1$ Am^2/kg for all the samples). The M_S values, reported in Table 4.3, range between 41 and 74 Am^2/kg. This spread is consistent with literature data for NPs of same composition and obtained by a similar synthetic strategy and is ascribed to the low crystallinity and magnetic disorder typical of NPs prepared by this synthetic method [12, 15, 16].

Even if for some compositions (Table 4.3) M_S is higher than that of $Mn_{0.6}Zn_{0.4}Fe_2O_4$ (60 Am^2/kg), it is still too low to directly use these materials for the desired application. It is therefore necessary to introduce a second process to improve the magnetic properties of the powder up to the target.

Sample	M_{5T} 300 K (Am^2/kg)
$Mn_{0.6}Zn_{0.1}Fe_{2.3}O_4$	60
$Mn_{0.6}Zn_{0.2}Fe_{2.2}O_4$	62
$Mn_{0.6}Zn_{0.3}Fe_{2.1}O_4$	57
$Mn_{0.6}Zn_{0.4}Fe_2O_4$	60
$Mn_{0.5}Zn_{0.5}Fe_2O_4$	41
$Mn_{0.7}Zn_{0.3}Fe_2O_4$	70
$Mn_{0.2}Zn_{0.2}Fe_{2.6}O_4$	74

Tab. 4.3. Magnetic parameters of $Mn_xZn_yFe_zO_4$ NPs. M_{5T}: experimental magnetization measured at 5T.

4.1.2 High temperature thermal treatments of $Mn_xZn_yFe_zO_4$ nanopowders

To improve the spin ordering of the material and to promote the migration of the ions into crystallographic sites with lower energy, with the consequent improvement of the magnetic properties (M_S, in particular), the obtained products were exposed to a high temperature treatment. In fact, as reported in the literature [17, 18], an annealing process carried out on nanostructured samples can reduce magnetic disorder and increase the saturation magnetization. However, the thermal treatment can also cause an excessive growth of the grains and/or appearance of other crystallographic phases that could lead to the loss of the desired physical and magnetic properties associated to the nanometric structure. It was therefore very important to find the optimal conditions to maximize the saturation magnetization while minimizing these undesired effects. The thermal treatment was carried out in a tubular furnace (Figure 4.8), at different temperatures from 500 ° C up to 1200 ° C with 100 °C step, under inert atmosphere (N_2 flow, to prevent Mn^{2+} and Fe^{2+} ions oxidation) with a heating rate of 10 °C/min and a dwell time of two hours (Figure 4.9). A degas step at 130 °C for 2 h was added to evaporate and remove any residual solvent present in the nanopowders, which could react with the material at high temperature. Then the samples were heated to the desired temperature, with a heating rate of 10 °C/min, kept in isotherm for 2 hours and then left to cool down to the room temperature. In the case of annealing temperatures higher than 700 °C, a controlled cooling step was introduced in the process, with a cooling rate of 5 °C/min up to 700 °C, to avoid thermal stress on the furnace mullite ($Al_{4+2x}Si_{2-2x}O_{10-x}$) tube.

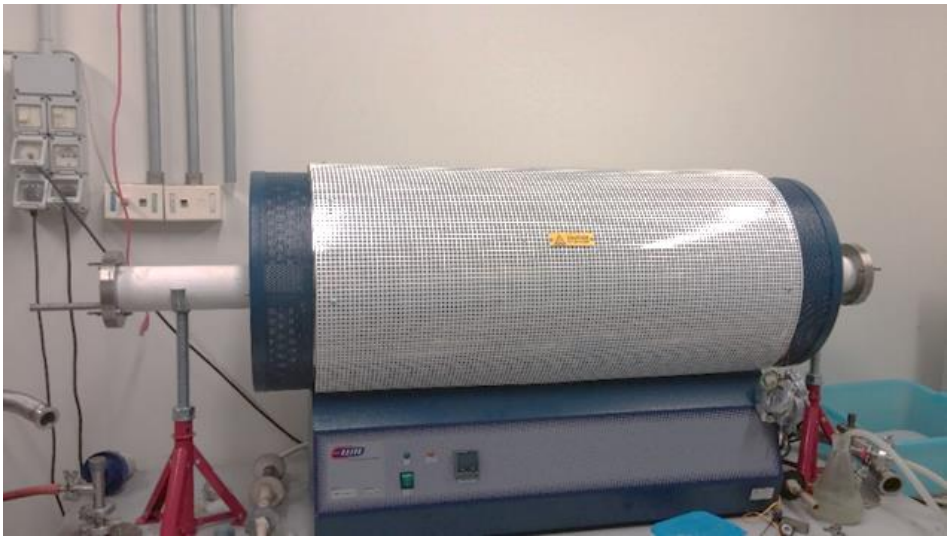

Fig. 4.8. Tubular furnace used for high temperature thermal treatment of nanopowders under inert atmosphere.

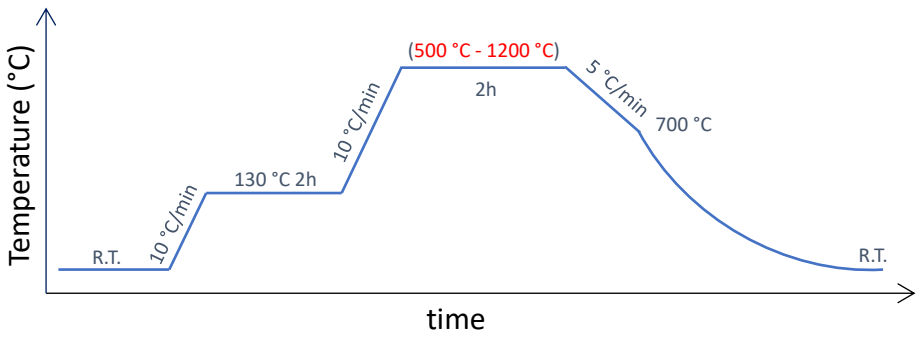

Fig. 4.9. Schematic diagram of the thermal treatments.

Since the obtained results as a function of the thermal cycle, were similar for all the compositions, for the sake of clarity, only the sample $Mn_{0.2}Zn_{0.2}Fe_{2.6}O_4$ is discussed in the following. Representative XRD patterns of the $Mn_{0.2}Zn_{0.2}Fe_{2.6}O_4$ sample annealed at different temperatures between 500 °C and 1200 °C are shown in Figure 4.10.

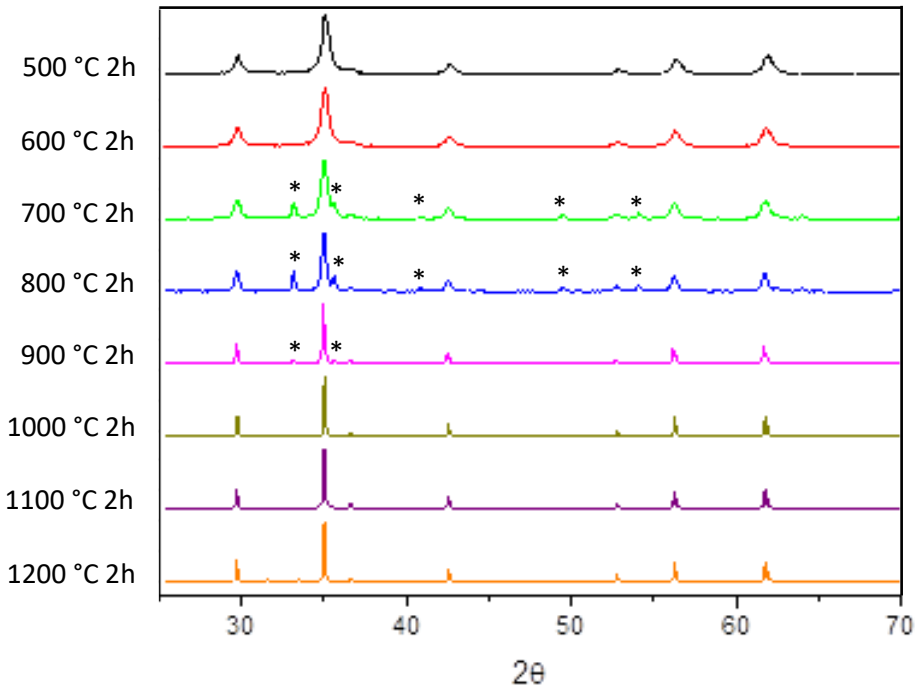

Fig. 4.10. XRD patterns of the $Mn_{0.2}Zn_{0.2}Fe_{2.6}O_4$ sample annealed at different temperatures, reported in the vertical axis, for two hours. For samples heated at 700, 800 and 900 °C it is possible to distinguish the reflexes of hematite (α-Fe_2O_3) indicated with black asterisks (*****).

The recorded XRD patterns, depict the presence of satellite crystallographic phase, identified as hematite (α-Fe_2O_3, JCPDS 86-2368) for the samples heated at 700, 800 and 900 °C, which rearrange in the cubic spinel structure for higher temperatures. The relative weight amount was calculated by Rietveld refinement and revealed a presence of ca. 20 % of hematite in the powder heated at 700 °C and 800 °C and of ca. 5 % in the powder heated at 900 °C. Probably, this result is due to a rearrangement of a part of Mn-Zn ferrite during the annealing process generating hematite (it is the most stable iron oxide crystallographic phase after the oxidation of Fe^{2+} to Fe^{3+}) with consequent expulsion of small amount of amorphous ZnO and MnO. In fact, for all the thermal treated samples, the lattice parameter does not change with the thermal treatment and remains equal to that of the as-synthesized powder; conversely, the crystallite diameter grows as the temperature of the thermal treatment increases, going from ca. 10 nm at 500 °C up to the micrometric scale when the annealing temperature overcomes 900 °C. To evaluate morphology and grain size of the samples exposed to the thermal treatment, SEM (Scanning Electron Microscopy) images were acquired (Figure 4.11). These images clearly show the increase in grain size as a function of the heating temperature; at 500 °C and 700 °C, the grains still have nanometric sizes, while the sample heated at 900 °C is mainly constituted by large aggregates of particles of roughly micrometric size and the sample heated at 1100 °C shows partially sintered micrometric grains. These data are consistent with those obtained from the XRD patterns.

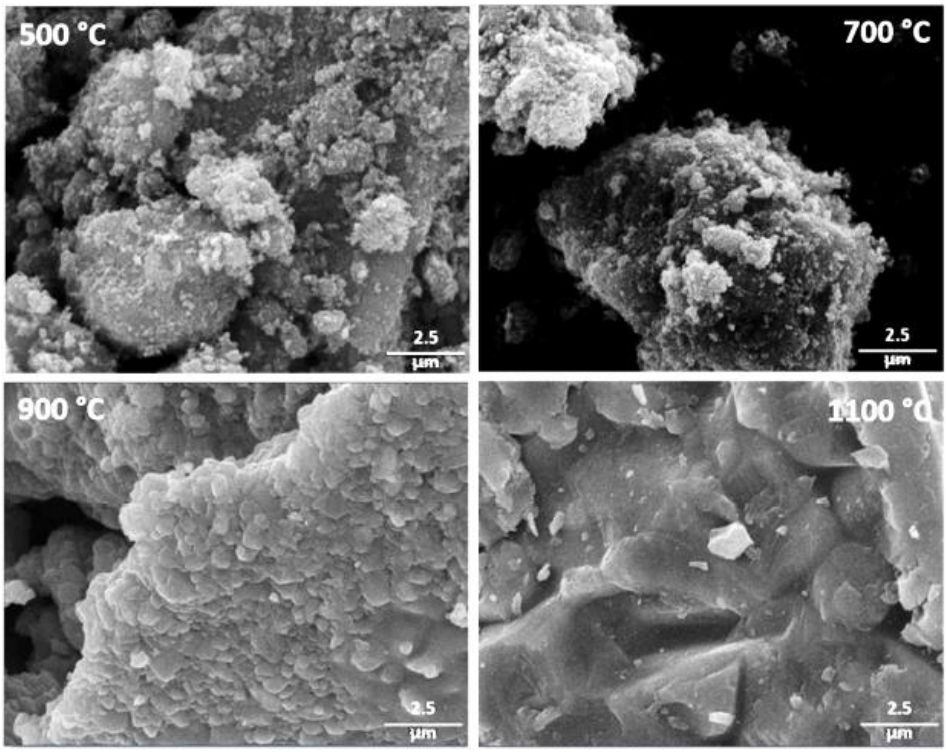

Fig. 4.11. SEM images of the $Mn_{0.2}Zn_{0.2}Fe_{2.6}O_4$ sample annealed at different temperature acquired at the same magnification (8000x).

Concerning the magnetic properties, the M_S of all the sintered samples increases with the temperature of the thermal treatment, reaching a maximum at 1100 °C. The highest value is indeed observed for $Mn_{0.2}Zn_{0.2}Fe_{2.6}O_4$ heated at 1100 °C for 2 hours, which has M_S = 108 Am^2/kg. The enhancement of M_S can be ascribed to the expected crystallinity improvement and increase of the magnetic order [17-19], pointing out the validity of the adopted approach. Furthermore, the coercive field remains negligible (below the instrumental accuracy), proving the preservation of the soft magnetic behaviour, typical of this kind of ferrite (Figure 4.12). In order to better appreciate the properties of

our sample we compared it with the powder obtained by grinding commercial sintered plate in use at Vicor for application at 2 MHz. The field dependence of the magnetization of the two powders at 300 K are shown in Figure 4.12. Although our sample exhibits a considerable higher M_S compared to the commercial analogue, its static initial permeability, evaluated from the initial slope of the M vs H curve, is slightly lower (Figure 4.12). However, the two values are not directly comparable since the permeability value is strongly affected by the density of material. Since the commercial powder was obtained by coarsely grinding a high density sintered bulk material, we should expect a much larger density than our powders, and consequently a higher permeability. Nevertheless, the compaction of our $Mn_{0.2}Zn_{0.2}Fe_{2.6}O_4$ powder, which has not been investigated in details, should lead to a significant improvement of the final permeability up to higher value than the commercial product (this latter result is expected from the higher M_S obtained). As a simple test, we observed that, measuring our sample as powder and pressed pellet (in the inset of Figure 4.12), the initial permeability of the pellet sample is much higher than the powder one and even of the commercial sample. In conclusion, despite the annealing treatment at 1100 °C caused a partial sintering of the material, with consequent growth of the grains, the enhancement of M_S value up to 108 Am^2/kg, ascribed to the crystallinity and magnetic order increase, makes the sample very promising for the production of inductors in the 2-5 MHz frequency range. Moreover, it is interesting to note that, even after the thermal treatment at 1100 °C for 2h, the samples preserve the magnetic reversibility already observed in nanopowders. As already mentioned, this magnetic behaviour is very important because allows a significant decrease of the dissipation of energy into heat through hysteresis losses [13].

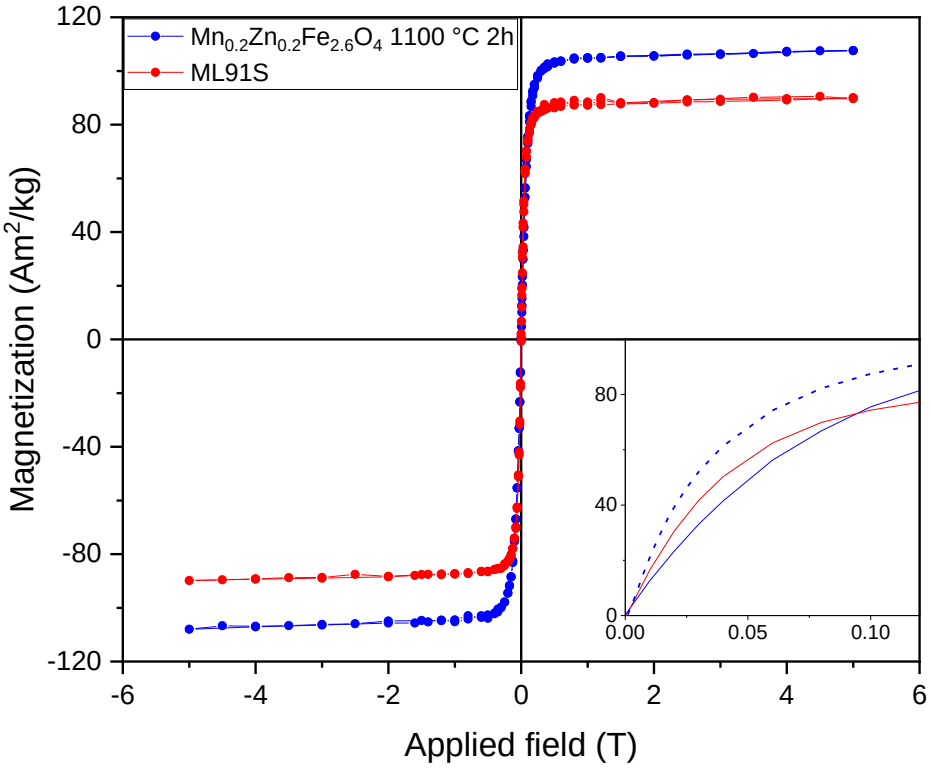

Fig. 4.12. Room temperature field dependence of the magnetization of $Mn_{0.2}Zn_{0.2}Fe_{2.6}O_4$ 1100 °C 2h and ML91S measured in the field range ± 5 T. In the inset, the low field region is reported, including data for $Mn_{0.2}Zn_{0.2}Fe_{2.6}O_4$ 1100 °C 2h in pellet (dashed blue line).

4.1.3 Large-scale production of $Mn_{0.2}Zn_{0.2}Fe_{2.6}O_4$ nanopowders

On the basis of the obtained results, and with the aim of applying the material to the large-scale production of inductors for high-frequency electronic devices, further attention was focused on the preparation of the sample with the highest saturation magnetization values, i.e. $Mn_{0.2}Zn_{0.2}Fe_{2.6}O_4$ annealed at 1100 °C for 2 hours, at the industrial scale. The industrial scale-up of the synthetic process was carried out in collaboration with the chemical company Cabro S.p.A. in Arezzo.

The large-scale synthesis was performed on a 100 liters glass reactor (reaction volume of 50 liters, Figure 4.13), starting from aqueous solution of manganese, zinc, iron (II) and iron (III) chlorides with industrial-grade purity, obtaining ca. 0.5 kg of nanometric product (see experimental section for synthetic details). The synthetic method was substantially analogous to that developed on the laboratory scale but, due to the large reaction volumes and quantities of reagents, longer times for many operations, mainly the purification time and heating time of the basic aqueous solution up to boiling point (ca. 2h), were required. After two hours at reflux, the black-brown mixture was cooled to room temperature (1 h) and removed from the reactor with a vacuum pump, and the obtained product was separated by magnetic decantation with a big permanent magnet (ca. 20 cm diameter and 4 cm thickness). The washing procedure was the most critical point of the overall process. In fact, the procedure developed in the laboratory, including several washings with water and two washing with ethanol, proved to be inadequate at the large scale.

Fig. 4.13. Comparison between the 100 liters industrial reactor (left) and the 1 liter round bottom flask (right) used for the laboratory-scale synthesis.

Indeed, it required a too long decantation time and excessive volumes of water, ethanol and acetone. Therefore, the washing procedure has been modified limiting the magnetic decantation to small volumes (ca. 5 liter of the black-brown mixture at a time). However, this procedure has inevitably increased the washing time of the whole batch with respect to the laboratory scale, increasing the risk of partial oxidation of Mn^{2+} to Mn^{4+} and Fe^{2+} to Fe^{3+}. Finally, the obtained product was dried under N_2 flow to prevent oxidation and stored in an inert atmosphere.

The as-prepared nanometric powder was then characterized by XRD, ICP-AES and SQUID magnetometry and the obtained results proved that the industrial product has the same structural (d_{XRD} = 8.6(3) nm; a = 8.415(3) Å) and magnetic properties (M_S = 73 Am^2/kg) as the laboratory-scale samples. The nanostructured material was then exposed to thermal treatment at 1100 ° C for 2 hours under nitrogen flow in a tubular furnace and characterized by XRD and ICP-AES. The recorded XRD pattern of the $Mn_{0.2}Zn_{0.2}Fe_{2.6}O_4$ sample prepared in Cabro S.p.A. and annealed at 1100 °C (Figure 4.14) shows, in addition to the spinel structure, the presence of satellite crystallographic phase, identified as hematite (ca. 20 %) indicating that, probably during the annealing step, a part of Mn-Zn ferrite rearranged generating hematite with consequent expulsion of small amount of amorphous ZnO and MnO. In fact, the lattice parameter of the $Mn_{0.2}Zn_{0.2}Fe_{2.6}O_4$ ferrite prepared in Cabro S.p.A. and annealed at 1100 °C is similar to that of the nanometric powder and $Mn_{0.2}Zn_{0.2}Fe_{2.6}O_4$ obtained in the laboratory and treated in the same way, suggesting the two ferrites share similar composition and metal ion distribution. However, this result could also be due to the crystallization of small amounts of unreacted amorphous impurities (iron hydroxide or iron oxo-hydroxide) adsorbed on the surface of the nanoparticles, or to a partial oxidation of Fe^{2+} to Fe^{3+}

during the long industrial washing process.

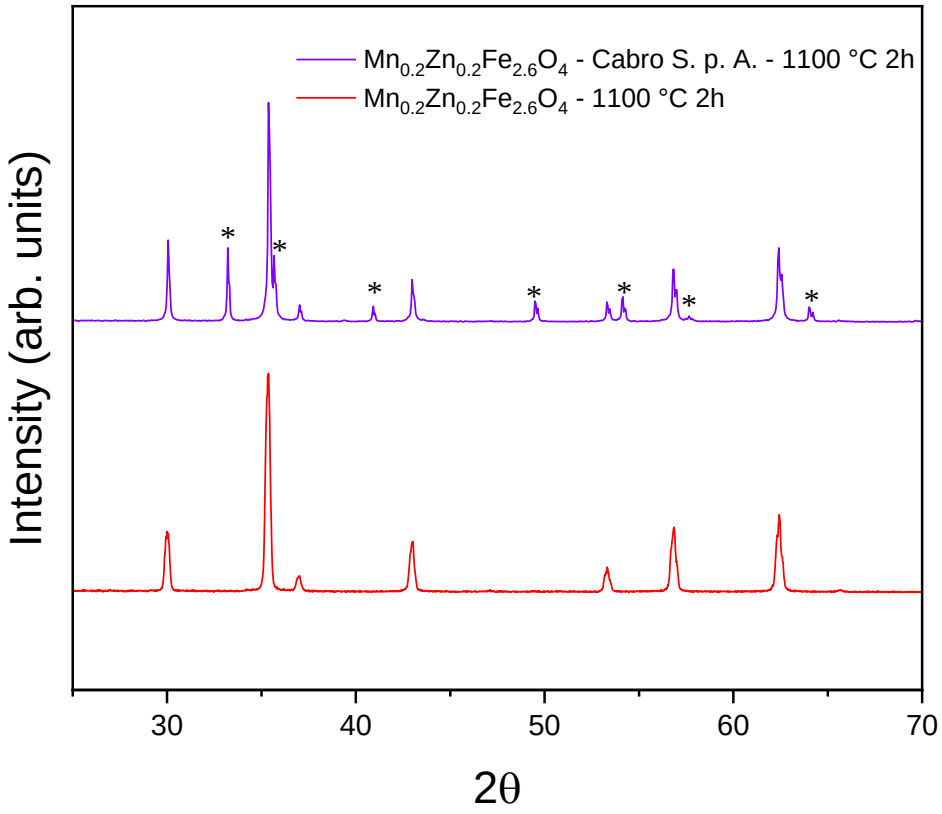

Fig. 4.14. XRD patterns of the samples $Mn_{0.2}Zn_{0.2}Fe_{2.6}O_4$ - 1100 °C 2h (red line) and $Mn_{0.2}Zn_{0.2}Fe_{2.6}O_4$ – Cabro S. p. A. - 1100 °C 2h (violet line). The reflexes of hematite (α-Fe_2O_3) are indicates with black asterisks (*****)).

4.2 Ferrite based MNPs for energy applications

As mentioned in the introduction, MNPs show remarkably promising properties which in principle can be exploited to develop permanent magnet. Permanent magnets are key elements for many technological devices that are largely used in everyday life, such as electronic devices, hard disks, automotive, wind turbines, and hybrid electric vehicles [20-22]. The kind of applications of a permanent magnet is determined by the magnetic energy density that can be stored within the material per volume unit, which is represented by the maximum energy product, $(BH)_{max}$ (Figure 1.4). The most powerful permanent magnets, i.e. those with largest $(BH)_{max}$, are based on Rare Earth (RE) elements. RE-magnets are currently used in most of the industrial products requiring magnetic energy storage, because their economic convenience (abundance/price compared to their major performances) was unquestionable until a few years ago. Nowadays, however, the concentration of the raw material by non-western countries (95% of the RE mines are controlled by China), with the consequent high supply risk, and the environmental issues related to their extraction have brought up several concerns about the future of RE market [23]. At present, a strong research activity is thus focused on finding viable alternatives to RE-based permanent magnets, which can allow their replacement at least in all those applications where moderate energy product is required and no major volume restriction are operating (mainly in automotive and energy industries). Among the different approaches proposed to maximize the $(BH)_{max}$, a lot of attention has been paid towards the development of RE-free nanostructured hybrid materials based on the coupling of a hard magnetic material with a soft magnetic one, producing

a so-called exchange-spring permanent magnet (Figure 1.6), i.e., a material which takes benefits form the properties of both components. [24, 25].
With regard to the permanent magnet research area, the idea we developed here is to couple a hard magnetic material ($SrFe_{12}O_{19}$) to a soft magnetic one ($Mn_xZn_yFe_zO_4$) to maximize the $(BH)_{max}$ of the final product. Since the hard magnetic component, $SrFe_{12}O_{19}$, is a standard material, already deeply investigated and employed as single-component permanent magnet, the work has been mainly addressed to the synthesis of a soft material with high M_S value, which could be potentially used as soft phase in the coupling. This study was included in the framework of the European project. EU-H2020 "Anisometric permanent hybrid magnets based on inexpensive and non-critical materials" AMPHIBIAN (Project n. 720853), which aims at increasing the energy product by improving the remanent magnetization of hybrid materials with only a moderate sacrifice of coercivity, exploiting the magneto-dipolar interactions within the material and/or exchange coupled nanosystems. In particular, the goal is to develop enhanced ferrite magnets to contribute to a greener technological industry, since, although ferrite-based magnets can store limited magnetic energy, they are cost-effective and their production is simple and environmentally friendly.

4.2.1 Synthesis and structural and magnetic characterization of $Zn_yFe_{(1-y)}Fe_2O_4$ NPs

The $Mn_{0.2}Zn_{0.2}Fe_{2.6}O_4$ sample, previously developed for electronical applications, could be a good candidate as soft component to be coupled to standard Sr-ferrite to realize an exchange-spring magnet device. Thanks

to the high saturation magnetization (108 Am^2/kg against ca. 65-70 Am^2/kg of $SrFe_{12}O_{19}$), if added in a percentage not too high to produce a drastic decrease of the magnetic anisotropy of the hard phase, (ca. 10% w/w) it can cause a small enhancement of the remanence of the hard/soft hybrid nanocomposite 5-7 %).

We therefore explored the possibility to improve the results by synthesizing other spinel ferrites particles with different metal composition. As an alternative, we tried to synthesize a series of non-stoichiometric Zn ferrite. More in detail, zinc doped ferrites with variable composition, $Zn_yFe_{(1-y)}Fe_2O_4$ ($0 \leq y \leq 0.4$), were prepared following the same protocol used for $Mn_xZn_yFe_zO_4$: $Zn_yFe_{(1-y)}Fe_2O_4$ NPs were synthesized by co-precipitation starting from zinc, iron (II) and iron (III) chlorides, and then the obtained nanopowders were exposed to high temperature thermal treatments. To investigate the effect of the Zn substitution on the magnetic properties of the Zn ferrites series and to identify the stoichiometry and the thermal treatment conditions to maximize the M_S of the material, the samples were characterized by TEM, SEM, XRD, ICP-AES and SQUID magnetometry.

As described previously, in bulk Zn-ferrites, a gradual increase of M_S is expected with the progressive introduction of diamagnetic Zn^{2+} ions in the magnetite inverse spinel structure. Since the Zn^{2+} ions tend to occupy T_d sites, the antiferromagnetic coupling between Fe^{3+} in T_d and O_h sites is partially removed and the sublattices more unbalanced. Assuming all Zn^{2+} ions occupy T_d cavities, the magnetic moment at 0 K for non-stoichiometric Zn ferrites, estimated using equation 4.1, and considering a Mn content x = 0 will be equal to:

$$\mu = (4+6y)\mu_B \qquad (4.2)$$

However, as previously explained, the mechanism holds up until the Zn^{2+} substitution reaches *ca*. half of the total number of divalent ions [5]. For higher percentage, M_S starts decreasing, due to the weakening of the magnetic exchange between T_d and O_h sites, which induces the destabilization of the ferrimagnetic order and the local canting of the spins in the O_h sites [6 - 8]. For this reason, the work was addressed to investigate only non-stoichiometric Zn ferrites with $y < 0.5$.

In the following, samples will be labeled as ZFOyy, where yy denotes the zinc content (i.e., y = 0.1 corresponds to yy = 01). The main chemical and structural parameters of the synthesized samples are summarized in Table 4.4.

Sample	d_{TEM} (nm)	d_{XRD} (nm)	a (Å)	y
ZFO00	10.7 ± 2.9	10.0(5)	8.393(5)	0.00
ZFO01	9.5 ± 2.3	9.5(4)	8.399(2)	0.09
ZFO02	10.8 ± 2.3	10.3(8)	8.404(3)	0.18
ZFO03	9.9 ± 2.2	9.4(3)	8.413(3)	0.27
ZFO04	9.5 ± 2.4	9.3(3)	8.416(3)	0.40

Tab. 4.4. Chemical and structural properties of ZFOyy NPs. d_{TEM}: NPs average diameter and standard deviation obtained from statistical analysis of the TEM images; d_{XRD}, a: crystallite mean size and lattice parameter obtained from XRD data analysis (errors on the least significant digit are reported in brackets); y: Zn content obtained from ICP analysis.

The effective stoichiometry of the obtained samples, checked by elemental analysis (ICP-AES), confirmed the amount of Zn and Fe introduced into the spinel lattice was, within the experimental error, almost identical to that set in the synthesis.

Since TEM images were similar for all the samples of the series, only the image of sample ZFO03 is reported in Figure 4.15, as representative of the whole series, together with the NPs size distributions, fitted to a log-normal function.

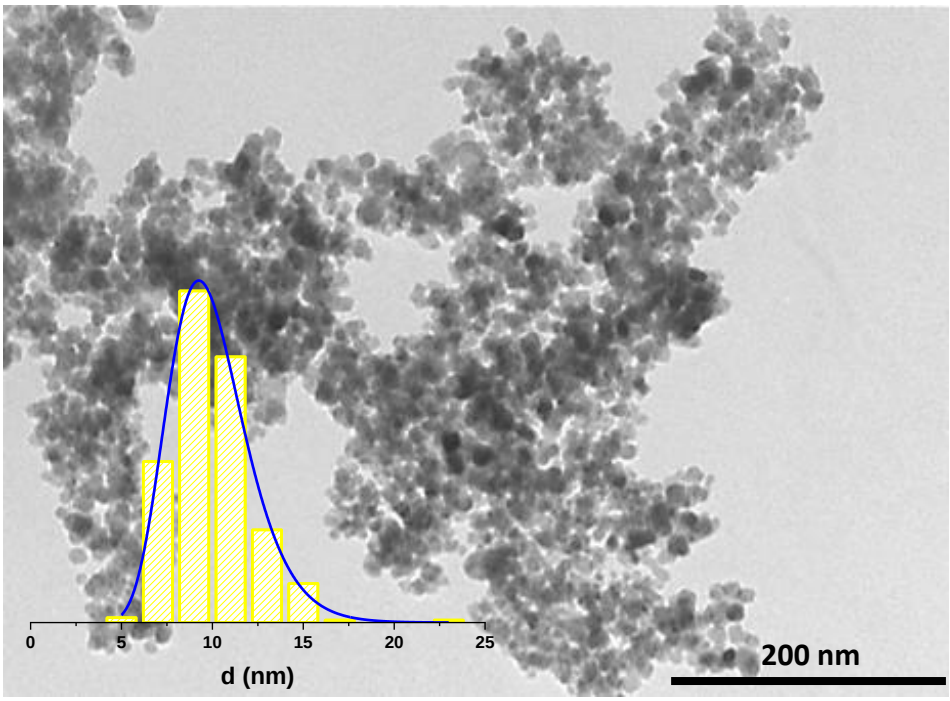

Fig. 4.15. TEM image of ZFO03 NPs. In the insets, the corresponding diameter distribution evaluated over 370 NPs is reported. The continuous line represents the best-fit curve to a lognormal distribution. The scale bar corresponds to 200 nm.

All the samples are composed of monodispersed NPs of *ca.* 10 nm diameter with irregular shape. Mean and standard deviation values are statistically evaluated from the size histograms. Since the synthesis is carried out without surfactants which can prevent NP aggregation due to the strong magnetic interactions, large clusters of NPs can be observed in the TEM images. Thus, diameter distribution was evaluated measuring the NPs at the edges of the aggregates.

Only the cubic ferrite phase is observed in the XRD patterns (Figure 4.16): this suggests that the introduction of Zn does not induce the formation of secondary phases other than the spinel.

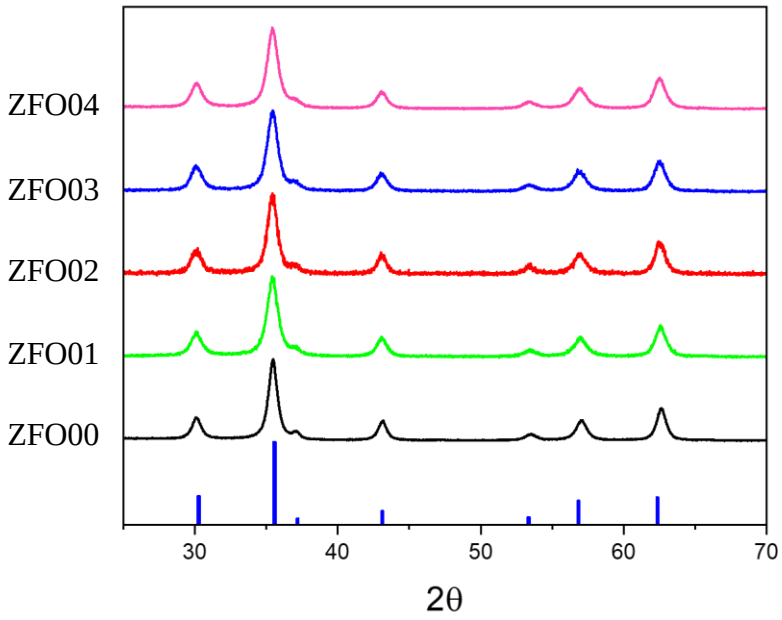

Fig. 4.16. X-ray diffraction patterns of ZFOyy NPs compared to the reference pattern of magnetite (blue bars, PDF 88-0315).

Lattice parameter, a, and mean crystallite diameter, d_{XRD}, were evaluated by TOPAS software (Bruker) using the method of fundamental parameter approach, considering a cubic space group $Fd\overline{3}m$. The lattice parameter increases with Zn-content (Figure 4.17 and Table 4.4) in agreement with the literature data on bulk and nanostructured zinc ferrites [4, 5], confirming that the Zn^{2+} ions are effectively incorporated in the ferrite lattice.

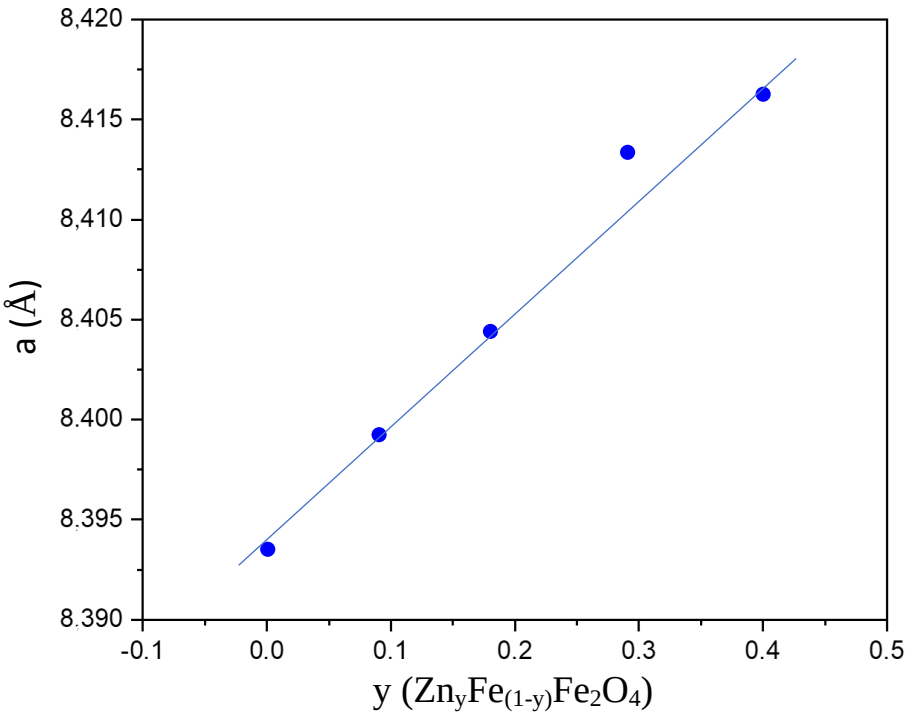

Fig. 4.17. Lattice parameter dependence on the Zn-content, y (error is within 0.005 Å). The straight line is a guide for the eyes.

Moreover, the theoretical estimation of the variation of the lattice parameter with the metal ion distribution among different cavities,

performed following the model proposed in Ref. [14] and using the equation 3.1, shows that a linear increase, as the one here observed, is possible only if Zn^{2+} ions replace Fe^{3+} in *Td* cavities. Finally, the good agreement between the average NPs diameter obtained from TEM and the crystallite size from XRD measurements (Table 4.4) suggests that all samples are composed by highly ordered, single crystal NPs.

To evaluate the effect of the Zn substitution on the magnetic properties of $Zn_yFe_{(1-y)}Fe_2O_4$ NPs, the field dependence of the magnetization was investigated at 300 K by using a SQUID magnetometer. Since magnetization curves were similar for all the samples of the series, only the M(H) curve of the sample ZFO02 is reported in Figure 4.18.

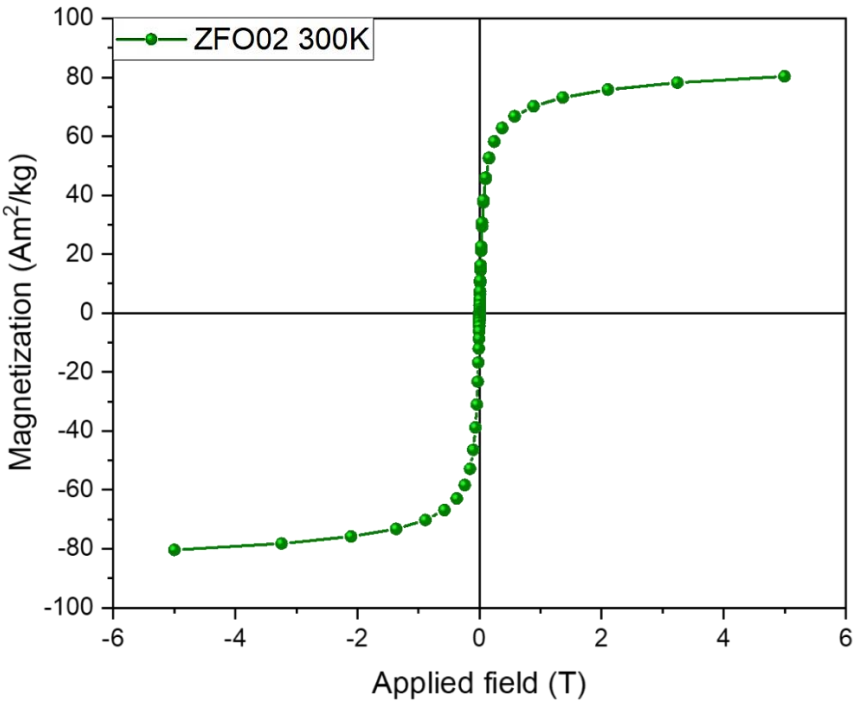

Fig. 4.18. Magnetization curve, *M*(*H*), of ZFO02 NPs measured at room temperature (300 K).

The field dependence of the magnetization of the samples show that, within the experimental error (1-2 mT), all the samples of the series are superparamagnetic at room temperature since no coercivity, nor remanence are observed.

As discussed above, the aim of this work is to obtain a soft magnetic material with a high M_S value. The saturation magnetization dependence on the Zn-content is shown in Figure 4.19 and the M_S values of the synthesized samples are reported in Table 4.5.

Sample	y	M_{5T} 300 K (Am^2/kg)
ZFO00	0.00	69
ZFO01	0.09	75
ZFO02	0.18	79
ZFO03	0.27	77
ZFO04	0.40	76

Tab. 4.5. M_S values of ZFOyy NPs and Zn content obtained from ICP analysis, *y*. The M_S was approximated to the experimental magnetization at 5 T.

For magnetite NPs, the M_S value, approximated to magnetization recorded at the highest experimental field (5 T), was 69 Am^2/kg. This value, even if lower than that of the corresponding bulk material (92 Am^2/kg at 300 K [2]), is comparable with the M_S value reported in the literature for magnetite NPs prepared by co-precipitation [16], due to the low

crystallinity and magnetic disorder typical of NPs prepared by this synthetic method.

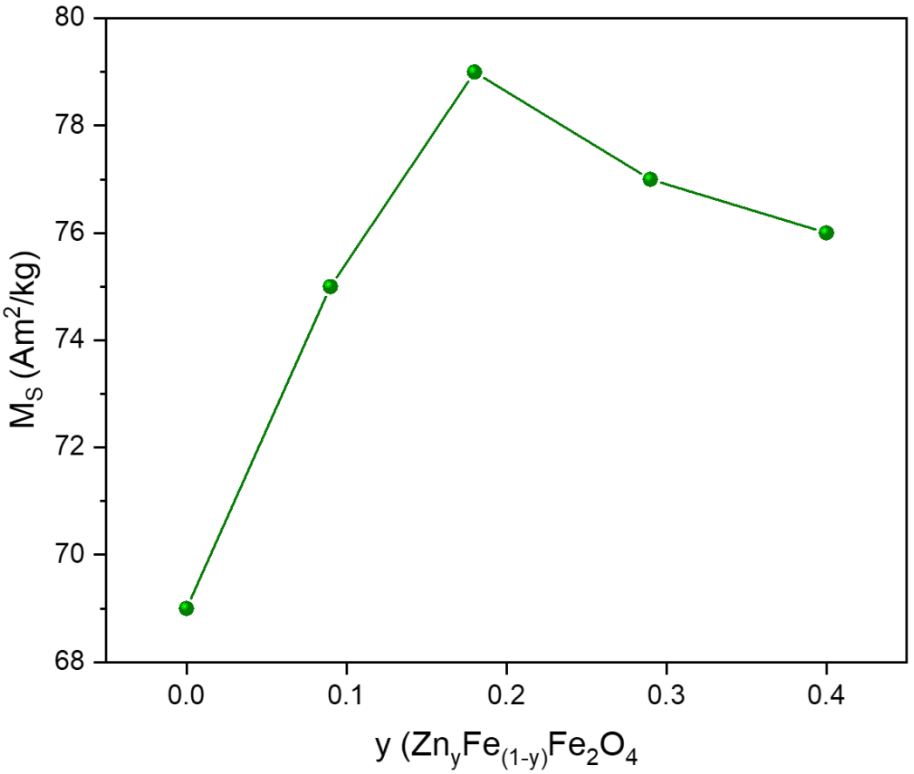

Fig. 4.19. Saturation magnetization dependence on the Zn-content, *y*. The experimental M_S was approximated to 5 T.

In Figure 4.19 an increase of M_S with the Zn-content is observed up to the maximum value for the sample ZFO0.2 (79 Am^2/kg) and then it decreases down to 76 Am^2/kg for the sample ZFO04. These M_S values are lower than those observed for the corresponding bulk Zn-ferrites but comparable with that reported in the literature for nanometric Zinc-ferrites, obtained by a similar synthetic strategy [15, 16]. As described above, in bulk Zn-ferrites,

the M_S follows a non-linear trend with the progressive introduction of diamagnetic Zn^{2+} ions in the magnetite inverse spinel structure reaching a maximum for y = 0.5. The same trend can be observed for the samples of the synthesized series, even if the maximum M_S value is shifted to lower Zn-content (y = 0.2). This behavior is due to the nanometric dimensions of the samples. In fact, at the nanoscale, the increase of spin disorder due to the weakening of magnetic exchange coupling becomes particularly relevant.

4.2.2 High temperature thermal treatments of $Zn_yFe_{(1-y)}Fe_2O_4$ nanopowders

As done for Mn,Zn doped spinel ferrite particles, a thermal treatment at high temperature (from 500 ° C up to 1100 ° C in increments of 200 °C) was applied to improve the crystallinity and to promote the migration of the ions into crystallographic sites with lower energy, so as to enhance the final magnetic properties of the material, and particularly of M_S. The thermal treatment was carried out in the same tubular furnace and following the same protocol used for $Mn_xZn_yFe_zO_4$ NPs.

Since the obtained results were similar for all the samples of the series, for the sake of clarity, only the sample ZFO03 is discussed in the following.

It is important to note that, with respect to the annealed $Mn_xZn_yFe_zO_4$ samples at 700, 800 and 900 °C, in which hematite is observed, only the cubic spinel structure is identified in the recorded XRD patterns of the Zn doped ferrites (Figure 4.20). This result is particularly relevant and confirms the goodness of the chosen thermal treatment conditions, which was not a foregone task. In fact, numerous studies reported in the literature

indicate that the spinel phase is thermally unstable and can decompose at high temperature, generating secondary crystallographic phases like wüstite (FeO), hematite (α-Fe_2O_3) and zinc oxide (ZnO) [17, 26, 27]. Moreover, as for $Mn_xZn_yFe_zO_4$ samples, the lattice parameter of the thermally treated sample does not change with the heating temperature and remains equal to that of the as-synthesized nanometric powder; conversely, the crystallite diameter grows with heating temperature from ca. 10 nm for powder treated at 500 °C up to the micrometric scale when annealing temperature overcomes 900 °C.

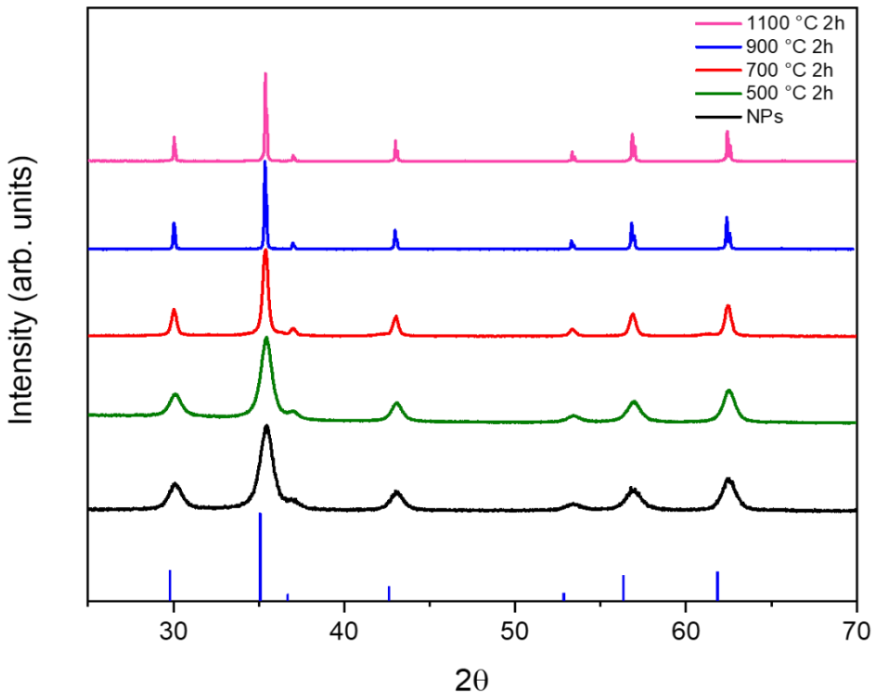

Fig. 4.20. XRD patterns of the ZFO03 sample annealed at different temperatures compared to the reference pattern of magnetite (blue bars, PDF 88-0315).

To evaluate morphology and grain size of the samples exposed to the thermal treatment, SEM images were also acquired. The grain size increases as a function of the heating temperature: at 500 °C and 700 °C the grains still have a nanometric size, the sample heated at 900 °C is mainly constituted of large aggregates of particles of roughly micrometric size, while the sample heated at 1100 °C comprises partially sintered micrometric grains. These data are consistent with those obtained from the XRD patterns.

Finally, the magnetic properties of the annealed samples were evaluated by SQUID magnetometry. The saturation magnetization dependence on the Zn-content before (black curve) and after thermal treatment are shown in Figure 4.21. As shown in Figure 4.21, an evident increase of M_S with the annealing temperature is observed for all the samples of the series. The only exception is for the sample ZFO04 heated to 500 °C in which a slight decrease of M_S is observed with respect to the untreated sample. The non-linear trend of M_S with the progressive introduction of diamagnetic Zn^{2+} ions, observed for the as-prepared nanopowders, is preserved after the thermal treatment at higher temperatures, but in this case the maximum M_S is shifted to y = 0.3. These is in agreement with the progressive minimization of spin disorder due to the growth of the grain size (we remind that in bulk Zn-ferrites, M_S reaches the maximum for y = 0.5).

The most promising sample in terms of M_S was that annealed at 1100 °C for 2 hours and with the stoichiometry $Zn_{0.3}Fe_{2.7}O_4$, that has M_S = 106 Am^2/kg (Figures 4.21 and 4.22). Moreover, even after the thermal treatment at 1100 °C for 2h the sample preserves the magnetic reversibility already observed in nano powder (Figure 4.22).

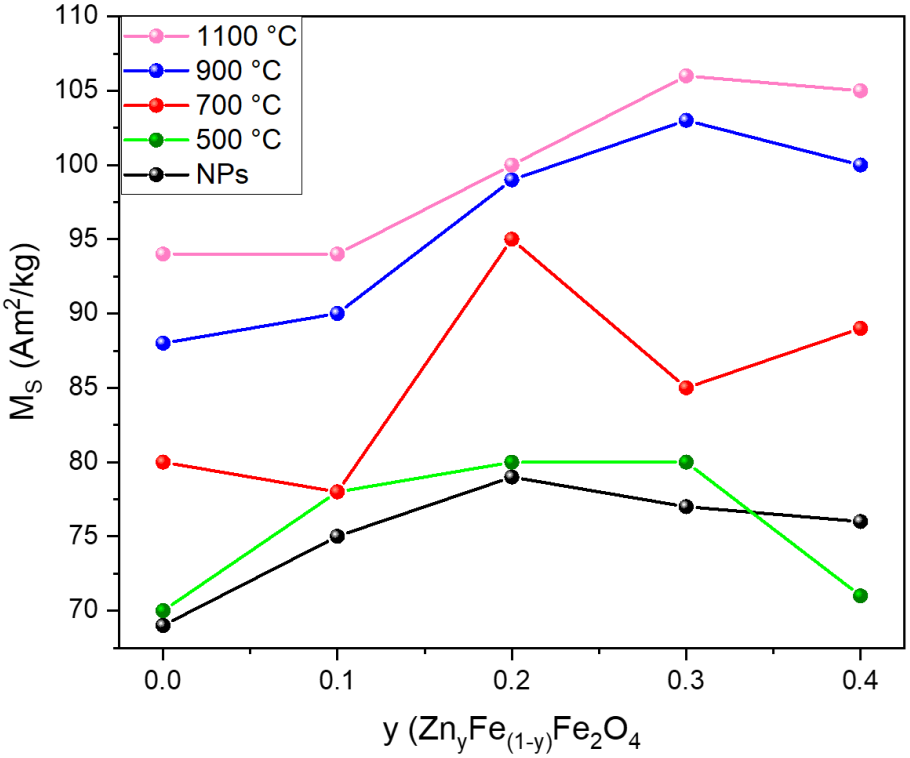

Fig. 4.21. Saturation magnetization dependence on the Zn-content, *y*, before (black curve) and after thermal cycle at different temperature: 500 °C, green curve, 700 °C, red curve, 900 °C blue curve and 1100 °C, pink curve). The experimental M_S was approximated to 5 T.

As for the sample $Mn_{0.2}Zn_{0.2}Fe_{2.6}O_4$, notwithstanding the annealing treatment at 1100 °C causes a partial sintering of the material, with consequent growth of the grains up to micrometric scale, the crystallinity and magnetic order increase lead to a strong enhancement of *Ms* value up to 106 Am^2/kg, making this sample appealing for desired application. Although this value is similar to that obtained for Mn-Zn co-doped ferrite, the different chemical composition, makes it a viable alternative for the fabrication of exchange coupled hard/soft magnetic systems. Indeed, the

realization of such system will require the annealing of the two phases at high temperature, a step where chemical reactivity may play a relevant role.

Moreover, avoiding the use of Mn ions, can further decrease the environmental impact of the final product.

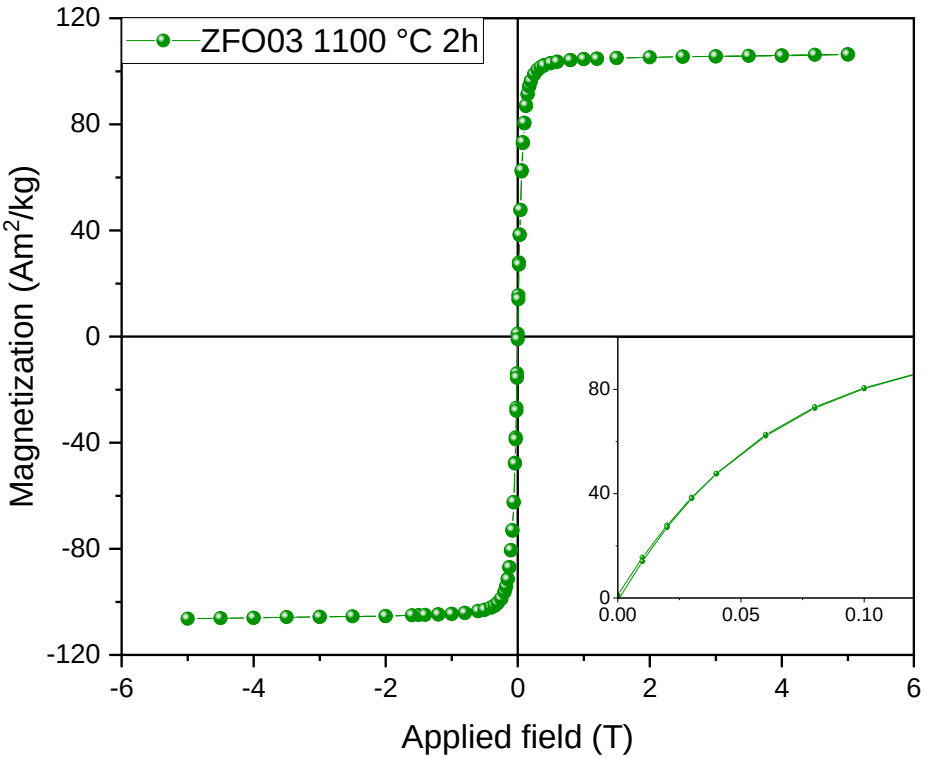

Fig. 4.22. Room temperature field dependence of the magnetization of the sample ZFO03 1100 °C 2h measured in the field range ± 5 T. In the inset, the low field region is reported.

4.3 Conclusions

$Mn_xZn_yFe_zO_4$ (x+y+z=3) NPs with different composition and similar average diameter (ca. 7-8 nm for Mn-Zn ferrites series and ca. 10 nm for Zn ferrites series) were synthesized by co-precipitation and their structural and magnetic properties were deeply characterized by TEM, XRD, ICP-AES and SQUID magnetometer. This detailed characterization allowed us to investigate the effect of the Mn and Zn substitution on the magnetic properties of the synthesized NPs and to understand whether the resulting soft magnetic materials are suitable to be employed in the realization of electronic devices for future application in the 2-5 MHz frequency range, as well as to produce exchange coupled rare-earth free permanent magnet. The obtained nanopowders at room temperature do not display magnetic irreversibility, as desired to minimize hysteresis power losses. Nevertheless, for all the synthesized samples, the M_S values, even if comparable with those reported in the literature for NPs of the same composition, were too low to use these materials for the desired applications. Thus, to improve the crystallinity of the material and to promote the migration of the ions into crystallographic sites with lower energy, so as to enhance M_S of the final product, the obtained nanopowders were exposed to high temperature thermal treatments (from 500 ° C up to 1200 ° C) in a tubular furnace under inert atmosphere (N_2 flow). The most promising samples were those with $Mn_{0.2}Zn_{0.2}Fe_{2.6}O_4$ and $Zn_{0.3}Fe_{2.7}O_4$ stoichiometries, after thermal treatment at 1100 °C for 2 hours, which show the highest saturation magnetization values (108 Am^2/kg and 106 Am^2/kg, respectively). The enhancement of M_S, ascribed to the crystallinity improvement and the increase of the magnetic order, highlights the validity of the adopted approach.

Concerning the production of inductors in the 2-5 MHz frequency range, although the $Mn_{0.2}Zn_{0.2}Fe_{2.6}O_4$ 1100 °C 2h sample shows a considerable higher M_S compared to the commercial analogue ML91S (90 Am^2/kg), its static permeability is slightly lower. However, the two values are not directly comparable since the permeability value is strongly affected by the density of material. Since the commercial powder was directly obtained by coarsely grinding a high density sintered bulk material, we should expect a much larger density than our powders, and consequently a higher permeability. In fact, as shown by the SEM analysis, $Mn_{0.2}Zn_{0.2}Fe_{2.6}O_4$ 1100 °C 2h powder consists of only partially sintered micrometric grains, and therefore it will have a higher porosity and a lower density than the commercial ML91S sintered powder. Nevertheless, the compaction and densification of our $Mn_{0.2}Zn_{0.2}Fe_{2.6}O_4$ powder, which has not been investigated in details, should lead to a significant reduction of the porosity and to a corresponding improvement of the final permeability, which possibly may exceed that of the commercial product (this latter result is expected from the higher M_S obtained).

On the other hand, the M_S value of both powders make them appealing to realize rare-earth permanent magnet through their coupling with a standard commercial product such as strontium hexaferrite.

In conclusion, despite the annealing treatment at 1100 °C caused a partial sintering of the material, with consequent growth of the grains up to micrometric scale, the enhancement of M_S and the preservation of the of the soft magnetic behaviour makes $Mn_{0.2}Zn_{0.2}Fe_{2.6}O_4$ 1100 °C 2h and $Zn_{0.3}Fe_{2.7}O_4$ 1100 °C 2h appealing for the desired applications.

Finally, the industrial scale-up of the synthetic process was carried out in collaboration with the chemical company Cabro S.p.A. in Arezzo. The large-scale synthesis was performed on a 100 liters glass reactor obtaining

ca. 0.5 kg of nanometric product with the same structural and magnetic properties as the laboratory-scale samples. However, while the industrial scale-up of the synthetic process has been successfully addressed, nowadays we are not yet able to produce large quantities of finished product. In fact, after annealing of the nanopowder at 1100 °C, in addition to the spinel structure, the presence of hematite (ca. 20 %) is observed, indicating that probably during the annealing a part of ferrite rearrange generating hematite with consequent expulsion of small amounts of amorphous MnO and/or ZnO. This result could also be due to the crystallization of small amounts of unreacted amorphous impurities (iron hydroxide or iron oxo-hydroxide) adsorbed on the surface of the nanoparticles, or to a partial oxidation of Fe^{2+} to Fe^{3+} during the long time of the industrial washing process. Precautions are thus recommended to improve and speed up the washing procedure, that is the most critical issue of the overall process. Such improvement can anyway be easily obtained in several ways. As an example, the use of larger and lower-height tanks can allow one to obtain a larger magnetic decantation surface with a low suspension thickness. This, together with the application of stronger magnets, should ensure a more effective response of the material during the separation process, speeding up the whole purification step.

References

[1] J. M. D. Coey, *Magnetism and Magnetic Materials*, Cambridge University Press **2010**.

[2] B. D. Cullity and C. D. Graham, *Introduction to Magnetic Materials*, Second Ed. Wiley-IEEE Press **2011**.

[3] M. M. Schieber, *Experimental Magnetochemistry. Nonmetallic Magnetic Materials*, vol. VIII of Selected topics in solid state physics, edited by E. P. Wohlfarth **1967**.

[4] J. Jang, H. Nah, J.-H. Lee, S. H. Moon, M. G. Kim, J. Cheon, *Angew. Chem. Int. Ed. Engl.* **2009**, 48, 1234.

[5] J. Smit, H. P. J. Wijn, N. V. Philips, *Ferrites*, Gloeilampenfabrieken **1959**.

[6] G. Petitt, D. Forester, *Phys. Rev. B* **1971**, 4, 3912.

[7] K. Raju, G. Venkataiah, D. H. Yoon, *Ceram. Int.* **2014**, 40, 9337.

[8] Y. Yafet, C. Kittel, *Phys. Rev.* **1952**, 87, 290.

[9] A. Yang, V. G. Harris, S. Calvin, X. Zuo, C. Vittoria, *IEEE Trans. Magn.* **2004**, 40, 2802.

[10] J. P. Chen, C. M. Sorensen, K. J. Klabunde, G. C. Hadjipanayis, E. Devlin, A. Kostikas, *Phys. Rev. B.* **1996**, 54, 9288.

[11] M. A. Gabal, S. S. A.-Allah, *J. Phys. Chem. Solids.* **2004**, 65, 995.

[12] E. Veena Gopalan, I. A. Al-Omari, K. A. Malini, P. A. Joy, D. Sakthi Kumar, Y. Yoshida, M. R. Anantharaman, *J. Magn. Magn. Mater.* **2009**, 321, 1092.

[13] A. Skumiel, M. Kaczmarek-Klinowska, M. Timko, M. Molcan, and M. Rajnak, *Int. J. Thermophys.* **2013**, 34, 655.

[14] H. S. C. O'Neill, A. Navrotsky, *Am. Mineral.* **1983**, 68, 181.

[15] Y. Li, Q. Li, M. Wen, Y. Zhang, Y. Zhai, Z. Xie, F. Xu, S. Wei, *J.*

Electron Spectrosc. **2007**, 160, 1.

[16] N. Modaresi, R. Afzalzadeh, B. Aslibeiki, P. Kameli, A. Ghotbi Varzaneh, I. Orue, V.A. Chernenko, *J. Magn. Magn. Mater.* **2019**, 482, 206.

[17] S. Mallesh, V. Srinivas, *J. Magn. Magn. Mater* **2019**, 475, 290.

[18] S. Singh, N. Kumar, A. Jha, M. Sahni, R. Bhargava, A. Chawla, R. Chandra, S. Kumar, S. Chaubey, *J. Supercond. Nov. Magn.* **2014**, 27, 821.

[19] K. Praveena, K. Sadhana, H. S. Virk, *Solid State Phenom.* **2015**, 232, 45.

[20] O. Gutfleisch, M. A. Willard, E. Brück, C.H. Chen, S. G. Sankar, J. P. Liu, *Adv. Mater.* **2011**, 23, 821.

[21] K. J. Strnat, *Proc. IEEE.* **1990**, 78, 923.

[22] F. Jimenez-Villacorta, L. H. Lewis, *Advanced Permanent Magnetic Materials*, in: J. M. Gonzalez Estevez, *Nanomagnetism*, One Central Press **2014**, 160–189.

[23] Critical Raw Materials, Eur. Comm., http://ec.europa.eu/growth/sectors/raw-materials/specific-interest/critical/index_en.htm, **2017**.

[24] E. F. Kneller, R. Hawig, *IEEE Trans. Magn.* **1991**, 27, 3588.

[25] E. E. Fullerton, J. S. Jiang, S. D. Bader, *J. Magn. Magn. Mater.* **1999**, 200, 392.

[26] S. Thakur, S. C. Katyal, A. Gupta, V. R. Reddy, M. Singh, *J. Appl. Phys.* **2009**, 105, 07A521.

[27] H. H. Hamdeh, J. C. Ho, S. A. Oliver, R. J. Willey, G. Oliveri, G. Busca, *J. Appl. Phys.* **1997**, 81, 1851.

Chapter 5

Conclusions and perspectives

The experimental work presented in this thesis was focused on the design of nanometric spinel ferrites for biomedical and technological applications. On one hand, the possibility of improving the magnetic properties of ferrites reducing the size of magnetic materials to the nanometric scale was explored and, on the other, the huge versatility of ferrites and the related tunability of their physical properties was exploited. In fact, the magnetic properties of ferrites can be drastically modified by simply replacing, either partially or completely, the metal ions or by modifying the inversion degree without affecting the crystal structure. To this aim, different synthetic strategies were exploited in order to investigate the effects of different divalent metal ions (cobalt, manganese, zinc) on the magnetic properties of spinel ferrite nanoparticles.

Regards biological applications, the work focused on the effect of Co-Zn co-doping, which is supposed to increase both the magnetic moment and the anisotropy of magnetite nanoparticles and, consequently, also the hyperthermic and relaxometric efficiency. To this aim, two series of $Co_xZn_yFe_{3-(x+y)}O_4$ NPs with comparable average diameter (8 nm and 9 nm) and variable amount of Zn^{2+} ions ($x=0.6$, $0 \leq y \leq 0.4$) were synthesized by thermal decomposition of metal acetylacetonates in high-boiling solvents in the presence of surfactants and deeply characterized by TEM, DLS, HRTEM, XRD, CHN, ICP-AES, XAS, XMCD, magneto-optical

spectroscopy and SQUID magnetometry to shed light on the effect of the progressive Zn^{2+} substitution on cobalt ferrite properties. Since cobalt ions have a strong impact on the magnetic properties of this material, its content was fixed to *ca*. x=0.6, corresponding to the highest value of magnetic anisotropy for non-stoichiometric cobalt ferrite, and the amount of Zn was varied up to y=0.4, for which the maximum of saturation magnetization is observed in the bulk material. This approach allowed us to better evaluate the peculiar role of Zn inclusion on the magnetic properties of the system, which is otherwise masked by any modification in the Co content. The thermal decomposition synthetic technique was chosen because, even if it does not allow to obtain large quantities of product (hundreds of mg), allows to obtain MNPs with high crystallinity and to have a good control on the composition, morphology, size and size distribution of the MNPs. Moreover, the surfactants used in the synthesis allow both to control the growth process of the MNPs as to stabilize the surface preventing MNPs agglomeration and ensuring their stability in solution. Thus, this synthetic technique allowed us to focus the study on the variation of the magnetic, hyperthermic and relaxometric properties due to the different composition neglecting the strong dependence of these properties on the volume of the nanoparticles. The analysis of the magnetic behavior of the series demonstrated that the expected increase of magnetic moment with progressive Zn substitution, due to the unbalance between T_d and O_h spin sublattices, is preserved only at low temperature. On the contrary, on increasing temperature the thermal disorder decreases the spin alignment degree, and, at room temperature the increase of M_S is retained only for very small amounts of Zn. Moreover, this effect is further counterbalanced by the strong reduction of magnetic anisotropy produced by the insertion of Zn^{2+} ions in the spinel lattice, as indeed demonstrated by magnetic,

XMCD and magneto-optical measurements. This behavior can be ascribed to the lattice expansion and local crystal distortion, as well as to the modification in cation distribution following the substitution.

These results redefine the expectations relying on Zn-substitution as an effective strategy to improve the performances of cobalt ferrite MNPs, particularly in view of their potential employment in MRI and MFH applications. To evaluate the impact of these modifications on the hyperthermic and relaxometric efficiency of the synthesized samples, calorimetric measurements of specific absorption rate (SAR) and nuclear longitudinal and transverse relaxivity (r_1, r_2) measurement were performed. If on one hand the obtained results show that increasing the Zn-content raises the capability of NPs of contrasting MR images, on the other, we found that only small amounts of zinc ($0.05 \leq y \leq 0.15$) increases the hyperthermic efficiency of cobalt ferrite NPs while the SAR decrease upon further increase of Zn-content. However, the SAR value achieved for the 8 nm sample CoZnFe05, although ca. 3 times higher than that of the sample CoFe00 (53 W/g compared to 17 W/g), is not very high if compared to the literature data reported for ferrite NPs specifically synthesized for this application. Nevertheless, a further increase of SAR of Co-Zn ferrite was easily obtained by a small increase of the mean size of the NPs. In fact, the SAR value for the 9 nm sample with the smallest amount of zinc ($y = 0.05$) reaches 103 W/g. Thus, we can conclude that this sample, with a large heat capability, is a very promising candidate for clinical application in MFH.

As future perspective, beside the inorganic magnetic core of Co-Zn doped magnetite, the attention will be focused on the realization of a suitable systems for biomedical applications through a proper functionalization of the NPs surface with specific molecules, bio-molecules or polymers, in

order to grant the biocompatibility and confer to the nanostructure specific properties (i.e. targeting, drug delivery, stealth) with the aim to realize an efficient theranostic platform.

Concerning technological applications, in view of a possible large-scale production, $Mn_xZn_yFe_zO_4$ (x+y+z=3) NPs with different composition and similar average diameter (ca. 7-8 nm for Mn-Zn ferrites series and ca. 10 nm for Zn ferrites series), were synthesized by co-precipitation starting from aqueous solution of manganese, zinc, iron (II) and iron (III) chlorides in basic aqueous solution (NaOH) at 100 °C, under inert atmosphere (N_2). This synthetic method was chosen because, even if it does not allow to obtain MNPs with high uniformity (size, shape) and crystallinity, it is simple, cheap, eco-sustainable (aqueous synthesis), allows one to obtain large quantities of materials (grams) and it is easily scalable to industrial production (up to kilograms). The synthesized samples were deeply characterized by TEM, SEM, XRD, ICP-AES and SQUID magnetometry. This detailed structural and magnetic characterization allowed us to investigate the effect of the Mn and Zn substitution on the magnetic properties of the synthesized NPs and to identify the stoichiometry and the thermal treatment conditions to maximize the M_S of the final product. Moreover, it allowed us to understand whether these soft magnetic materials are suitable to be used as low power loss powder with high M_S and magnetic permeability for improving traditional electronic devices and for future application in the higher, 2-5 MHz, frequency range, as well as to produce exchange coupled rare-earth free permanent magnet through mixing with a standard ferrite hard phase. It is important to note, that this latter objective partially matches that carried on to obtaining a low power loss Mn-Zn ferrite powder. The improvement of the magnetic properties of the material in the two applications requires, indeed, the maximization

of the magnetic permeability in one hand, and of the remanence in the other, conditions which can be both satisfied by a soft magnetic material with a high M_S value. At room temperature no magnetic irreversibility was observed for all the synthesized samples, and the M_S values, even if comparable with those reported in the literature for NPs of the same composition, were too low to directly use these materials for the desired applications. This result was ascribed to the low crystallinity and magnetic disorder typical of NPs prepared by this synthetic method, To improve the spin ordering of the material and to promote the migration of the ions into crystallographic sites with lower energy, so as to enhance M_S of the final product, the obtained nanopowders were exposed to high temperature thermal treatments (from 500 ° C up to 1200 ° C) in a tubular furnace under inert atmosphere (N_2 flow). The most promising samples were those with $Mn_{0.2}Zn_{0.2}Fe_{2.6}O_4$ and $Zn_{0.3}Fe_{2.7}O_4$ stoichiometries, after thermal treatment at 1100 °C for 2 hours, which show the highest saturation magnetization values (108 Am^2/kg and 106 Am^2/kg, respectively). The enhancement of M_S, ascribed to the crystallinity improvement and the increase of the magnetic order, highlights the validity of the adopted approach.

In view of a possible application of the material for the production of inductors operating in the 2-5 MHz frequency range, although the $Mn_{0.2}Zn_{0.2}Fe_{2.6}O_4$ 1100 °C 2h sample shows a considerable higher M_S compared to the commercial analogue ML91S (90 Am^2/kg), its static permeability was slightly lower. However, the two values are not directly comparable since the permeability value is strongly affected by the density of the material. Actually, we do expect that compaction and densification of our $Mn_{0.2}Zn_{0.2}Fe_{2.6}O_4$ powder should lead to a significant reduction of the porosity and to a corresponding improvement of the final permeability, which possibly, thanks to the higher M_S, may exceed that of the

commercial product.

On the other hand, the M_S value of both Mn-Zn and Zn ferrites make them appealing to realize rare-earth permanent magnet through their coupling with a standard commercial product such as strontium hexaferrite.

To conclude, despite the annealing treatment at 1100 °C caused a partial sintering of the material, with the consequent growth of the grains up to the micrometric scale, the enhancement of M_S and the preservation of the soft magnetic behaviour make $Mn_{0.2}Zn_{0.2}Fe_{2.6}O_4$ 1100 °C 2h and $Zn_{0.3}Fe_{2.7}O_4$ 1100 °C 2h appealing for the envisaged applications. In particular, the different chemical composition of the latter sample, makes it a viable alternative to Mn-Zn ferrite, for the fabrication of exchange coupled hard/soft magnetic systems. Indeed, the realization of such system will require the annealing of the two phases at high temperature, a step where chemical reactivity may play a relevant role. Moreover, avoiding the use of Mn ions, can further decrease the environmental impact of the final product.

Finally, the industrial scale-up of the synthetic process was carried out in collaboration with the chemical company Cabro S.p.A. in Arezzo. The large-scale synthesis was performed on a 100 liters glass reactor obtaining ca. 0.5 kg of nanometric product with the same structural and magnetic properties as the laboratory-scale samples. However, while the industrial scale-up of the synthetic process has been successfully addressed, nowadays we are not yet able to produce large quantities of finished product. In fact, after annealing of the nanopowder at 1100 °C, in addition to the spinel structure, the presence of hematite (ca. 20 %) is observed, indicating that probably during the annealing a part of ferrite rearrange generating hematite with consequent expulsion of small amounts of amorphous MnO and/or ZnO. This result could also be due to the

crystallization of small amounts of unreacted amorphous impurities (iron hydroxide or iron oxo-hydroxide) adsorbed on the surface of the nanoparticles, or to a partial oxidation of Fe^{2+} to Fe^{3+} during the long time of the industrial washing process. Precautions are thus recommended to improve and speed up the washing procedure, that is the most critical issue of the overall process. Such improvement can anyway be easily obtained in several ways. As an example, the use of larger and lower-height tanks can allow one to obtain a larger magnetic decantation surface with a low suspension thickness. This, together with the application of stronger magnets, should ensure a more effective response of the material during the separation process, speeding up the whole purification step.

Chapter 6

Experimental section

6.1 Synthesis

6.1.1 Materials

All the samples were prepared under inert atmosphere using commercially available reagents. Hexane (99%), benzyl ether (99%), oleic acid (90%), oleylamine (70%), cobalt (II) acetylacetonate ($Co(acac)_2 \cdot 2\ H_2O$, 97%), zinc (II) acetylacetonate hydrate ($Zn(acac)_2 \cdot x\ H_2O$, 98%), tetramethyl ammonium hydroxide solution (TMAOH, 25% in water), cobalt chloride hexahydrate ($CoCl_2 \cdot 6\ H_2O \geq 98\%$), zinc chloride hydrate ($ZnCl_2 \cdot x\ H_2O \geq 98\%$), iron (III) chloride hexa-hydrate ($FeCl_3 \cdot 6\ H_2O$, 98 %), iron (II) chloride tetra-hydrate ($FeCl_2 \cdot 4\ H_2O$, 98 %), manganese chloride tetra-hydrate ($MnCl_2 \cdot 4\ H_2O$, $\geq$ 99 %), sodium hydroxide (NaOH, $\geq$ 98 %) were purchased from Aldrich Chemical Co. and iron (III) acetylacetonate ($Fe(acac)_3$, 99 %) from Strem Chemicals, Inc.. Absolute ethanol (EtOH) was purchased from Fluka. All chemicals were used as received.

6.1.2 Synthesis of $Co_xZn_yFe_{3-(x+y)}O_4$ NPs by thermal decomposition

Regarding $Co_xZn_yFe_{3-(x+y)}O_4$ NPs, in the following, samples will be labeled as CoZnFeyy where yy denotes the zinc content (i.e., y = 0.13 corresponds to yy = 13). The label of the 9 nm average size NPs includes the term "_9" at the end.

8 nm $Co_xZn_yFe_{3-(x+y)}O_4$ NPs. In a typical synthesis, $Fe(acac)_3$ (0.233 g, 0.66 mmol), $Co(acac)_2 \cdot 2\ H_2O$ (0.058 g, 0.198 mmol), $ZnCl_2 \cdot x\ H_2O$ (progressive amounts from 0 to 0.119 g, 0 to 0.873 mmol, oleylamine (0.268 g, 1 mmol) and oleic acid (0.283 g, 1 mmol) were mixed and magnetically stirred in a three neck round bottom flask (100 ml) under a flow of nitrogen in benzyl ether (50 ml) for 15 min. The resulting mixture was heated to reflux (290 °C) at 9 °C/min and kept at this temperature for 15 min under a blanket of nitrogen and vigorous stirring. The black-brown mixture was cooled at room temperature by removing the heat source. Under ambient conditions, EtOH (60 ml) was added to the mixture, causing the precipitation of a black material which was magnetically separated. The obtained product was then washed several times with ethanol, dispersed in hexane, re-precipitated with ethanol, separated with a magnet, redispersed in hexane and then centrifuged (5000 rpm, 5 min). The synthesis and purification conditions for **CoFe00** was the same, but the metal/oleic acid/oleylamine ratio 1:5:5.

9 nm $Co_xZn_yFe_{3-(x+y)}O_4$ NPs. The synthesis of these samples was carried out following the same protocol (**CoZnFe11_9**) or using $CoCl_2 \cdot 6\ H_2O$ (**CoZnFe05_9**) or $Zn(acac)_2 \cdot x\ H_2O$ (**CoZnFe26_9**) as reagents.

All the products can be readily dispersed in hexane or other apolar solvents, giving stable suspensions without aggregates. as demonstrated by Dynamic light scattering (DLS) measurements. As shown in Figure 6.1, the hydrodynamic diameter was found to increase by 3 nm respect to TEM diameter.

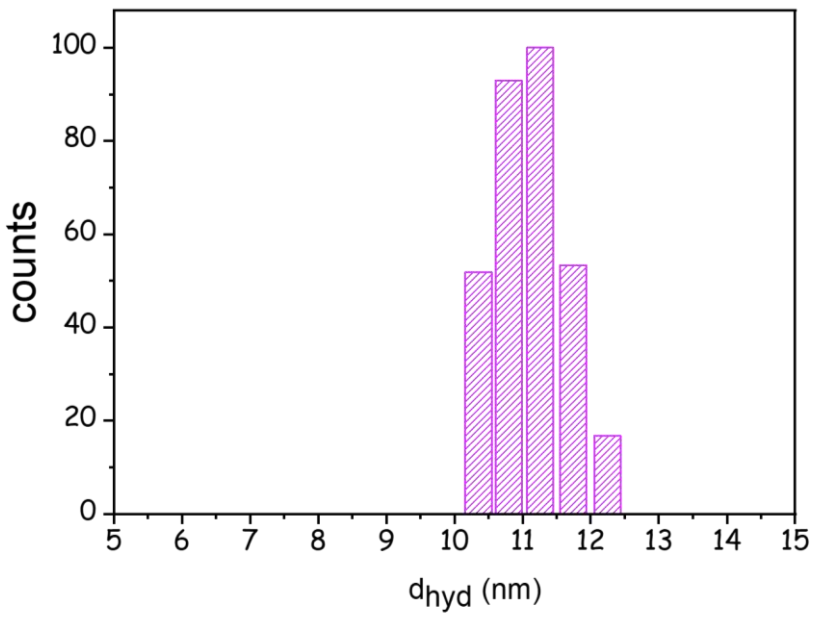

Fig. 6.1. Representative measurement of hydrodynamic size, d_{hyd}, performed by dynamic light scattering technique on sample CoFe00 in toluene**.** The average value is 11.1 nm with a standard deviation of 0.5 nm. DLS measurements were carried out with a Malvern Zetasizer ZS90, Malvern Instruments Ltd.

6.1.3 Ligand-exchange with tetrametylammonium hydroxide (TMAOH)

5 mg of the NPs were dispersed in 10 ml of a 10% wt. TMAOH aqueous solution and sonicated for 10 min. Several washings with TMAOH solution were important to ensure removal of the oleic acid, leaving the NPs with a negative surface charge enough to stabilize the dispersion. The hydrodynamic radius was estimated to increase by 3-4 nm with respect to the inorganic core. After that, the NPs were collected with a permanent magnet and re-dispersed in deionized water (5 ml, 1 mg/ml).

6.1.4 Synthesis of $Mn_xZn_yFe_zO_4$ NPs by co-precipitation

$Mn_{0.2}Zn_{0.2}Fe_{2.6}O_4$ NPs. In a typical synthesis, $FeCl_3 \cdot 6\ H_2O$ (13.5 g, 50 mmol), $FeCl_2 \cdot 4\ H_2O$ (2.99 g, 15 mmol), $MnCl_2 \cdot 4\ H_2O$ (0.99 g, 5 mmol), $ZnCl_2 \cdot x\ H_2O$ (0.68 g, 5 mmol) and N_2 purged demineralized water (50 ml) were mixed and magnetically stirred under a flow of nitrogen. The resulting mixture was added to a basic solution at 100 °C, obtained dissolving NaOH (8.6 g, 215 mmol) in N_2 purged demineralized water (500 ml) in a three neck round bottom flask (1 L), and kept at this temperature for 2 h under a blanket of nitrogen and vigorous magnetic stirring. The black-brown mixture was cooled to room temperature and the obtained product was separated with a permanent magnet, washed several times with water, two times with ethanol and finally dried under nitrogen. The synthesis and purification of the others sample was carried out by following the same protocol used for $Mn_{0.2}Zn_{0.2}Fe_{2.6}O_4$ NPs but the molar

ratio of metal transition chlorides was quantitatively adjusted according to the final desired stoichiometry.

6.1.5 Large-scale synthesis of $Mn_{0.2}Zn_{0.2}Fe_{2.6}O_4$ NPs

The large-scale synthesis of $Mn_{0.2}Zn_{0.2}Fe_{2.6}O_4$ NPs was performed using a 100 L industrial reactor at Cabro S. p. A. In a typical synthesis, $FeCl_3 \cdot 6 H_2O$ (1.35 kg, 5 mol), $FeCl_2 \cdot 4 H_2O$ (0.299 kg, 1.5 mol), $MnCl_2 \cdot 4 H_2O$ (0.99 kg, 0.5 mol), $ZnCl_2 \cdot x H_2O$ (0.68 kg, 0.5 mol) and N_2 purged demineralized water (2.5 L) were mixed and magnetically stirred under a flow of nitrogen. The resulting mixture was added to a basic solution at 100 °C, obtained dissolving NaOH (0.86 kg, 21.5 mol) in N_2 purged demineralized water (50 L) in a 100 L glass reactor, and kept at this temperature for 2 h under a blanket of nitrogen and vigorous mechanical stirring. The black-brown mixture was cooled to room temperature and the obtained product was separated, in several times, with a permanent magnet, washed several times with water, two times with acetone and finally dried under nitrogen.

6.2 Experimental techniques

6.2.1 Electron microscopy techniques

Electron microscopy techniques are one of the most useful and powerful methods to investigate the nanoscale. They operate on the same principles as the optical microscope but use electrons instead of light. Wavelength of light is the limitation for optical microscopy (resolution up to ca. 200 nm). Using electrons as probe radiation with a much lower wavelength allows a resolution a thousand times smaller than that achieved with light. The wavelength (λ) of an electron is determined by the de Broglie equation and, by using some assumptions, it is possible to express it in terms of the accelerating voltage (AV) used to form the electron beam:

$$\lambda\ (nm) = \frac{1.23}{(AV)^{1/2}} \qquad (6.1)$$

For example, an AV of 100 kV results in an electron wavelength of ca. 0.0039 nm, corresponding to a resolution of ca. 0.24 nm. This value is obtained by the Abbe's equation for a perfect optical system. In practice, aberrations and distortions due to the optical apparatus (lens, aperture etc.) determine the real resolution limit. The different types of electron microscopes (EM) can be divided into two main categories, Transmission Electron Microscopes (TEM) and Scanning Electron Microscopes (SEM), depending on the optics (Figure 6.2), signal detection and, consequently, type of information obtained. Both types of EM have an electron gun, which contains an electron source that produces a cloud of electrons, a Wehnelt cylinder to form the electron beam and an anode to accelerate the

beam. There are three main types of electron source; a tungsten filament (W), a lanthanum hexaboride (LaB_6) single crystal and a field emission filament. Tungsten is normally used in thermionic electron guns because of its high melting point and low vapor pressure, compared with other metals, and because of its low cost. The differences among the filaments are shown in Table 6.1.

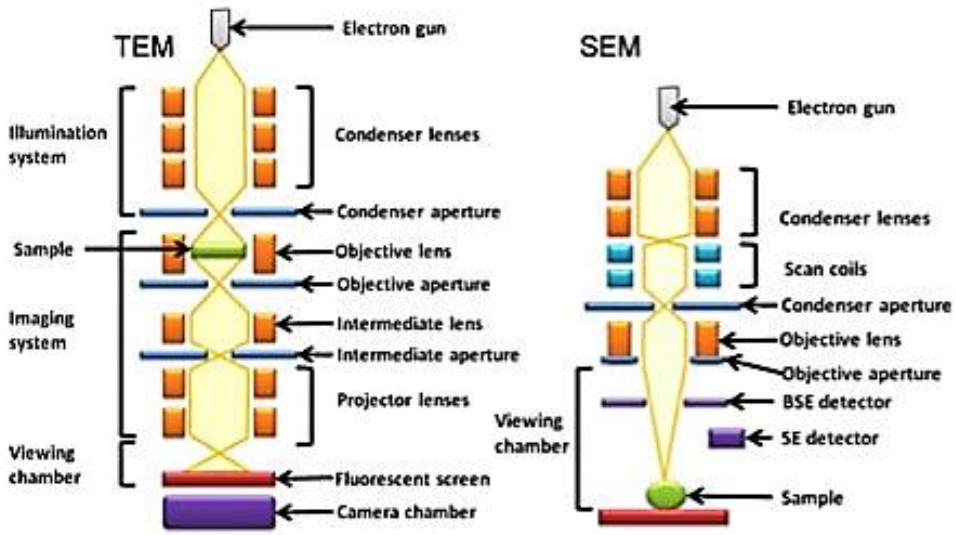

Fig. 6.2. Optics of standard TEM and SEM [1].

Both TEM and SEM use electromagnetic lenses to focus the electron beam. As a light beam is focused by using glass lenses, electrons are collimated by travelling inside a magnetic field (magnetic lenses). Apertures associated with the lenses are thin plates of molybdenum with several small holes (usually a range of 10-300 μm in diameter). Apertures are used in an EM to control the coherence of the beam, which affects the resolution and the signal contrast.

Type of source	Thermionic		Cold field emission	Schottky field emission
Material	Tungsten (W)	Lanthanum hexaboride (LaB6)	Tungsten (W)	Zirconiated tungsten (ZrO/W)
Beam diameter	1-2 µm	1-2 µm	3-5 nm	10-25 nm
Brightness (A/cm^2sr)	10^6	10^7	10^9	10^8
Energy range (eV)	2.0	1.5	0.2-0.3	0.3-1
Resolution (nm)	<3	<2	<1	<1

Tab. 6.1. Comparison of different electron guns used to produce a beam in an electron microscope. Data obtained from Hitachi (Berkshire, UK) and Carl Zeiss (Cambridge, UK). Modified from Ref. [1].

6.2.1.1 Transmission electron microscopy (TEM)

In TEM technique a beam of electrons is transmitted through an ultra-thin specimen. The image formed by the electrons transmitted through the specimen is magnified and focused onto an image recording device, such as a fluorescent screen, or a sensor coupled to a CCD camera (Figure 6.2). To obtain a clear image, the column containing the magnetic lenses and the specimen must be under high vacuum to avoid electrons deflection by collisions with air molecules. Below the electron gun there are two or more condenser lenses. These lenses demagnify the beam emitted by the gun and control its diameter as it hits the specimen. The condenser aperture, present under the condenser lenses, can be used to control the convergence angle of the beam. The condenser lenses are responsible for the amount of

illumination that reaches the sample and control the beam intensity and brightness. The objective lens focuses the electron beam onto the sample, producing a small magnification (first intermediate image). The intermediate and projector lenses magnify the beam and project it onto the CCD camera or screen to form an image. Only a few seconds are needed to obtain a micrograph (microscope image). This is a result of the projected beam intensity: transmitted electrons are detected as light areas in the micrograph, while darker areas occur where electrons do not reach the screen because they have been scattered or absorbed by the sample (bright field imaging).

In the present work, average diameter and size distribution of NPs were determined by low resolution TEM, using the CM12 PHILIPS microscope, equipped with a LaB_6 filament operating at 100 kV of Centro di Microscopie Elettroniche "Laura Bonzi" (CE.M.E.) at CNR-ICCOM, Firenze. Samples were prepared by drop drying a diluted suspension of NPs in hexane or ethanol onto 200 mesh carbon-coated copper grids. The recorded images were analyzed with the ImageJ software. The mean diameter and the size distribution of each sample were obtained by statistical analysis over 700–750 particles.

High-resolution TEM (HRTEM) images and energy dispersive X-ray spectra (EDS) were acquired by Dr. Giovanni Bertoni at I.M.E.M-C.N.R., Parco Area delle Scienze, Parma, using at a JEOL JEM-2200FS microscope equipped with a Ω filter operating at 200kV. The NPs were dispersed in hexane and then placed dropwise onto a carbon supported grid.

6.2.1.2 Scanning electron microscopy (SEM)

In SEM, electrons interact with the atoms of a sample, producing various signals that contain information about the surface topography and composition. The electron beam is generally focused into a small spot that scans across the surface of the sample (Figure 6.2). The condenser lens assembles the electrons into a thin beam while the objective lens focuses the beam onto the sample. Deflection coils cause the beam projection to move in two perpendicular directions (X, Y), producing a raster scan across the surface of the sample. The signal, amplified by different electronic amplifiers, is transmitted to a computer screen and displayed as variations in brightness. Reducing the scanned area results in an increase in magnification. A SEM image is formed by signals emitted from the sample as a result of the interaction with the electrons of the beam (Figure 6.3). Most SEM generate images by two types of electrons. Secondary electrons (SE) are low energy electrons produced by small energy transfers between beam electrons and orbiting electrons of the sample atoms. The energy transfer causes the orbiting electron to leave the atom, becoming a SE. An outer orbiting electron will then release some energy in order to jump into the gap left by the SE. The second type, backscattered electrons (BSE), are high energy electrons that have passed close to an atomic nucleus and been reflected or "back-scattered" out of the specimen. Additional information can be obtained by detecting the characteristic X-rays (energy dispersive X-ray spectroscopy) or photons (cathodoluminescence) emitted by the beam-sample interaction.

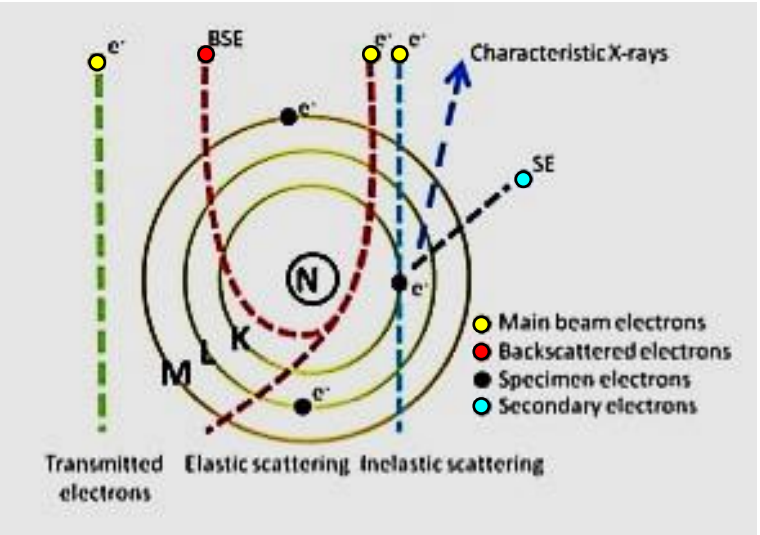

Fig. 6.3. Specimen-beam interaction at the atomic level. The main signals relevant for TEM are those of transmitted and scattered electrons, which create the contrast in the final image. For the SEM, the main signals are due to secondary and backscattered electrons. Modified from Ref. [1].

There are different types of detectors to collect these signals. Due to the different energies, only SE produced near the surface can be detected while detected BSE can originate in deep within the sample (Figure 6.4). Since heavy elements (high atomic number) backscatter electrons more strongly than light elements (low atomic number), BSE are used to evidence contrast between areas with different chemical compositions. The resolution of a SEM image depends on the spot size of the beam, as it hits the sample and, on the beam/sample interaction volume, directly related to the AV of the beam (Figure 6.4).

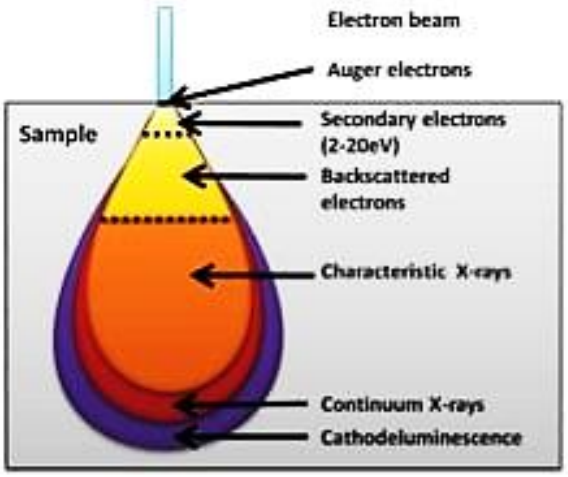

Fig. 6.4. Interaction volume of the electron beam with a sample. The diagram shows the regions from which signals with enough energy to leave the sample and be detected originated [1].

In this work, SEM images were acquired using the HITACHI S2300 Scanning Electron Microscope, equipped with PathFinder ThermoScientific software ver.1.3. at the research group laboratory of Prof. Ugo Bardi and Dr. Stefano Caporali of the Dipartimento di Chimica "Ugo Schiff" of Università degli Studi di Firenze (we are grateful to Dr. Stefano Martinuzzi for acquiring the images). Samples were prepared spreading a small amount of powder on a metal stub covered with a sticky carbon tape which increases conductivity.

6.2.2 X-Ray based techniques

X-radiation is an electromagnetic radiation in the wavelength range from 0.01 to 10 nm, (corresponding to energies in the range 0.1 - 100 keV), i.e.,

shorter than that of UV-rays and typically longer than that of gamma rays. X-rays with energies above 5–10 keV (below 0.2–0.1 nm wavelength) are called hard X-rays, while those with lower energy are called soft X-rays. Since the wavelengths of hard X-rays are comparable to the size of atoms, they can be useful for determining crystal structures by X-ray crystallography.

6.2.2.1 X-Ray powder diffraction (XRPD)

XRPD is a rapid, non-destructive analytical technique used for phase identification of a crystalline material and can provide information on lattice parameter and crystal size. For example, the analysis of the peak position and intensity in the diffracted pattern, provide precise information on the types of phases present in the samples and their relative amounts. Another important piece of information, obtained from the analysis of the peak width and shape, is the crystallite size and the microstrains. Diffraction phenomenon is described by the Bragg's law (Figure 6.5) and occurs when radiation, with a wavelength comparable to atomic spacings, is scattered in a specular way by the atoms of a crystalline system and undergoes constructive interference. If an incident X-ray beam is perfectly collimated and monochromatic (with a single wavelength, λ) and makes an incident angle θ with respect to the reticular planes of the crystal, X-rays are partially scattered by atoms when they strike the surface of a crystal. The part of the X-ray that is not scattered passes through to the next layer of atoms, where again part of the X-ray is scattered, part passes through to the next layer and so on. If X-rays diffracted by two different layers are in phase, constructive interference occurs and the diffraction pattern shows a peak, while if they are out of phase, destructive

interference occurs and no diffracted signal (no peak) is recorded. Thus, diffraction peaks only occur if the difference between the path lengths of the two X-rays is equal to an integer multiple of the wavelength:

$$n\lambda = 2d(hkl)\sin(\theta) \tag{6.2}$$

where *n*, the reflection order, is an integer number and *d(hkl)* is the inter-planar distance of one family of (hkl) crystallographic planes.

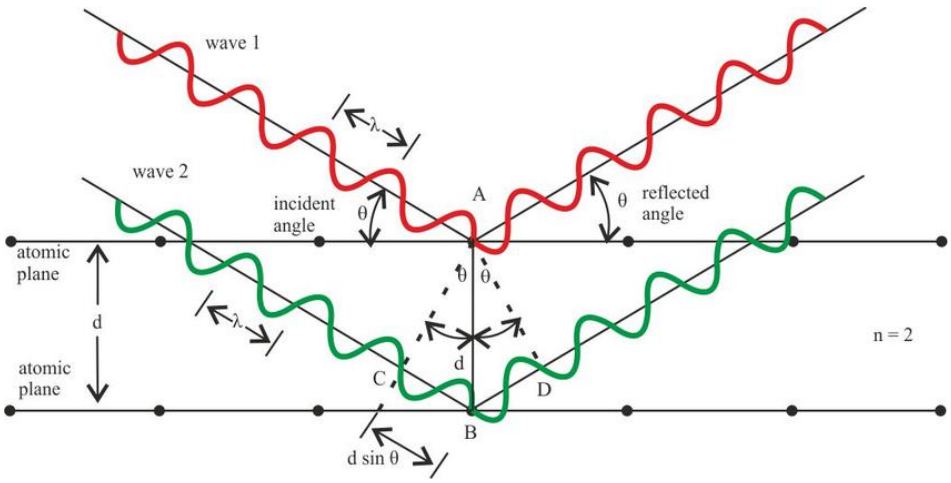

Fig. 6.5. Schematic representation of Bragg's law which can be derived from the triangle ABC [2].

A diffraction pattern is obtained by measuring the intensity of scattered X-rays as a function of scattering angle. Very strong intensities known as Bragg peaks are obtained in the diffraction pattern at the points where the scattering angles satisfy Bragg condition. Since a highly regular structure is needed for diffraction to occur, only crystalline solids will diffract; amorphous materials will not show up in a diffraction pattern.

Most materials have a characteristic diffraction patterns that can be identified by comparing the experimental and reference diffractograms available in the crystallographic databases. A diffraction pattern can also be used to determine and refine the lattice parameters of a crystal structure by using a method known as Rietveld refinement. Moreover, the crystallite size of the powder can be estimated by using the Scherrer formula.

The interplanar distance d(hkl) can be understood as a geometric function of size and shape of a unit cell for a diffracted crystallographic structure. After assigning the Miller indices (h,k,l) to all the peaks, it is also possible to calculate the lattice parameters, adding information about the phases present in the sample. In the simplest case of a cubic crystallographic structure cell of side "a", d(hkl) can be related to the cell parameter "a" [3, 4].

$$d(hkl) = \frac{a}{\sqrt[2]{h^2 + k^2 + l^2}} \tag{6.3}$$

Diffraction peaks intensity. The measured diffraction pattern includes information about peak positions and intensity. The position of diffraction peaks and the corresponding *d(hkl)* provide information about the location of lattice planes, the crystal structure and the symmetry of the contributing phase. Each peak identifies a d-spacing that represents a family of lattice planes *d(hkl)*. Moreover, each peak has a characteristic intensity which, once related to the most intense one, indicates the relative strength of the diffraction. An accurate measure of the intensity relationships in a pattern is obtained by measuring the area (without background) under the peaks. Peak intensities have been calculated theoretically for most crystal

structures, so that comparing the experimental peak intensity to the theoretical one allows determining the diffracting material phase.

Scherrer equation. Bragg's law assumes that the crystal is ideal (without structural defects) and the incident beam is perfectly monochromatic and collimated. On the contrary, these conditions are never completely fulfilled in the experiments. Moreover, the particles are usually composed by several crystallites with different orientation and with certain number of defects. The size of these crystallites and the microstrains present in them can be estimated from the diffraction pattern [3], since both effects contribute to determine the width of the diffraction peaks. The crystallite size *d* can be easily estimated from the full width at half maximum (FWHM) of each diffraction peak, as given by the Scherrer equation:

$$d = \frac{K_\alpha \lambda}{(FWHM)_i cos\theta_i} \tag{6.4}$$

where K_α is a constant dependent on the crystallite shape and λ is the incident wavelength [3].

Rietveld refinement. The Rietveld method is used to fit the experimental diffraction patterns by considering the instrumental contribution, assuming a certain crystal structure and adjusting different structural parameters, such as atomic displacements, anisotropy and microstrain. The chosen parameters are adjusted in an iterative process until convergence is reached between the values of the experimental intensities and the theoretical model. Different programs which use Rietveld method, such as Topas, are available.

In the present work, the X-ray diffractograms were obtained on loosely packed powdered samples using the Bruker Advantage D8 diffractometer, equipped with CuKα radiation and operating in θ–θ Bragg Brentano geometry at 40 kV and 40 mA, of Centro di Cristallografia Strutturale (CRIST) of the Dipartimento di Chimica "Ugo Schiff" of Università degli Studi di Firenze. The measurements were carried out in the 25-70 º 2θ range with a step size of 0.03 º and collection time of 1 s. Rietveld refinement, lattice parameters and mean crystallite diameters were evaluated by TOPAS software (Bruker) using the method of fundamental parameter approach based on the Scherrer equation. We are grateful to Samuele Ciattini, Francesca Loglio and Laura Chelazzi for helping us with XRD measurements.

6.2.3 Magnetometric techniques

The principle aim of magnetometry is to measure the magnetic response of a material when it is inserted in an external magnetic field. This can be achieved in many different ways, using various magnetic phenomena. Magnetometers can operate in AC or DC mode, depending on whether the magnetic field of the instrument is oscillating (AC) or static one (DC). The magnetic measurements reported in this thesis were made by a Superconducting Quantum Interference Device (SQUID) magnetometer. This instrumentation is based on the Faraday law: when a coil is concatenated to a time-varying magnetic field flow, a current proportional to the flow variation is generated in it. In order to perform measurement, a sample is moved in a homogeneous magnetic field produced by a superconductive coil. This movement induces a flux variation in time, proportional to the magnetic moment of the sample, which can be

measured by the current induced in the detection coil. Typically, the SQUID and the magnet need to be dipped in a liquid He cryostat, that also allows the control of temperature of the sample. A vacuum gap (10^{-6} bar) around the measuring chamber produces a thermal isolation from the surroundings. In some instrumentation, in order to reduce the He^4 waste, another gap filled with liquid nitrogen can be present. The measuring chamber and the He bath are in communication by a thin capillary and the incoming flux is regulated by an external pump. This device, coupled with a heater located near the sample, controls the temperature during the measurement. Thanks to a pumping system on the sample chamber it is possible to reach temperature lower than the boiling point of He^4 (4.2 K), ranging from 1.8 K to 350K. The He bath has the function to keep the magnet, the measuring device coupled to SQUID and the SQUID itself in the superconductive regime. The SQUID is a measuring device composed of a superconductive coil at low temperature with a Josephson junction. The Josephson junction consists in an extremely narrow insulating layer (normally an oxide) between two superconductors elements. The current can flow through the insulating layer thanks to the tunneling effect, oscillating between a maximum and a minimum for each flux quantum induced by the sample magnetic moment moving in the detection coils, The sensitivity of a SQUID is 10^{-14} Wb for magnetic flux, corresponding to magnetizations of 10^{-7}-10^{-9} emu. Due to the high sensitivity of SQUID, the whole measuring apparatus must be shielded from external spurious magnetic fields with a layer of NbTi and the sample cannot be moved directly inside the SQUID. In practice, the magnetic moment detection requires a more complex device, as shown in Figure 6.6. The measurement consists in moving the sample through pick-up coils, coupled with other ones, called input coils, which inductively transmit the magnetic flux

variation to the SQUID. The SQUID converts these variations in an electric signal and send it to the acquiring system on PC through another series of coils, called output coils. The pick-up coils form a gradiometer, a system able to measure only the gradient of magnetic field. A first-order gradiometer is composed by two superconductive coils with the same number of turns but wrapped in opposed directions. In this way, every contribution to the flux which does not depend on the sample movement is removed. A more sensitive device, called second-order gradiometer (Figure 6.7) can be realized by using three coils, the central one with a double number of turns wrapped in the opposite direction with respect to the two external ones. In both cases, the magnetic moment results from the amplitude of the signal registered while moving the sample.

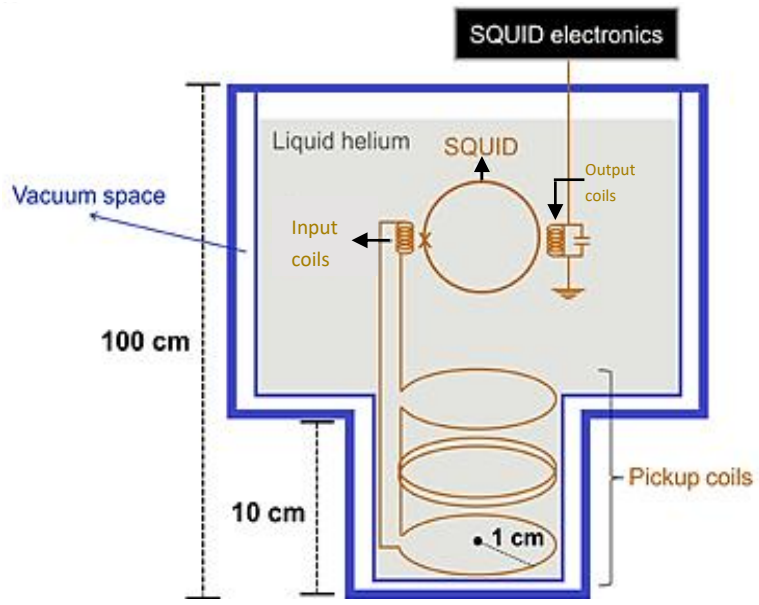

Fig. 6.6. Schematic representation of the coils system. Modified from Ref. [5].

The temperature is monitored by two GaAs diode thermometers, connected to a Lakeshore 340 controller. The first one is placed close to the sample, near the gradiometer, while the second one is used for software automatic control of temperature and it is placed near the heater, which produced the desired temperature settings. The sensitivity of those thermometers allows one to appreciate temperature variations up to 0.001K.

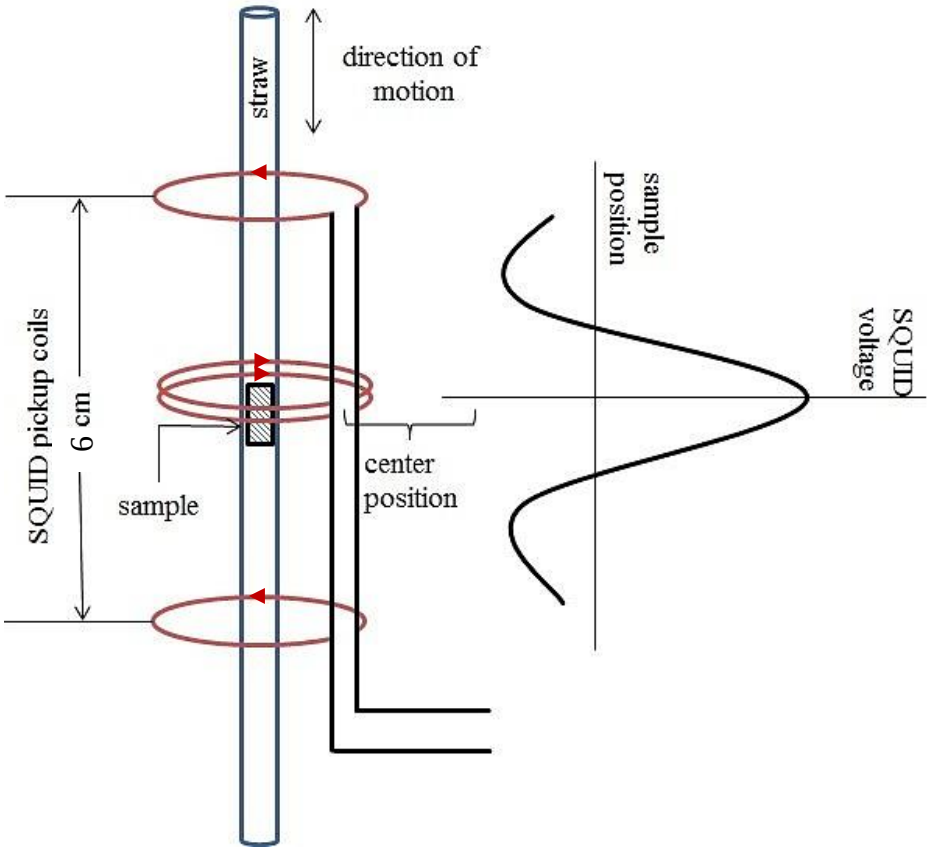

Fig. 6.7. Pick up coils in a second order gradiometer. Modified from Ref. [6].

As final result, a magnetometer in DC mode is able to measure the magnetic moment (or magnetization, when referred to the sample mass) of the sample, as a function of:

- the temperature, M(T).
- the applied field, M(H).

In this work, M(T) measurements were performed using the procedure as follows:

1. Zero-field cooling (ZFC), where the samples are cooled without any field applied at low temperature (10K) and once the desired T is reached, a small magnetic field (50 Oe) is applied. Then, the temperature is increased up to 350K and the magnetization measured.
2. Field cooling (FC), where the sample is cooled in the presence of a small external magnetic field (50 Oe) and the magnetization is measured during stepwise warming in the same applied field.

Usually, both measurements are plotted together as a function of temperature. From these curves, information about magnetic transition temperatures such as Curie, Neel or Blocking temperatures (T_C, T_N, T_B, respectively) can be obtained.

M(H) measurements were performed cooling the samples to the desirable temperature in a FC (with high magnetic field applied, typically, 50 kOe) or ZFC procedure. Then, the sample is magnetically saturated with a positive high field (+ 50 kOe). Then, the magnetization is measured while decreasing the field until the opposite, negative, saturation (- 50 kOe) is reached. Finally, the magnetization is measured increasing field back to positive saturation. The shape and size of the hysteresis loop allows to determine magnetic properties of the samples such as coercive field *(Hc)*, remnant magnetization (M_R) and saturation magnetization *(M_S)*.

Magnetic measurements were performed using two SQUID magnetometers (Quantum Design MPMS and Cryogenic Ltd. S600) operating in the 1.8 - 350 K temperature range with applied field up to 5 T (Quantum Design) and 6.5 T (Cryogenic) of Laboratory of Molecular Magnetism (LAMM) of the Dipartimento di Chimica "Ugo Schiff" of Università degli Studi di Firenze. Powder samples were hosted in a teflon tape and then pressed in a pellet to prevent preferential orientation of the nano-crystallites under the magnetic field. The obtained values of magnetization were normalized by the weight of ferrite present in the sample and expressed in Am^2/kg of ferrite. ZFC/FC curves were obtained by measuring the temperature dependence of the magnetization applying a probe magnetic field (5 mT) after cooling the sample in the absence (ZFC) or in the presence (FC) of the field.

6.2.4 Magnetic heating equipment

The capability of magnetic NPs to release heat if exposed to an alternating magnetic field is generally quantified in terms of Specific Absorption Rate (SAR) o Specific Loss Power (SLP), defined as the heating power of a magnetic material per mass unit. A model for precisely evaluate the SAR from the characteristic parameters of NPs (i.e. mean diameter, size distribution, shape, chemical composition) and instrumental ones (frequency and amplitude of the alternate magnetic field), is still lacking. For this reason, the experimental measurement of SAR must be done by a calorimetric procedure, which provides direct information on the heating power of a NPs-based system. However, this kind of measurement would require a much more accurate experimental set up than those generally employed. Most of experiments are carried with power supplies working

from 50 kHz to 1 MHz and with magnetic field amplitude of few tenth of kA/m. The measuring apparatus are non-adiabatic: samples are placed in an induction coil, cooled with water or air. Up to now, there is only one adiabatic instrumentation in the world, developed at the University of Zaragoza (Spain) [7]. In this setup, the heat exchange between the sample and the external environment is strongly minimized: all the heat produced gives rise to an increase of sample temperature, allowing the very accurate measurements of SAR from a direct measurement of temperature. The great variability of protocols used from one laboratory to other leads to a lack of homogeneity of results, with consequent difficulties in the direct comparison between SAR values reported in the literature. Another difficulty for the data comparison is the large range of fields and frequencies used, often settled over the physiological limit. In fact, alternating magnetic field, of appropriate intensity and frequency (ν of 50-500 kHz, H_0 up to 15 kAm^{-1}; maintaining the $H_0\nu$ product below the tolerance threshold of 5 x 10^9 $Am^{-1}s^{-1}$ to avoid deleterious physiological responses such as skeletal muscles stimulation, cardiac stimulation and arrhythmias) should be used for the calorimetric measurements.

Here, calorimetric measurements of SAR were performed using a 6 kW power supply by Fives Celes realized in our research laboratories (Figure 6.8). The experimental setup is based on a commercial instrument composed of different elements:

- A power supply of 6 kW working in the frequency range of 50 – 400 kHz;
- An induction coil connected to the power supply and cooled with water. Depending on the frequency needed, two different coils, made by 2 and 6 windings, and nine capacitors can be assembled;
- A water-cooling system;

- An optical fiber thermometer connected to a digital temperature recorder (Fotemp).
- An ethylene glycol based thermostated glass dewar, to thermally isolate the sample from the surroundings.

Depending on the frequency chosen, this setup can work from 4.86 ± 0.05 to 19.1 ± 0.5 kA/m, by simply changing the amount of power applied through the power supply. All the parts that need to be placed in the center of the coil during measurements must be totally metal free, in order to avoid heating and even fusion of the metal parts by eddy currents generated by the ac magnetic field. For the temperature measurement, the optical fiber is dipped in the sample by a hole in the screw cap of the plastic sample holder, which is hosted in a polystyrene support.

Fig. 6.8. Picture of the magnetic heating equipment.

Measurements were carried out by applying for 300 s an alternating magnetic field of 12 kA/m amplitude and 183 kHz frequency on a suspension in toluene (1.6 - 1.9 % w/w) in the presence of 7.5 mM of oleic acid and 7.5 mM of oleylamine. The temperature of the sample was recorded using an optical fiber temperature probe (Optocon-Fotemp). Samples were surrounded by polystyrene and hosted in an ethylene glycol based thermostated glass dewar, in order to thermally isolate the sample from the surroundings. SAR values were evaluated using the equation:

$$SAR = \frac{\sum_i m_i c_{pi}}{m_{Me}} \frac{\Delta T}{\Delta t} \qquad (6.5)$$

where ΔT is the temperature increase in the interval of time Δt, m_{Me} is the total mass of metal, m_i is the mass of the *i*-species and C_{pi} its specific heat. The sum is extended to all the *i* species involved in the heat exchange. Since the measurements are carried in non-adiabatic conditions, $\Delta T/\Delta t$ values were extrapolated for t→ 0 by considering the initial slope of the temperature kinetic curves.

6.2.5 ICP-AES

ICP-AES measurements were performed in triplicate using the Varian 720-ES at the research group of Prof. R. Udisti of the Dipartimento di Chimica "Ugo Schiff" of Università degli Studi di Firenze. For the analysis, about 1 mg of sample was digested by concentrated aqua regia (HCl suprapure and HNO_3 sub-boiled in 3:1 ratio) in the presence of H_2O_2, diluted with ultrapure water (≥18 MΩ/cm) and then analyzed using Ge as

internal standard. The wavelengths used for Co, Fe, Zn and Ge were 238.204, 238.892, 206.200 and 209.426 nm, respectively.

6.2.6 CHN

CHN measurements were performed on a few mg of sample using the CHN-S Flash E1112 Thermofinnigan Elemental Analyzer of the Dipartimento di Chimica "Ugo Schiff" of Università degli Studi di Firenze.

6.2.7 MCD

Magnetic circular dichroism (MCD) spectroscopic data were acquired in the UV-Vis-NIR range (1.25 eV to 4.25 eV) with a home-built setup originally developed by Dr. Lucia Cavigli and Dr. Lapo Bogani and upgraded by Dr. Giulio Campo [8]. Experiments reported in this works were performed by Dr. Giulio Campo, Dr. Valentina Bonanni and Prof. Francesco Pineider. The magnetic field is applied parallel to the propagation direction of light with an electromagnet generating a static field of 1.3 T. The polarization of light is dynamically switched between left and right helicities at 50 kHz with a photoelastic modulator. The differential absorption signal (ΔA) between the two opposite polarizations is retrieved via phase sensitive detection with a lock-in amplifier referenced at the polarization modulation frequency. A complete MCD spectrum is taken as the difference between the spectra acquired with the magnetic field applied parallel and antiparallel to the propagation direction of light. This procedure leaves out all non-magnetic contributions to the

dichroic signal. Samples for MCD measurements were prepared by mixing 100 µl of each nanocrystal toluene suspension with 100 µl of a polystyrene solution (10 mg/ml) in toluene and casting 50 µl of the mixture on a glass slide and allowing the solvent to evaporate.

6.2.8 XAS and XMCD

XAS and XMCD measurements were performed on dried NPs of CoFe00, CoZnFe05 and CoZnFe27, spread onto carbon tape at the circular polarization beamline of the Elettra synchrotron (Trieste, Italy). Both XAS and XMCD spectra were recorded at the Fe and Co $L_{2,3}$ edges using total electron yield (TEY) mode at 10 K in a magnetic field of 3.5 T. The XMCD signal was normalized by the area of the XAS spectrum after correcting for the background. The orbital, μ_{orb}, and spin, μ_s, components of the mean magnetic moments for Fe and Co were determined using the sum-rule analysis [9]. The calculations have been carried out neglecting the magnetic dipole operator [10] and setting the total number of holes per formula unit to 3 for Co^{2+} ions and 13.7 for the Fe valence band [11, 12].

6.2.9 ^{1}H-NMR measurements

^{1}H-NMR measurements were performed at the laboratory of Prof. A. Lascialfari at the Dipartimento di Fisica of the Università degli Studi di Milano. Water suspensions for relaxometric measurements at 300 K were obtained by transferring NPs from organic to aqueous solution by ligand-exchange with TMAOH. Longitudinal nuclear relaxation times, T_1, were measured in the range 10 kHz – 60 MHz for the ^{1}H Larmor frequency,

corresponding to an applied magnetic field from 2.3 x 10-4 T to 1.4 T. To cover such a range of experimental measurements, two instruments were used: a Stelar SMARtracer, working with the fast field cycling technology and pre-polarized saturation recovery sequence, for the low field range, i.e., 10 kHz – 10 MHz, and a Stelar Spinmaster with an electromagnet for the range 10 MHz – 60 MHz. A standard saturation recovery sequence was used in the latter case. The transverse nuclear relaxation times, T_2, were also measured for each sample at the frequency $\nu = 60$ MHz with a Carr-Purcell-Meiboom-Gill sequence.

References

[1] https://bitesizebio.com/29197/introduction-electron-microscopy-biologists/.

[2] https://www.researchgate.net/figure/Schematic-stretching-of-Braggs-law-which-can-be-derived-from-the-triangle-ABC_fig6_302838100.

[3] B. D. Cullity, S. Stock, *Elements of X-ray diffraction*, Pearson Education **2001**.

[4] G. Will, *Powder diffraction: the Rietveld method and the two-stage method to determine and refine crystal structures from powder diffraction data*, Springer **2006**.

[5] https://www.researchgate.net/figure/Drawings-of-basic-designs-of-A-a-toroidal-pickup-coil-built-for-collecting-MMG-signals_fig1_280841932.

[6] https://www.researchgate.net/figure/The-configuration-of-SQUID-magnetometer-in-a-MPMS-setup_fig18_325711575.

[7] E. Natividad, M. Castro, A. Mediano, *Appl. Phys. Lett.* **2008**, 92, 093116.

[8] L. Cavigli, C. de Julian Fernandez, D. Gatteschi, M. Gurioli, C. Sangregorio, G. Mattei, P. Mazzoldi, L. Bogani *J. Magn. Magn. Mater.* **2007**, 316, 798.

[9] P. Carra, B. T. Thole, M. Altarelli, X. Wang, *Phys. Rev. Lett.* **1993**, 70, 694.

[10] J. A. Moyer, C. A. F. Vaz, D. A. Arena, D. Kumah, E. Negusse, V. E. Henrich, *Phys. Rev. B* **2011**, 84, 054447.

[11] D. J. Huang, C. F. Chang, H.-T. Jeng, G. Y. Guo, H.-J. Lin, W. B. Wu, H. C. Ku, A. Fujimori, Y. Takahashi, C. T. Chen, *Phys. Rev. Lett.* **2004**, 93, 077204.

[12] E. J. Goering, M. Lafkioti, S. Gold, G. Schuetz, *J. Magn. Magn. Mater.* **2007**, 310, 249.

Appendix

M. Bersweiler, P. Bender, L. G. Vivas, M. Albino, M. Petrecca, S. Mühlbauer, S. Erokhin, D. Berkov, C. Sangregorio, A. Michels,
"*Size-dependent spatial magnetization profile of Manganese-Zinc ferrite nanoparticles"*
Phys. Rev. B. **2019**, 100, 144434.

M. Petrecca, M. Albino, I. G. Tredici, U. Anselmi-Tamburini, M. Passaponti, A. Caneschi, C. Sangregorio.
"High density nanostructured soft ferrites prepared by High Pressure Field Assisted Sintering Technique"
J. Nanosci. Nanotechnol. **2019**, 19, 4974-4979.

P. Arosio, M. Albino, F. Orsini, P. Ferruti, A. Manfredi, L. Cabrera, A. Caneschi, P. Marzola, S. Tambalo, E. Nicolato, C. Sangregorio, A. Lascialfari, E. Ranucci.
"Multifunctional nanovectors based on polyamidoamine polymers for theranostic application"
J. Nanosci. Nanotechnol. **2019**, 19, 5020-5026.

F. Varsano, M. Bellusci, A. La Barbera, M. Petrecca, M. Albino, C. Sangregorio.
"Dry reforming of methane powered by magnetic induction"
Int. J. Hydrogen Energy **2019**, 44, 21037-21044.

M. Albino, E. Fantechi, C. Innocenti, A. López-Ortega, V. Bonanni, G. Campo, F. Pineider, M. Gurioli, P. Arosio, T. Orlando, G. Bertoni, C. de Julián Fernández, A. Lascialfari, C. Sangregorio.
"The role of Zn^{2+} substitution on the magnetic, hyperthermic and relaxometric properties of cobalt ferrite nanoparticles"
J. Phys. Chem. C **2019**,123, 6148-6157.

N. Z. Knezevic, C. Mauriello Jimenez, M. Albino, A. Vukadinovic, A. Mrakovic, E. Illes, D. Janackovic, J.-O. Durand, C. Sangregorio, D. Peddis.
"Synthesis and Characterization of Core-Shell Magnetic Mesoporous Silica and Organosilica Nanostructures"
MRS Advances **2017**, 2, 1037-1045.